

TREATMENT TIME REDUCTION THROUGH PARAMETER
OPTIMIZATION IN MAGNETIC RESONANCE GUIDED
HIGH INTENSITY FOCUSED ULTRASOUND
TREATMENTS

by

Joshua Coon

A dissertation submitted to the faculty of
The University of Utah
in partial fulfillment of the requirements for the degree of

Doctor of Philosophy

in

Physics

Department of Physics and Astronomy

The University of Utah

December 2012

Copyright © Joshua Coon 2012

All Rights Reserved

The University of Utah Graduate School

STATEMENT OF DISSERTATION APPROVAL

The dissertation of Joshua Coon

has been approved by the following supervisory committee members:

<u>Orest Symko</u>	, Chair	<u>06/19/2012</u> Date Approved
--------------------	---------	------------------------------------

<u>Robert Roemer</u>	, Member	<u>06/14/2012</u> Date Approved
----------------------	----------	------------------------------------

<u>Dennis Parker</u>	, Member	<u>06/18/2012</u> Date Approved
----------------------	----------	------------------------------------

<u>Jordan Gerton</u>	, Member	<u>06/19/2012</u> Date Approved
----------------------	----------	------------------------------------

<u>Stephan LeBohec</u>	, Member	<u>06/19/2012</u> Date Approved
------------------------	----------	------------------------------------

and by David Kieda, Chair of
the Department of Physics and Astronomy

and by Charles A. Wight, Dean of The Graduate School.

ABSTRACT

Magnetic Resonance guided High Intensity Focused Ultrasound (MRgHIFU) treatments are a promising modality for cancer treatments in which a focused beam of ultrasound energy is used to kill tumor tissue. However, obstacles still exist to its widespread clinical implementation, including long treatment times. This research demonstrates reductions in treatment times through intelligent selection of the user-controllable parameters, including: the focal zone treatment path, focal zone size, focal zone spacing, and whether to treat one or several focal zone locations at any given time. Several treatments using various combinations of these parameters were simulated using a finite difference method to solve the Pennes bio-heat transfer equation for an ultrasonically heated tissue region with a wide range of acoustic, thermal, geometric, and tumor properties. The total treatment time was iteratively optimized using either a heuristic method or routines included in the Matlab software package, with constraints imposed for patient safety and treatment efficacy.

The results demonstrate that large reductions in treatment time are possible through the intelligent selection of user-controllable treatment parameters. For the treatment path, treatment times are reduced by as much as an order of magnitude if the focal zones are arranged into stacks along the axial direction and a middle-front-back ordering is followed. For situations where normal tissue heating constraints are less stringent, these focal zones should have high levels of adjacency to further decrease

treatment times; however, adjacency should be reduced in some cases where normal tissue constraints are more stringent. Also, the use of smaller, more concentrated focal zones produces shorter treatment times than larger, more diluted focal zones, a result verified in an agar phantom model. Further, focal zones should be packed using only a small amount of overlap in the axial direction and with a small gap in the transverse direction. These studies suggest that all treatment time reductions occur due to selection of parameters that advantageously use mechanisms of decreasing the focal zone size to concentrate the power density, increasing thermal superposition in the tumor, decreasing thermal superposition in the normal tissue, and advantageously using nonlinear rates of thermal dose deposition with increasing temperature.

TABLE OF CONTENTS

ABSTRACT.....	iii
LIST OF TABLES.....	vii
ACKNOWLEDGEMENTS.....	viii
Chapters	
1. INTRODUCTION.....	1
Background Theory.....	2
Ultrasound Physics.....	2
Heating Due to Ultrasound Absorption.....	4
Modeling Heat Diffusion and Loss in Biological Tissue.....	5
Modeling Heat Damage in Biological Tissue.....	6
Optimizing Treatment Times	7
Outline of Dissertation	10
References	10
2. HIFU TREATMENT TIME REDUCTION IN SUPERFICIAL TUMORS THROUGH FOCAL ZONE PATH SELECTION.....	12
Abstract.....	13
Introduction.....	13
Methods.....	14
Results	19
Discussion.....	24
Conclusion.....	27
Acknowledgement.....	27
References.....	27
Appendix.....	28
3. HIFU TREATMENT TIME REDUCTION THROUGH HEATING APPROACH OPTIMIZATION.....	30
Abstract.....	31
Introduction	31
Methods	33
Results	38

Discussion.....	44
Conclusion.....	49
Acknowledgement.....	49
References.....	50
4. PHANTOM AND SIMULATION TEMPERATURE MATCHING THROUGH LEAST SQUARES FIT OF DOSE LINES	53
References.....	64
5. CONCLUSION.....	65
Future Work	66
Appendices	
A. GUIDE TO SIMULATION COMPUTER CODE.....	69
B. SIMULATION COMPUTER CODE.....	80

LIST OF TABLES

2.1.	Thermal and acoustic properties used in all simulations	16
2.2	Simulation configurations	17
2.3	Scanning patterns studied	18
3.1	Tissue and acoustic properties held constant in all simulations except for the changing absorptivity study	37
4.1	Summary of parameters used in the phantom treatments	55
A.1	Summary of purpose, input variables, and output variables for Matlab scripts and functions used for treatment simulations	71

ACKNOWLEDGEMENTS

I would first like to gratefully acknowledge the constant support of my mentor, Robert Roemer, with whom I credit more than any person except myself with the completion of my doctorate degree. Through countless hours of meetings, he patiently helped me to refine and expand my research, my scientific writing abilities, and my understanding of science. Over the years of working with him, I have developed a large and growing amount of respect for Bob, both on a personal and professional level. I hope to emulate in my own academic career many of the aspects of his career, including his many contributions to science and his indefatigable work ethic.

I would also like to thank Dennis Parker for initially hiring me into the group, helping me to understand the physics and basic science behind HIFU, and providing sound observations about my research that helped make the research better. I also want to thank Douglas Christensen for his help in understanding the science behind ultrasound and for his input on my research. I thoroughly enjoyed Doug's ultrasound class, and I would highly recommend it to other students.

I would also like to thank the other members of the HIFU group: Allison Payne, Nick Todd, Urvi Vyas, Yi Wang, Josh De Beaver, Mohamadou Diakite, Christopher Reed, Emily Minalga, Scott Almquist, Henrik Odéen, Robb Merrill, Nelly A. Volland, Tyler and Rock Hadley. Without your contributions, this work would have not been possible.

I would also like to express my deep appreciation to my family for all their love and support throughout the years of graduate school. I especially want to thank my father, John D. Coon, my late mother Maridee Coon , and my siblings John, Sandra, Andrea, and Michelle.

Finally, I would like to express my appreciation to several longtime friends: Ryan Gorely, Ethan Doetsch, Jeff Keyes (and his family), and Peter Carli.

This work was partially supported by grants from NIH (R01-CA134599), Siemens Medical Solutions, the Focused Ultrasound Foundation, a University of Utah Synergy Grant, the Ben B. and Iris M. Margolis Foundation, and theUCAIR facilities. A generous allocation of extensive computer time from the Center for High Performance Computing at the University of Utah is gratefully acknowledged.

CHAPTER 1

INTRODUCTION

High Intensity Focused Ultrasound (HIFU) is a promising new cancer therapy (1-8) that uses ultrasound energy to kill tumor tissue. In this treatment modality, a beam of ultrasound generated by a transducer is focused to a sharp focus (up to the diffraction limit imposed by the wavelength of the ultrasound beam) – either through the use of a phased array transducer, a lens, a geometrically curved transducer face, or any combination of the three methods – and is coupled to a patient's body through an efficient transmitting medium such as water. Similar to sunlight focused with a magnifying glass, a portion of the energy at the concentrated focus is converted to heat, which causes tissue death at the site of the focus through thermal damage.

Despite the potential of this treatment modality to present an effective, relatively noninvasive method of treating cancer, challenges still exist to its widespread clinical implementation. Foremost among these are long treatment times, with treatments of several hours common (3, 9, 10). Recent research (11, 12) has shown that these times can be reduced through intelligent selection of user controllable parameters, found through treatment simulation and optimization. Below is a concise summary of the physical and mathematical theory behind this research.

Background Theory

For HIFU treatments involving therapies that cause tumor cell death due to heat damage, there are three main components of each treatment to consider in treatment simulation routines. These components are: the deposition of heat in the body due to the ultrasound, the time evolution of the deposited energy (in the form of heat) in the body (including the resulting temperature distribution inside the body due to conduction and perfusion effects), and tissue damage caused by high temperatures. An explanation of these three components and a derivation of relevant equations is included below.

Ultrasound Physics

Ultrasound is broadly classified as a group of sound waves with frequencies above the 20 kHz limit detectible by human hearing (13). The medical uses of ultrasound imaging are well established, with ultrasound fetal imaging, ultrasound imaging of blood flow through Doppler effects, and B-mode imaging of biological tissues being just a few of the more well-known examples among the many possible.

Ultrasound waves propagate via the periodic compression and rarefaction of a medium. As with all waves, ultrasound waves have two primary components: a longitudinal (or compressional) wave that travels in the direction of the displacement of molecules in the medium and a transverse (or shear) component that travels perpendicular to the direction of molecular displacement. In biological tissues, the transverse component of the ultrasound tends to attenuate rapidly in all substances except for bone

(2), so in this treatment, we will consider only the longitudinal components of the wave equation.

With only the longitudinal components of the wave equation considered, the classical wave equation reduces to the one-dimensional wave equation:

$$\frac{\partial^2 p}{\partial z^2} - p_o K \frac{\partial^2 p}{\partial t^2} = 0 \quad (1.1)$$

where p_o is the average density of the material, K is the compressibility of the material, p is the excess pressure above static pressure, z is the direction of wave propagation, and t is time. This equation holds in the “linear” domain where the amplitudes of the pressure variations are assumed to be sufficiently small to only cause small disturbances in the medium. If the amplitude of the pressure wave is too large, this assumption of small disturbances breaks down and a more advanced treatment is needed.

There are several possible solutions to equation (1.1). Though a complete treatment of these solutions is beyond the scope of this text, a few simple solutions suffice to demonstrate the physics behind this equation. In general, any function satisfying the form $p = p_{\pm} f(kx \pm \omega t)$ will satisfy the equation above, where $k = \frac{2\pi}{\lambda}$ is the wave number (and λ is the wavelength), $\omega = 2\pi f$ is the angular frequency, and p_{\pm} is the amplitude coefficient. A specific example of a solution is the equation:

$$p = p_{\pm} \cos(kx - \omega t) \quad (1.2)$$

This equation can be understood when considered as a plane compressional wave traveling in the +Z direction. Other possible solutions include a Dirac Delta pulse at time $t = 0$ or a superposition of sine and cosine waves. The phase velocity (the rate at which the phase of the wave propagates through space) of the wave above is given by the equation $c = \frac{\omega}{k}$. Substitution of (1.2) into (1.1) additionally gives a relation specific to the propagation of plane compressional acoustic waves: $k^2 = p_o K \omega^2$ which can be combined with the definition of phase velocity to form the equation $= \frac{1}{\sqrt{p_o K}}$.

Heating Due to Ultrasound Absorption

When ultrasound energy is produced by a transducer and propagated through biological tissue, that energy is dissipated in a number of different ways. The first way is simply through the geometrical spreading of the wave due to diffraction as it propagates. Focusing reduces the effects of dispersion due to diffraction in the beam near field.

The second way in which ultrasound energy can be dissipated is through attenuation (absorption and scattering) in the medium. Under the model of a decreasing ultrasound beam due to an exponential absorption envelope, the equation for the heating due to an ultrasound plane wave is (2):

$$Q = 2 \alpha I ; I = I_o e^{-2\alpha x} \quad (1.3)$$

where Q is the heat deposited in the tissue from the ultrasound [W/m^3], I_o is the initial ultrasound intensity [W/m^2], I the ultrasound intensity [W/m^2] after the ultrasound has penetrated distance x , and x the penetration depth of the ultrasound into the tissue in

meters [m]. The equation for Q can be derived from taking the derivative with respect to x of both sides of the equation $= I_o e^{-2\alpha x}$. The equation for Q follows from the assumption that heating in the tissue is entirely due to energy loss from the ultrasound beam as it passes through the tissue. One of the main purposes of beam focusing in HIFU is to increase the ultrasound intensity at the focal point, effectively increasing Q by increasing I .

Modeling Heat Diffusion and Loss in Biological Tissue

The evolution of the heating inside the body as a function of time can be modeled using the bioheat transfer equation (14):

$$\rho c \frac{\partial T}{\partial t} = \nabla k(\nabla T) - W(T - T_o) + Q \quad (1.4)$$

where ρ is the density of the tissue [kg/m^3], c is the specific heat of the tissue [$\text{J}/(\text{kg}^*\text{C})$], k is the conduction coefficient [$\text{W}/(\text{m}^*\text{C})$], W is the perfusion coefficient [$\text{kg}/(\text{m}^3*\text{s})$], and Q is the applied power density from the ultrasound [W/m^3].

The bioheat transfer equation can be derived by tracking the heat flow through the body through conservation of energy. Read from left to right, the time derivative of the temperature vector is equal to the heat dispersion due to conduction plus the heat lost due to perfusion plus the heat deposited due to the ultrasound. The perfusion term is often called the Pennes term and is what makes the heat equation become the Pennes bioheat equation. In this model, the process of perfusion is modeled as a uniform heat sink that removes heat from the equation based solely on the temperature difference between the

tissue temperature and the ambient body temperature. This is in contrast to more complicated models of heat flow that model the perfusion term as a tensor that is dependent on the specific geometry of the underlying vascular network.

Modeling Heat Damage in Biological Tissue

Finally, the damage done to tissue due heating can be modeled using the empirical formula (15)

$$CEM = \int_{t_o}^{t_f} R^{T-43} dt \quad (1.5)$$

where CEM are the cumulative equivalent minutes of thermal dose delivered to the tissue, t_o is the integral starting time, t_f is the integral end time, T is the temperature of the tissue in Celsius, and dt time differential (in units of minutes), and R and 43 are empirically determined reference constants where $R = 4$ if $37 \leq T \leq 43$ degrees and $R = 2$ for $T > 43$ (16). This formula was derived from experiments in which cell cultures were heated and the percentage of cell populations remaining alive at intervals were recorded and fitted to the model using a computer program. While more refined models have been developed by subsequent research, this equation remains a good approximation for the amount of thermal energy that needs to be deposited in tissue in order to cause cell death, and it is still used by many researchers when investigating HIFU and other hyperthermia treatments.

Optimizing Treatment Times

In the process of mathematically optimizing treatments in order to reduce treatment times, there are several constraints that are often imposed to ensure the goals of treatment safety and efficacy. One such constraint to ensure treatment efficacy is that all tumor locations receive a minimum thermal dose by the end of the treatment.

Additionally, concern for the health of the normal tissue surrounding a tumor often dictates that safety constraints are imposed, whereby either a temperature limit or an accumulated thermal dose limit are set for the normal tissue (outside of a small “margin” near the tumor edges). A more detailed explanation of these requirements are available in several places, for example, in Chapter 2. Mathematically, the efficacy requirement can be expressed as:

$$\text{Min}(D_{Tumor}) \geq D_{floor} \quad (1.6)$$

Where D_{Tumor} is the thermal dose deposited in the tumor(15) by the end of the treatment and D_{Floor} is the minimum allowable thermal dose for an area to be “treated”. In most cases, value of D_{Floor} is taken to be 240 CEM (15).

Similarly, the safety requirement for a temperature constraint in the normal tissue can be expressed mathematically as

$$\text{Max}(T_{NT}) \leq T_{Limit} \quad (1.7)$$

where T_{NT} is the temperature in the normal tissue at any point during the treatment and T_{Limit} is the maximum temperature allowed for any part of the normal tissue.

As a corollary, the safety requirement for a maximum dose constraint in the normal tissue can be expressed as

$$Max(D_{NT}) \leq D_{Limit} \quad (1.8)$$

where D_{NT} is the maximum thermal dose deposited in the normal tissue by the end of the treatment and D_{Limit} is the maximum allowable thermal dose in the normal tissue at the end of treatment.

A tightly focused focal zone from a HIFU transducer typically has dimensions on the order of a 1mm diameter in the transverse direction and 1cm in the axial direction (for example, see (11)). As the typical dimensions for breast tumors are typically on the order of several cubic centimeters (17), it is often necessary to scan the focal zone between several points in a HIFU treatment. Indeed, in most HIFU treatments, the typical set of user-controllable parameters consist of the transducer power output (possibly as a function of time); the transducer power on and off times; and the focal zone size, shape, and path through the tumor, as explained more fully in other research (18).

For most HIFU treatments, the combination of the six user-controllable parameters mentioned above means that there are multiple treatment configurations possible on the same tumor geometry. Because the number of possible treatments scales as the factorial of the possible user-controllable variables, in practice it is not possible to evaluate every possible treatment for an initial tumor geometry. Therefore, it is usually

highly desirable to select a treatment from the large space of possible treatments through the use of an optimization scheme.

Many optimization schemes exist, and a comprehensive review of these schemes is beyond the scope of this work; although, it is available in several other places (19). In brief, most optimization schemes follow the same basic heuristic to find an optimized solution in a large treatment space:

1. Evaluate the objective function (possibly subject to one or more constraint functions) at a “starting guess.”
2. Use selection criteria to select a new point for evaluation.
3. Evaluate the treatment at the new point, possibly subject to constraints.
4. Repeat steps 2-3 until the stopping criteria have been met.

For the optimization schemes presented in this work, the evaluation criterion was the total treatment time (i.e., the treatments were optimized to minimize the total treatment time). Mathematically, this can be described as

$$t_{treatment} = \sum_{n=1}^N t_{heat_n} + t_{cool_n} \quad (1.9)$$

where $t_{treatment}$ is the total treatment time, t_{heat_n} is the heating time at position n and t_{cool_n} is the interpulse cooling time for the position n . The constraints on this objective were exclusively equations (1.4) and (1.5), although the use of equation (1.6) instead of equation (1.5) would also have been possible. New points were mostly selected by using an interior point method (19), sequential quadratic programming (19), or a heuristic grid

search algorithm (11). Stopping criteria were chosen as the convergence of the function to below a user specified tolerance.

Outline of Dissertation

The outline of the dissertation is as follows. Chapter 2 and 3 are papers that have been accepted and published by the International Journal of Hyperthermia (in 2011 and 2012). Chapter 4 is an addition to the main body of research in Chapter 3 that will be submitted for publication as a technical note in the near future. Chapter 5 contains the major conclusion of this work and directions for future research. The Appendices which follow Chapter 5 contain explanations of and examples of the code used for this research, simplified for user readability.

References

1. Fennessy FM, Tempany CM. MRI-guided Focused ultrasound surgery of uterine leiomyomas. *Academic Radiology* 2005;12(9):1158-66.
2. Hindley J, Gedroyc WM, Regan L, Stewart E, Tempany C, Hynnen K, et al. MRI guidance of focused ultrasound therapy of uterine fibroids: Early results. *American Journal of Roentgenology* 2004;183(6):1713-9.
3. Illing RO, Kennedy JE, Wu F, ter Haar GR, Protheroe AS, Friend PJ, et al. The safety and feasibility of extracorporeal high-intensity focused ultrasound (HIFU) for the treatment of liver and kidney tumours in a Western population. *Br J Cancer* 2005;93(8):890-5.
4. Hynnen K, Pomeroy O, Smith DN, Huber PE, McDannold NJ, Kettenbach J, et al. MR imaging-guided focused ultrasound surgery of fibroadenomas in the breast: A feasibility study. *Radiology* 2001;219(1):176-85.
5. Hesley GK, Felmlee JP, Gebhart JB, Dunagan KT, Gorny KR, Kesler JB, et al. Noninvasive treatment of uterine fibroids: Early mayo clinic experience with magnetic resonance imaging-guided focused ultrasound. *Mayo Clinic Proceedings* 2006;81(7):936-42.

6. Daum DR, Smith NB, King R, Hynynen K. In vivo demonstration of noninvasive thermal surgery of the liver and kidney using an ultrasonic phased array - Comparison of strategies using phased array systems. *Ultrasound Med Biol* 1999;25:1087-98.
7. Damianou C, Hynynen K. Focal spacing and near-field heating during pulsed high temperature ultrasound therapy. *Ultrasound Med Biol*. 1993;19(9):777-87.
8. McDannold NJ, Jolesz FA, Hynynen KH. Determination of the optimal delay between sonications during focused ultrasound surgery in rabbits by using MR imaging to monitor thermal buildup in vivo. *Radiology* 1999;211(2):419-26.
9. Coon J, Payne A, Roemer R. HIFU treatment time reduction in superficial tumours through focal zone path selection. *International Journal of Hyperthermia* 2011;27(5):465-81.
10. Payne A, Vyas U, Blankespoor A, Christensen D, Roemer R. Minimisation of HIFU pulse heating and interpulse cooling times. *International Journal of Hyperthermia* 2010;26(2):198-208.
11. Christensen DA. *Ultrasonic Bioinstrumentation*. New York: Harper & Row; 1988.
12. Pennes HH. Analysis of tissue and arterial blood temperatures in the resting human forearm. *Journal of Applied Physiology* 1948;1(2):93-122.
13. Sapareto SA, Dewey WC. Thermal dose determination in cancer therapy. *International Journal of Radiation Oncology Biol Phys* 1984;10:787-800.
14. Cheng KS, Roemer RB. Optimal power deposition patterns for ideal high temperature therapy/hyperthermia treatments. *International Journal of Hyperthermia* 2004;20(1):57-72. Epub 72.
15. Fisher B, Slack NH, Bross IDF, Investigators C. Cancer of the breast: Size of neoplasm and prognosis. *Cancer* 1969;24(5):1071-80.
16. Payne A. Minimization of thermal dose delivery time and development of an isolated kidney phantom: Applications for high intensity focused ultrasound [Ph.D.]. Utah: The University of Utah; 2008.
17. Nocedal J, Wright SJ. *Numerical Optimization*. Secaucus, NJ, USA: Springer; 1999.

CHAPTER 2

HIFU TREATMENT TIME REDUCTION IN SUPERFICIAL TUMORS THROUGH FOCAL ZONE PATH SELECTION

Reprinted with Permission from Informa UK Ltd.

International Journal of Hyperthermia, Vol. 27, No. 5, Pages 465-481

Joshua Coon, Allison Payne, Robert Roemer

RESEARCH ARTICLE

HIFU treatment time reduction in superficial tumours through focal zone path selection

JOSHUA COON¹, ALLISON PAYNE^{2,3}, & ROBERT ROEMER^{2,3,4}¹Department of Physics and Astronomy, University of Utah, Salt Lake City, ²Department of Mechanical Engineering, University of Utah, Salt Lake City, ³Utah Center of Advanced Imaging Research (UCAIR), University of Utah, Salt Lake City, and ⁴Department of Radiology, University of Utah, Salt Lake City, Utah, USA

(Received 22 May 2010; Revised 1 February 2011; Accepted 15 February 2011)

Abstract**Purpose:** This study evaluates the hypothesis that optimising the path of a high intensity focused ultrasound (HIFU) treatment's N focal zone heating pulses can significantly reduce treatment time, and identifies the underlying bio-thermal principles.**Materials and methods:** Thirty-one scanning paths were investigated using 3D simulations, with a minimum thermal dose delivered to every tumour position. Treatment time was calculated as the sum of the N, individually optimised heating and cooling periods. Tumours were superficial (skin to tumour distance ranging from 1.3 to 2.5 cm), but always deep enough so that the pre-tumour normal tissue was routinely heated to its constraint temperature (range: 42–45 °C). Properties were uniform and constant, and a range of blood perfusion and phased array powers were studied.**Results:** The best paths significantly reduced treatment times, with the largest gains occurring when (1) temperature superposition inside the tumour was maximised by successively heating the focal zone positions located in a 'stack' along the transducer's axis, and (2) the focal zone was moved laterally to an optimised location and another stack was applied. Stacking takes advantage of the focal zone's elongated shape, which produces axial temperature superposition within the tumour. Reduced tumour heating times also reduced energy deposition in the normal tissues, thus reducing or eliminating the need for inter-pulse cooling.**Conclusions:** HIFU treatment times can be significantly reduced by taking advantage of axial temperature superposition in tumours. Further reductions are obtained by correct choice of the transverse scan path.**Keywords:** High intensity focused ultrasound, MRgHIFU, path optimisation, simulations, treatment time**Introduction**

High intensity focused ultrasound (HIFU) has been shown to be a promising treatment method for several types of cancer and for uterine fibroids [3–8]. However, when considering large tumours embedded in critical normal tissues, the requirement of precisely placing and applying a large number of heating pulses can result in very long treatment times [3, 9, 10], with McDannold et al. [10] recommending at least 50–60 s of cooling between pulses and Fennessy and Tempny [3] using 20–40 s of heating followed by 80–90 s of cooling. For example, 100 pulses with 30 s of heating and 60 s of cooling per

pulse would take 2.5 h just for delivering the desired dose, not including treatment preparation time, adjustments and complications. Such long times pose a major challenge to HIFU's broad clinical acceptance. To reduce treatment times, clinicians can control: the electrical power delivered to the transducer; the sequence of focal zone positions; the heating pulses' periods; the inter-pulse cooling periods; and, for a phased array, the size and shape of the focal zone [11].

One way to reduce treatment times is to simultaneously optimise all of those parameters. However, because of the computational intensity involved

Correspondence: Joshua Coon, Department of Physics and Astronomy, University of Utah, Salt Lake City. Tel: (801) 427-1245. Fax: (801) 581-4801. E-mail: jcoo161@yahoo.com

ISSN 0265-6736 print/ISSN 1464-5157 online © 2011 Informa UK Ltd.
DOI: 10.3109/02656736.2011.564507

RIGHTS

in simultaneously optimising the large number of possible combinations of parameters, prior research [3, 4, 6, 10, 12–14] has commonly addressed a fixed treatment path and parametrically changed one of the other treatment variables, including the: applied power magnitude [13]; ultrasound frequency [13] and; inter-sonication delay period [10]. Most investigators have used fixed heating pulse and inter-pulse cooling periods to both provide standardised heating conditions and to avoid normal tissue overheating [3, 4, 6, 14–16]. Because of efficacy and safety concerns, such protocols used conservative heating and cooling periods, resulting in very long treatment times [6, 12]. To help reduce those times, recent research has developed an approach that minimises each individual pulse heating and inter-pulse cooling period during a treatment, resulting in significantly reduced treatment times [17]. That study also showed that larger applied powers always shortened treatments for focused transducers, a non-obvious result when normal tissue constraints are active. They employed the strategy of developing separate optimisation approaches for individual treatment parameters (e.g. heating and cooling periods), with the goal of eventually combining all individual approaches into a comprehensive optimisation approach. The current study extends the use of that strategy by optimising one more treatment variable, the focal zone scan path.

Only a few studies have investigated the effects of scan path, and none have been concerned primarily with treatment time – except Payne et al. [17] which only compared two paths. Fan and Hynynen [18] considered three two-dimensional planar paths applied sequentially to two planes perpendicular to the transducer's axis. They used fixed heating and cooling periods and thus did not study treatment time; however, they did show that the volume of tissue ablated was path dependent. Liu et al. [19] performed a numerical study of two heuristic paths (least possible distance and greatest possible distance between sequential small rapid scanning volumes) and showed that cumulative heating time differences (cooling times were fixed at 1 min between sonications) of several minutes were possible, depending on which path was used. More recently Kohler et al. [20], in an experimental study that was extended by Enholm et al. [21], and was based on that group's earlier work with nested spirals [22, 23], used a focal zone at a fixed axial depth that was rapidly electronically steered in concentric 2D circles going sequentially from inward to outward. They used fixed heating times for their circles and thus they did not provide any comparative information on optimal treatment times. Finally, in a 2D and 3D (spherical tumour) computational study, Malinen et al. [24] developed an optimisation algorithm that found the

scan path that minimised the total dose delivered to the tumour while guaranteeing minimal dose at all locations. Again, treatment time was not the study's focus, but a more uniform dose delivery would, presumably, help shorten treatments – a reasonable belief bolstered by comparison of their results to those from a 'standard, non-optimised' path.

In summary, while several investigators have studied the role of separate physical mechanisms in reducing treatment times, no study exists that concentrates on the effects of scan path on treatment time. Thus, although several different paths have been proposed and studied by individual investigators, at present no type of scan path has been shown to be preferable – regardless of differing claims by various investigators. The current research attempts to help shed light on this problem by providing direct comparisons of the treatment times needed by a range of scanning paths to treat the same tumours under simple, standard conditions of fixed, uniform tissue properties. Such results will help guide, and be a reference base for, future studies on more complex clinical situations.

Methods

The goals of this study were to determine whether significant treatment time gains could be obtained by optimising the scan path when significant normal tissue heating was present, and to identify the thermophysical mechanisms underlying those gains. To do so, numerous treatment scenarios were simulated using different scanning paths, tissue perfusions, transducer powers, tumour sizes and depths, and normal tissue constraints. In this study we concentrate on superficial tumours, but with all such tumours located at a sufficient depth so that there was sufficient 'pre-focal' normal tissue between the skin and tumour so that normal tissue overheating due to scanning-related thermal build-up was a significant factor in differentiating among scan paths.

Treatment time

Each scan path involved a sequence of N discrete focal zone locations, at each of which a heating pulse was applied and a subsequent power off, inter-pulse cooling period was initiated (if needed) to avoid heating the normal tissue past its constraint value (generally 43°C) during the next heating pulse. Each path's treatment time (t_{TREAT}) was calculated as the sum of its N heating and $N-1$ inter-pulse cooling periods:

$$t_{TREAT} = \sum_{n=1}^N (\Delta t_{HEAT,n} + \Delta t_{COOL,n}) \quad (1)$$

Here, $\Delta t_{heat,n}$ and $\Delta t_{cool,n}$ are the pulse heating period and the subsequent inter-pulse cooling period for the n th heating pulse. Each heating pulse was applied at the same total transducer power magnitude at every focal zone position within a tumour. In order to find the path that minimised t_{TREAT} a scan path was set, the pulse's heating and inter-pulse cooling periods were individually minimised at each of the N sequential focal zone positions, and t_{TREAT} was calculated and evaluated with respect to all other paths' treatment times values. To find the minimal heating and cooling times at each focal zone position, the simulations used the approach of Payne et al. [17] in which each pulse's heating period was made just long enough so that the desired thermal dose was delivered to the focal zone (as determined both during that heating pulse and during the immediately ensuing decay of the focal zone temperature); and power was then turned off during an inter-pulse cooling period that was also optimised. This approach ensured that every path studied was standardised to consistently meet the same important conditions; the same applied power magnitude was used for every pulse, and every heating and cooling period was individually optimised. The thermal dose [25] was monitored in the hottest voxel of the full width half maximum region of the focal zone's specific absorption rate (SAR) pattern, and the inter-pulse focal zone spacing was made small enough to ensure that the tumour was treated to at least 240CEM43°C at all locations (as verified after each treatment). Any 'prior dose' delivered (i.e. delivered to the current focal zone position during earlier heating of other focal zone positions) was subtracted from the target dose before the optimal heating and cooling periods were calculated. Conversely, no accounting for future dose was implemented. That is, the dose that will be delivered to the currently heated position by later pulses was not anticipated, an approach that results in the (clinically conservative) overdosing of some tumour locations. The metric used for comparing scan paths, the treatment time, is equivalent to a rate of thermal ablation when a fixed tumour volume is divided by the treatment time.

Thermal model

Temperatures were calculated using the Pennes bio-heat transfer equation [26]:

$$\rho C \frac{\partial T}{\partial t} = k \nabla^2 T - W C_b (T - T_b) + Q_{ext} \quad (2)$$

where T is temperature (°C), ρ is the tissue density (kg/m^3), C is the specific heat of tissue ($\text{J/kg}^\circ\text{C}$), k is the thermal conductivity of the tissue ($\text{W/m}^\circ\text{C}$), Q_{ext} is the applied power density deposited by an external applicator (W/m^2), W is the Pennes perfusion

parameter ($\text{kg/m}^3 \text{ s}$), C_b is the specific heat of blood and T_b is the arterial blood temperature. Although this equation has its limitations, it has been shown to adequately predict the major aspects of *in vivo* experiments [26–29]. An explicit finite-difference approximation of Equation 2 was implemented with a temporal resolution of one second and a spatial resolution of $3 \times 3 \times 1 \text{ mm}$. These resolutions are similar to those in Malinen's study [24] which used an isotropic 2-mm finite element nodal spacing, and 0.5-s time steps. Their preliminary studies showed that finer spatial resolutions did not significantly affect their results, a finding similar to ours for the 1-s time step. Also as in that study: all boundary conditions were kept at 37°C, as were the initial conditions; tissue properties were constant, and their computational region size was chosen to include the major features of the scanning process (primarily the heating of the proximal and distal normal tissues, and the tumour), while being mindful of the computationally intense optimisation problems being solved. The present study used a comparable computational region size for the same reasons. We applied a range of normal tissue temperature limits (42°, 43°, and 45°C) on constraint planes located 1 cm behind and in front of the tumour – which is the location where the maximum normal tissue temperatures almost always occurred due to thermal build-up, a phenomenon that is minimal in the transverse direction due to the rapid transverse fall-off of the focal zone's SAR pattern.

Power deposition

The power deposition pattern was determined as in Payne et al. [17] using the HAS (hybrid angular spectrum) method [30] to simulate the SAR field from an existing ultrasound phased array with 256 elements arranged randomly on a spherical surface (Imasonics, Besançon, France), with the focal zone steered electronically in the axial direction and mechanically in the transverse direction (Image Guided Therapies, Bordeaux France). The HAS method is an extension of the traditional angular spectrum method to inhomogeneous tissues and has been found to be both accurate and much faster computationally than other methods (i.e. the Rayleigh-Sommerfeld integral) [30]. The resulting focal zone size, expanded to adjust for scattering and transducer element variability, is $\sim 2 \times 10 \text{ mm}$ (FWHM) which is very close to that seen when using this phased array to heat agar phantoms and *ex vivo* tissues [31]. The simulated treatment geometry is shown in Figure 1.

Every tumour studied was treated with heating pulses at three focal zone depths along the transducer's axis (z direction). Thus, three electronically

steered power deposition distributions were simulated for each tumour, one for each focal zone depth. Each of those distributions was translated in the x-y plane at its fixed depth to obtain the SAR

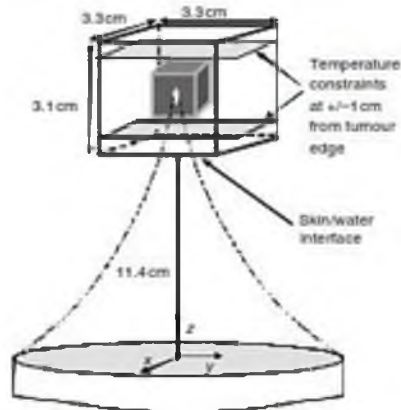


Figure 1. Geometry of the treatment domain. The origin is located in the centre of the transducer's face. The geometric focus of the transducer is at 13 cm and the water filled distance from the transducer to the skin is 11.4 cm (11.0 for some simulations, as measured from the centre of the face of the transducer). A small (1.1 cm³) and medium (2.6 cm³) volume tumour were studied with this geometry. A deeper medium and a larger (4.5 cm³) tumour were studied with a slightly modified geometry using an expanded simulation region.

distributions for the tumour's (N/3) transverse positions at that depth. This approach simulates mechanical scanning in the transverse directions. The focal zones' peak absorbed power density values (W/m³) used were all below the conservative limits set by the FDA [32] to avoid cavitation. For every scan pattern the total applied transducer power was the same at all N locations, and was fixed at a value that gave a maximum absorbed power density (in the hottest voxel) of 0.67×10^3 W/m³ when the focal zone was centred on the front plane of the small, superficial tumour studied (Figure 1). This power density value is close to optimal in the sense that lower values yield significantly longer treatment times, while larger values give only small gains in treatment times, a prior result [17] that was confirmed in the current study (Figure 6). The property values used are shown in Table 1.

Tumour models

Four tumour geometries were studied (Table II), labelled as small superficial, medium superficial,

Table 1. Thermal and acoustic properties used in all simulations [1, 2].

Thermal conductivity, k (W/m ² °C)	0.5
Specific heat, C (J/kg°°C)	4190 (blood and tissue)
Speed of sound, c (m/s)	1500 (tissue and water)
Attenuation coefficient, α (nPa/m/MHz)	4.8
Density, ρ (kg/m ³)	1000
Pennes' perfusion, W (kg/m ³ s)	0.5, 1.0–10

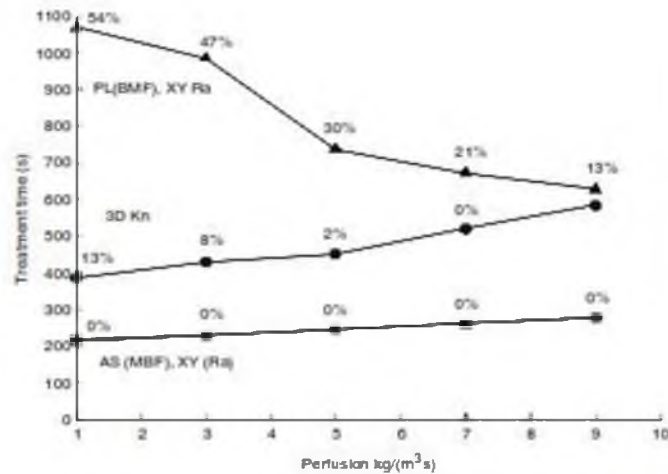


Figure 2. Treatment time vs. perfusion for three focal zone paths treating the small superficial tumour with 45 positions with the standard total applied power and a range of perfusions. Also shown are the percentages of the treatment time spent cooling the normal tissue. The lines are for the AS (MBF), XY (Ra) (squares); 3D Kn (circles) and PL (BMF), XY Ra (triangles) scan patterns.

medium deeper, and larger. The choice of geometries was made in order to provide (1) a reasonable range of sizes (the largest tumour dimension in the current study was ~ 2 cm, a value near the middle of the range for the largest tumour dimension representing approximately 1/3 of breast tumours [33]), (2) tumours at several depths, including depths where significant axial electronic steering was needed, with its concomitant focal zone SAR reduction, and (3) tumour sizes and dimensions similar to those used in other path studies, e.g. Liu et al. and Malinen et al. [19, 24]. The tissue region dimensions for the small and medium superficial tumours were $3.3 \times 3.3 \times 3.1$ cm, while for the medium deeper and larger tumours they were $3.3 \times 3.3 \times 5.1$ cm. These region sizes are close to those used by Malinen et al. [24]. To verify that the region size was large enough to prevent boundary condition induced changes in scan path rankings, multiple additional simulations were performed using a larger, region up to $1.8 \times 1.8 \times 1.4$ cm³. The larger region gave the same rank ordering of scan paths as the smaller region. The focal locations were spaced 3 mm apart in all three directions for all tumours except for the larger tumour, for which the focal zones were 6 mm apart in the *z*-direction. The 3-mm axial spacing had considerable axial SAR overlap among the three axial focal zone positions within a 'focal zone stack' and was thus a conservative spacing ensuring that all voxels within the tumour achieved a minimum dose of 240 CEM. This matches the recommendation of a previous study [18] that some focal zone overlap is present to avoid untreated regions in the tumour. This 3-mm spacing is on the same order as the 2-mm spacing between focal zones used by Fan et al. [34] (which is more conservative than the 5-mm axial and 3-mm lateral spacing used by Hynynen [6]), and is similar to the 4-mm inner annulus diameter used by Kohler et al. [20]. The 6-mm axial spacing used in the larger tumour provided a larger spacing that could treat the tumour in a reasonable amount of treatment time while still providing enough SAR overlap to avoid regions of untreated tumour tissue between focal zones.

Finally, for the more difficult to treat 'medium deeper' and 'larger' tumours a higher normal tissue temperature limit was used (45 °C) for the constraint locations, which were deeper in the tissue and thus further from the skin's nerve endings. Post-treatment analysis of the normal tissue temperatures showed that this higher limit (imposed to speed treatments) was approximately equivalent to a 30 CEM dose limit. Even though the tumours studied were superficial, near-field thermal build-up activated the normal-tissue tissue constraints requiring interpulse cooling for approximately 90% of the paths studied.

Scanning paths

Due to the extremely large number of possible paths (approaching N) an exhaustive search was not practical. The 31 paths studied are a combination of ones that are exactly or roughly equivalent to those used previously [13, 14, 18, 20, 24], plus several that appeared promising due to potentially improved tumour heating and/or decreased normal tissue heating. The paths are broadly categorised as: axially stacked (AS), planar (PL), and 3-dimensional (3D). Within each category multiple patterns were studied, as summarised in Table III, while Figures 3 and 4 show example patterns.

For the axially stacked patterns, when the transducer is located at a given transverse (X-Y) location these patterns first treat all three axial focal zone positions in an ordered 'stack' (e.g. successively in a straight line along the *z*-axis in one of the six possible sequences involving the back (B), middle (M), and front (F) treatment depths). That axial stack sequence is then repeated at multiple, sequential, transverse locations which, taken together, cover the complete tumour. These transverse patterns include raster scans, which have been used by [5, 18], Annular scans, which have been applied clinically in hyperthermia treatments and HIFU experiments [20, 22, 35–37], and knight jumps (the L-shaped moves from a chess game), which were studied in an attempt to reduce normal tissue cooling times by using a transverse pattern that had a fixed distance

Table II. Simulation configurations. All distances are given in cm from the transducer's centre, the transducer's geometric focus is at 13 cm, and all dimensions are in cm. The coordinate order is X, Y, Z.

	Small	Medium, superficial	Medium, deeper	Larger
Number of FZs	45	108	108	108
Treatment grid	$3 \times 5 \times 3$	$6 \times 6 \times 3$	$6 \times 6 \times 3$	$6 \times 6 \times 3$
Skin distance	11.3	11.4	11.0	11.0
Treatment plane distances	12.7, 13.0, 13.3	12.7, 13.0, 13.3	13.5, 13.8, 14.1	12.4, 13.0, 13.6
Constraint plane distances	11.7, 14.3	11.7, 14.3	12.5, 15.1	11.4, 14.6
Tumour dimensions	$1.5 \times 0.9 \times 0.8$	$1.8 \times 1.8 \times 0.8$	$1.8 \times 1.8 \times 0.8$	$1.8 \times 1.8 \times 1.4$
NT constraint (°C)	43	42, 42.5, 43	45	45
Distance from tumour to skin	1.3	1.3	2.5	1.4

Table III. Scanning patterns studied: F indicates the front position in an axial stack, or the front plane in a planar scan; M and B indicate the middle and back. MBF indicates that the M position (or plane) was treated first, etc.

Axially stacked (AS) scans		Planar (PL) scans		
Axially stacking order	Transverse scan pattern of stacks	Order in which planes are treated	Scan pattern within each plane	3-Dimensional (3D) scans
All six permutations of F, M and B	XY raster	MBF, BFM, and BMF	XY raster	XYZ knight
MBF and MFB	Concentric annuli: all six permutations of L, M and O	LMR	XZ raster	Maximum distance first
MBF	Adjacent annuli: squares and rectangles	FBM	XY knight	Maximum distance last
MBF and MFB	XY knight			Random

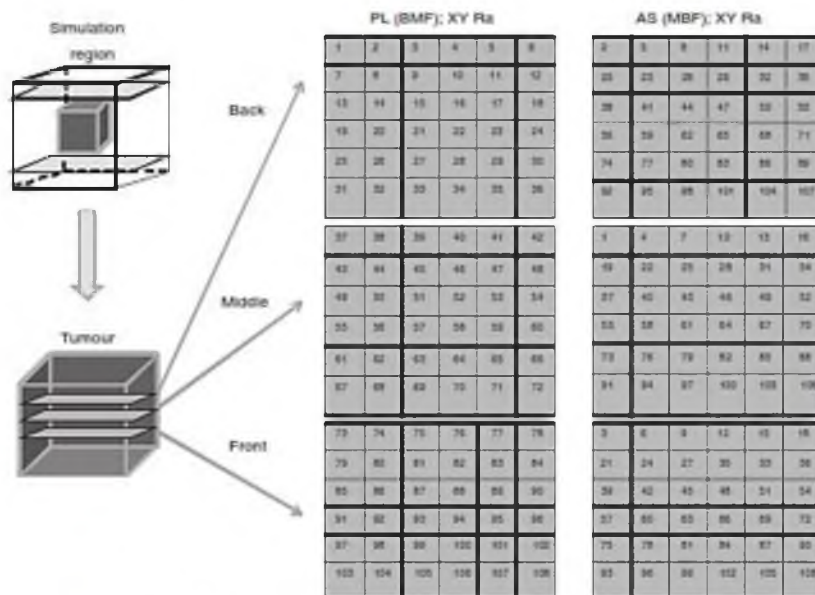


Figure 3. The successive focal zone locations for: (Left) the 'planar (BMF); XY raster' path, in which the back plane is treated first with an X-Y raster scan, then the middle plane and then the front plane; (Right) the 'axially stacked (MBF); XY raster scan' in which the transducer is fixed at one transverse (X-Y) location and the focal zone is electronically scanned through the stack of three axial M, B and F locations. The transducer is then moved through the remaining transverse locations in an XY raster pattern, applying the same axial stack order at each location. The numbers specify the order in which the focal zone positions were scanned.

between successive stacks that is close to the largest that can be consistently applied between all pairs of successive stacks throughout the complete treatment.

For the planar scans, axial stacking was not used and each of the three transverse planes (one at each axial depth; B, M and F) was scanned completely with a transverse pattern before moving to the next plane. In a very few cases three different planes were scanned (with left (L), middle (M), and right (R)

signifying the planes as referenced to a plane containing the transducer's axis).

The 3D patterns (which, like the planar scans, did not use axial stacking) provided the opportunity to utilise larger distances between successive heating pulse locations, including (1) a maximum distance first (3DMaxFirst) path, which maximised the distance between successive FZ locations (i.e. the first two pulses occurred at the ends of the longest

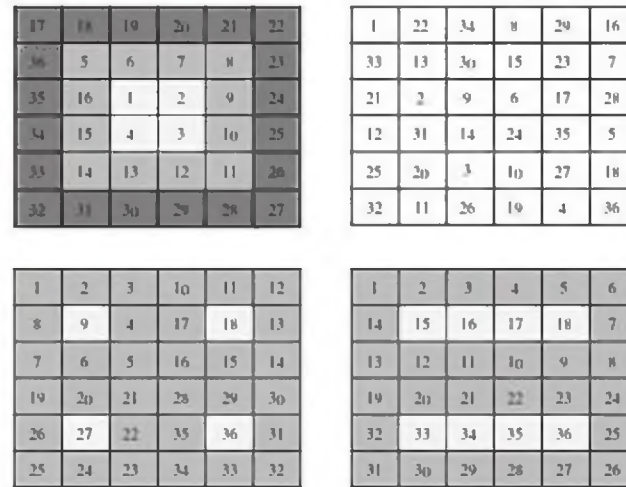


Figure 4. Axial view of four transverse, XY paths used to scan an axial stack: inner middle outer (IMO), concentric annuli (top left), knight (top right), adjacent square annuli (bottom left), and adjacent rectangular annuli (bottom right).

diagonal in the treated volume, etc.), resulting in numerous small separations at the end of the treatment, (2) a '3DMaxLast' path (generated by reversing the order of the maximum first path), and (3) a '3D knight' path, generated with 3D knight jumps between successive (x, y, z) focal zone locations, thus providing a relatively large fixed distance between all successive scan locations for the complete treatment. Finally, 100 randomly generated 3D paths were studied for the small superficial tumour.

Elemental reference cases

Four elemental reference cases that are composed of 'building blocks' from which more complex paths are constructed were developed and are presented in Appendix A. These cases serve as a reference base against which to compare the treatment time gains seen in the individual paths developed below.

Results

Results are presented in terms of the scan path treatment times. For most cases the 'standard treatment conditions' of a fixed applied transducer power level (giving a front treatment plane maximum power density of $0.66 \times 10^7 \text{ W/m}^2$ for the superficial tumour), a perfusion magnitude $0.5 \text{ kg/m}^3\text{s}$ (typical for muscle tissue [1]), and a 6°C normal tissue constraint temperature were used. Due to the large number of paths and treatment conditions studied,

and the lengthy computations required for the optimisation of the heating pulse and inter-pulse cooling period at every focal zone position along each path, computation times of over a week on a large, multicore computing node were sometimes required to find the treatment time for a single path. Thus, when it was clear that a scan path being studied had treatment times far from optimal (e.g. the optimal treatment time was already significantly exceeded after only half of the tumour was scanned), the treatment times were extrapolated to an estimated final time, and the results indicated by asterisk.

Effects of scan path

To illustrate the large effect of scan path, Figure 5 presents the treatment times for fourteen scan paths with the standard treatment conditions for the medium superficial tumour. Clearly the axially stacked X-Y raster scans with the heating pulses starting in the middle of each stack (the AS (MFB), XY Ra and AS (MBF), XY Ra scans) are the fastest, with treatment times that are a factor of 5.5 better (6.7 vs. 36.7 min) than the worst case simulated, i.e. the PL (BMF), XY raster scan that successively treats the back, middle and front planes with XY raster scans. (They are also a factor of 4.5 better than the case of all N pulses applied independently, i.e. than the 'independent pulse' case given in the appendix (6.7 vs. 30 min).)

The small superficial tumour was also studied with most of the paths in Figure 5, and the resulting

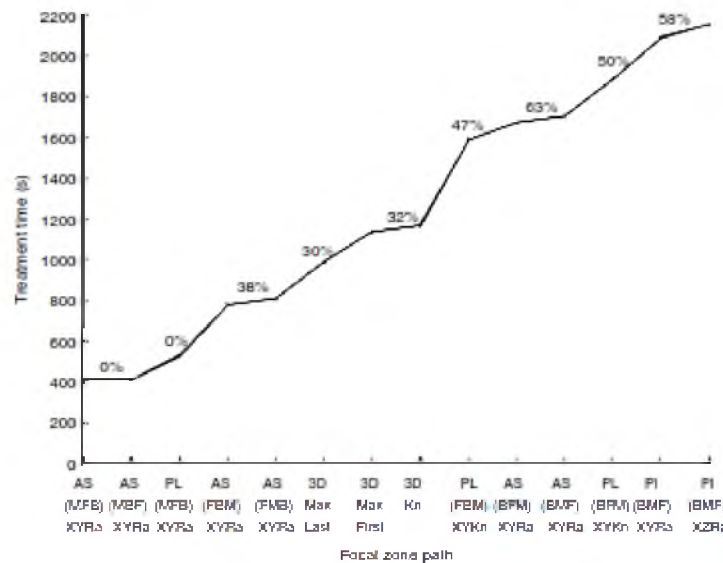


Figure 5. Treatment time vs. scanning path type for the medium superficial tumour (108 focal zone positions) and the standard treatment conditions. Also shown are the percentages of the treatment time spent cooling the normal tissue. When the cooling time percentages are nearly identical, only one value (located between the paths with similar values) is shown.

relative path rankings were unchanged from those in Figure 5. The small superficial tumour was also treated with 100 randomly generated paths, with their treatment times all lying roughly midway in the relative path rankings.

Effects of applied power and perfusion

Figures 6 and 2 show the effects of applied power and perfusion magnitude on the treatment times and the relative rankings of the scan paths. Results are shown for one of the best (AS (MBF), XY Ra), worst (PL (BMF), XY Ra) and middle (3DKn) scans from Figure 5. (The other scans from Figure 5 that were studied at different powers and perfusions followed the trends in Figures 6 and 2, and are thus not shown.) The trends of decreasing treatment times with increased power in Figure 6 are the same as shown previously [17] and illustrate why the standard power density level of $0.66 \times 10^7 \text{ W/m}^2$ was chosen – since larger powers yield only marginal treatment time gains, while lower powers greatly increase the treatment times. Figure 2 shows that for the best cases (e.g. AS (MBF), XY Ra scan) for which no normal tissue constraints are activated even at low perfusions, increasing the perfusion magnitude provides no additional benefit in the normal tissue and makes it harder to heat the tumour, thus

increasing the treatment times. Conversely, for the slowest scan patterns (e.g. the PL (BMF), XY raster scan), which already have long treatment times at low perfusions (since they activate the normal tissue constraints so frequently), increasing the perfusion cools the normal tissue, and thus reduces the treatment times. A small number of scans were also performed in a tumour model with heterogeneous perfusions, where the tumour perfusion level was twice the normal tissue perfusion. These scans used a subset of the paths described above, and in all cases the ranking of the paths was unchanged from those in Figure 5.

To illustrate why the axially stacked scans have the shortest treatment times and other scans have much longer treatment times, Figure 7 shows the heating and cooling times at each successive position for the AS (MBF), XY Ra and the PL (BMF), XY raster paths for the medium superficial tumour. In Figure 7A, the benefits of axial stacking can be seen by noting that the axially stacked case has one long (initial) heating pulse (at M) followed by two much shorter pulses (at B and F) within each axial stack. The short pulses arise since axial stacking allows for sequential pulses to build up the tumour temperatures (before they decay) in the direction in which the most SAR overlap can be utilised, i.e. axially stacking takes advantage of the elongated nature of

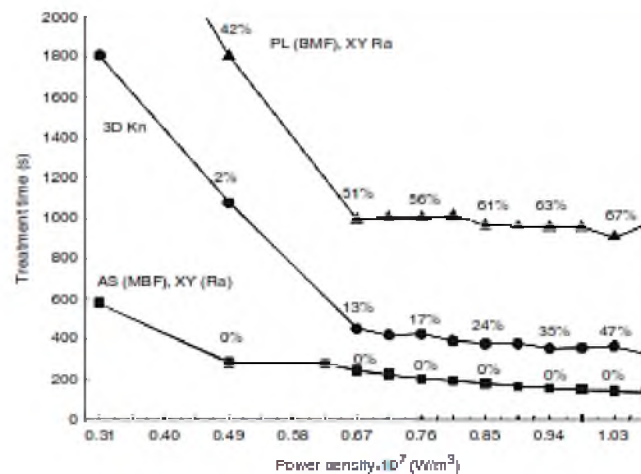


Figure 6. Treatment time vs. power density for three scan paths treating the small superficial tumour with 45 positions. The standard perfusion and constraint values were used but the total applied power was varied. Also shown are the percentages of the treatment time spent cooling the normal tissue. The lines are for the AS (MBF), XY (Ra) (squares); 3D Kn (circles) and PL (BMF), XY Ra (triangles) scan patterns.

the focal zone. In contrast, the PL (BMF); XY raster path has nearly constant long heating times at each focal zone position in every plane (Figure 7A) since it does not take advantage of such SAR overlap. In addition, it treats the back plane first, thus spending the most time (the first pulses) at locations for which the ratio of SAR in the focal zone to that in the normal tissues is the lowest, thus activating the inter-pulse cooling much more frequently. Figure 7B shows how these longer heating times for this planar scan result in much longer inter-pulse cooling periods. A second trend in Figure 7A is the steady reduction in heating times as the treatment progresses for both scan patterns, corresponding to increased thermal build-up in the tumour, an effect present for both scan patterns, but to different degrees.

The bio-physical mechanism by which the treatment time benefits are gained through axially stacking is illustrated in Figure 8, which shows the temperature vs. time curves in the centre of the first focal zone treated (M) for a heating pulse applied to the middle of the larger tumour. It also shows the corresponding curves for the voxels that are immediately proximal (F), distal (B) and transversely adjacent to the focal zone. Here one can see that if after heating the middle position, the focal zone is rapidly moved to the front position for the second heating pulse, that the temperature elevations resulting from the second pulse will be superimposed on the already significantly elevated tumour temperatures at the front position, and thus the front pulse will need a much shorter heating period. Since this

superposition occurs at high temperatures it also takes maximum advantage of the gains to be obtained from the non-linear temperature-thermal dose relationship, thus further reducing the needed heating times. Similar but smaller heating time gains would occur if one immediately moved to the back position when applying the second pulse. However, if one moved off-axis by a transverse motion, then not only would there only be a small amount of temperature gain due to superposition, but also the temperatures in the front and back axial locations would be allowed to decay, and thus when they are heated at a later time, long heating periods will be required to bring them back up from basal conditions to the desired target temperature. Such longer heating times will increase the energy deposited in the normal tissues, thus necessitating additional inter-pulse cooling times (as can be seen in Figure 7B for the PL (BMF), XY Ra scan), thus further lengthening the treatment times. Finally, the largest time gains arise from heating the middle position first since this generally maximises the total power (and energy) deposition in the tumour during the first (and longest) axial heating pulse, thus producing a larger 'pre-heated' temperature base at the other two axial focal zone locations.

Transverse path patterns of axially stacked scans

Since the axially stacked scans starting in the middle position gave the shortest treatment times for a wide range of conditions when studied with the XY

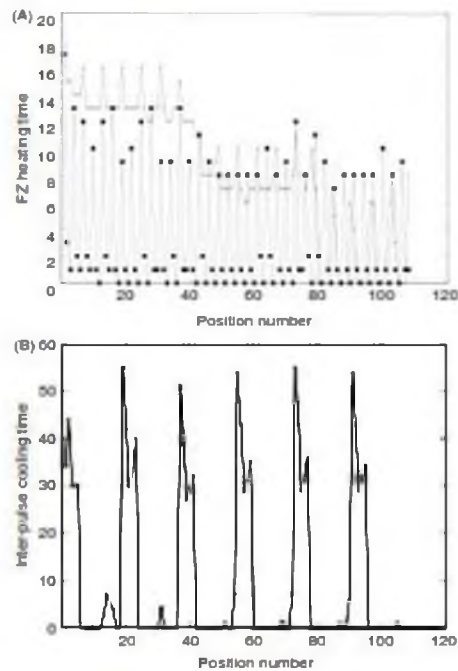


Figure 7. Pulse heating and inter-pulse cooling times (s) during treatment of the medium, superficial tumour under the standard treatment conditions: (A) The heating times at each sequential focal zone position for both the axially stacked (MBF), XY raster path (squares) and the planar (BMF), XY raster path (x). (B) The cooling times at each sequential focal zone position for the planar (BMF), XY raster path. The cooling times for the axially stacked (MBF), XY raster are not shown because they are zero for almost all positions in the treatment and are only a few seconds for the remaining positions.

transverse raster path treating the superficial tumours, additional transverse patterns were studied with the AS (MBF) axial stacking sequence to see if further treatment time gains could be realised. These treatments were performed on the medium superficial tumour with standard treatment conditions. In addition, since a primary safety concern in treatment is thermal build-up in normal tissues, in order to study more difficult treatment conditions the more stringent normal tissue temperature limit of 5 °C was also studied. Figure 9 shows (ranked in order of the treatment times for the 5 °C limit) the resulting treatment times for the following axially stacked AS (MBF) transverse scan patterns: AS (MBF) XY raster; the AS (MBF) adjacent annuli; the six permutations of the AS (MBF) O, M and I annuli for the concentric annuli scans; and the AS (MBF)

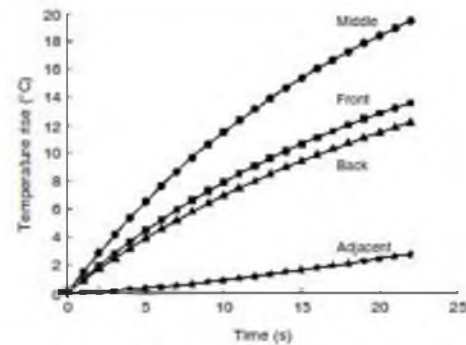


Figure 8. Temperature vs. time for the middle, front, back, and transversely adjacent (to either side of the middle position in the plane perpendicular to the transducer axis) locations with respect to the FZ location when the beam is focused on the middle (M) position. Results are shown for the first heating pulse for the larger tumour under standard treatment conditions.

XY knight jumps. In the 6 °C constraint case there was essentially no inter-pulse cooling needed for any scan patterns (the adjacent square annuli case used 3% of the time for cooling; all others were zero or <1%), and thus normal tissue considerations were not significant. For the 6 °C constraint case, all of the transverse scan patterns had very similar treatment times, and as expected since tumour heating was the dominant consideration, the fastest scan paths were generally those with the most adjacency among focal zone stacks (the adjacent square annuli had the shortest treatment time – 418 s) while the longest treatment times had the least adjacency (the AS (MBF) XY knight pattern – 469 s). However, once the normal tissue constraint conditions become very active (i.e. the 5 °C limit), then path choice became significant, and the ordering of the paths essentially reversed – with the path with the least focal zone adjacency (knight) becoming the fastest and the path with the most adjacency (squares) becoming the slowest. This change clearly illustrates the problem dependency of the optimal scan paths when normal tissue constraints are very active. It should also be noted for this 5 °C normal tissue constraint that while all transverse patterns (except the adjacent square annuli) still gain from tumour temperature superposition (their treatment times are less than the 1860 s independent pulses treatment time – see Appendix A), some paths lose part of that advantage due to activation of the inter-pulse cooling periods. This is evidenced by the monotonically increasing cooling times as the treatment time increases. Finally, for this stricter normal tissue constraint limit, the shortest treatment times are for the AS (MBF) transverse patterns of concentric annuli

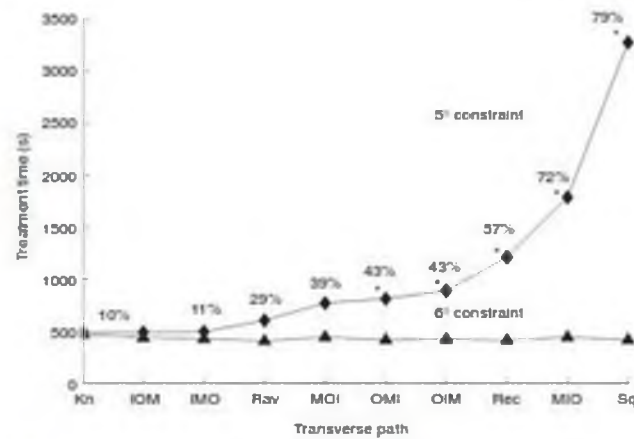


Figure 9. Treatment time vs. transverse scan path for axially stacked (MBF) stacks treating the medium, superficial tumour for 6°C and 5°C normal tissue temperature limits under the standard treatment conditions. The scans are rank ordered based on their times for the 5°C constraint case. The path abbreviations are: Kn for the AS (MBF) XY knight jumps; inner I, middle M, outer O for the AS (MBF) concentric annuli; Ra for the AS (MBF) XY raster; Rec for the AS (MBF) adjacent rectangular annuli; and Sq for the adjacent square annuli. Paths where the treatment times were extrapolated have an asterisk. The percentages of treatment time spent cooling the normal tissue for each path with the 5°C limit are shown. The percentages for the 6°C limit are not shown because they were all less than 3% and were not a significant factor in determining total treatment time.

starting at the tumour centre (IMO and IOM); the XY knight jumps; and the XY raster scan. Note that at the 5°C limit these four patterns have treatment times that are less than the treatment times for all of the Figure 4 cases at the 6°C limit (except the AS (MBF) and AS (MFB) raster scans), so no other patterns from Figure 4 were worth running since their treatment time would only increase if run with the 5°C limit. These four transverse patterns are an interesting combination of quite different transverse scans which all balance the goal of optimising the gains from increased adjacency inside the tumour, with avoiding overheating the normal tissues due to SAR overlap in the near field.

Deeper and larger tumours: SAR overlap

To study the effects of path selection in other, more difficult to treat situations, treatments were also performed on the medium tumour moved to a deeper location and on an axially larger tumour. Since the 6°C constraint limit resulted in large amounts of normal tissue thermal build-up and thus impractically long treatment times for these tumours, the NT constraint temperature was set at 8°C for these studies. (This 8°C temperature constraint is approximately equivalent to a thermal dose limit of 30CEM43°C since in retrospectively examining the results for these cases, a NT dose of greater

than 30 CEM was observed for at most one NT voxel in every treatment.) Figure 10A and B show the resulting treatment times for the medium deeper tumour and the larger tumour for the four fastest transverse scanning patterns from Figure 9, i.e. the AS (MFB): XY knight jumps; IOM and IMO concentric annuli; and XY raster. The results for these medium and deeper tumours differentiate these four transverse paths even further, showing that the AS (MFB) XY raster and AS (MFB) IMO concentric annuli paths are the most consistently fast scans for all cases examined. Finally, scan path treatments were also performed on both this medium deeper and this larger tumour using all other five permutations of (M, F, B) for the axially stacked XY raster path. In all cases, the treatment times were slower than for the corresponding MFB scans, thus reinforcing the optimal nature of the MFB axially stacking sequence.

In order to better understand the effects of transverse path on treatment times, the heating times for each axial stack during the treatment (i.e. for all 36 stacks) for each of the five paths of Figure 10 are shown in Figure 11 (A–E), where stacks which were preceded by a previous stack requiring a long cooling time (>30 s) are marked with a tilde. The heating time of the initial stack for all paths was 39 s and decreased for later stacks in all paths as focal zone adjacency came into play and

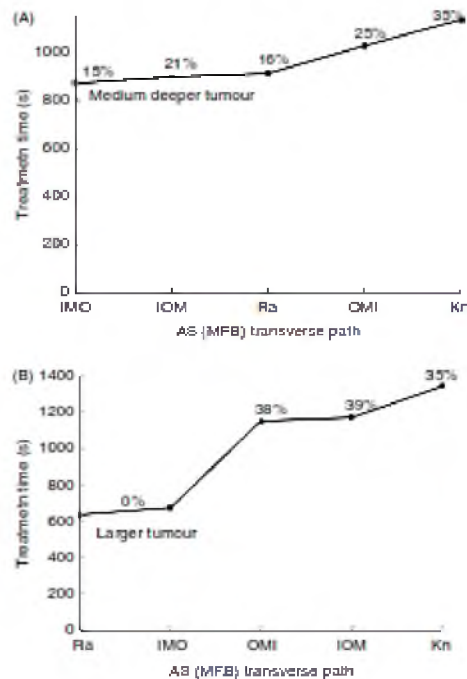


Figure 10. Treatment time (s) vs. transverse path for (A) the medium deep (top) and (B) larger tumour (bottom) for the standard treatment conditions and a NT temperature limit of 8 °C. The independent single pulse treatment times for these tumours are 3852 and 2556 s, respectively (Appendix). The percentage of treatment time spent cooling is shown above each path (or between points in cases where the percentages were essentially identical).

thermal build-up in the tumour accumulated. Also note the 'spikes' in the heating time that occurred either after a long cooling period or because of a large change in the path position that reduced the adjacency between successive focal zone stacks.

Discussion

The results presented confirm this study's primary hypothesis, that large treatment time reductions can be realised by judicious scan path selection, at least for the tumours and conditions studied herein. They also identify and quantify the effects of the underlying thermo-physical principles that make scan paths 'fast', thus providing guidance for future studies with more complicated conditions (e.g. changing blood flow and attenuation coefficients). The most important effect is 'axially stacking' of successive focal

zones in the tumour, which arises from the combination of axial SAR overlap and temperature superposition due to the focal zone's elongated shape. More specifically, the MFB axially stacked paths studied are generally fastest since they apply their longest heating pulse (M, the initial pulse of each stack) when the focal zone is depositing the most power inside the tumour, and then move to the tumour location that was preheated the most (F) by the initial pulse in order to take maximum advantage of temperature superposition in the tumour. This effect is shown to hold for a wide range of perfusion and transducer power levels, and multiple tumour conditions that activate the normal tissue constraints. In summary, while most previous scan-related studies have concentrated on the problem of avoiding thermal build-up in the normal tissues by having successive focal zone locations spread far apart, the current study shows how in many cases the completely opposite approach of placing successive pulses close together (in an axial stack and with maximum stack adjacency) can shorten treatment times considerably.

The second most important thermo, physical factor, is adjacency of successive transverse stacks, an effect important in treatment paths used in other research [20]. The effect of adjacency can best be seen by comparing the heating times for the AS (MFB) XY knight path (Figure 11E) which has little adjacency, to the other AS (MFB) paths of Figure 11 which all have considerable adjacency. This reduced adjacency leads to much longer average stack heating times for the AS (MFB) XY knight pattern at the start of the treatment, and thus creates longer treatment times both directly because of those longer heating periods and indirectly because the normal tissue is also being heated for longer times. This results in higher normal tissue temperatures and an increased need for inter-pulse cooling following later heating pulses.

The current study concentrates on superficial tumours with fixed properties, and extends previous treatment time optimisation studies by showing that the time gains from path selection add to those obtained by optimising the individual pulse heating and cooling times [17]. The results shed light on the best approach for treating the presented tumour configurations, and provide a basis for further studies with more complicated conditions. An interesting topic for such future studies is temporally changing tissue properties, both changing tumour and normal tissue perfusion, and increased tumour attenuation. Attenuation changes have been observed both experimentally [38–40] and when matching simulation data to previous experimental results [41]. The scan-related convention that has been followed by several previous investigators is to treat from the back to the

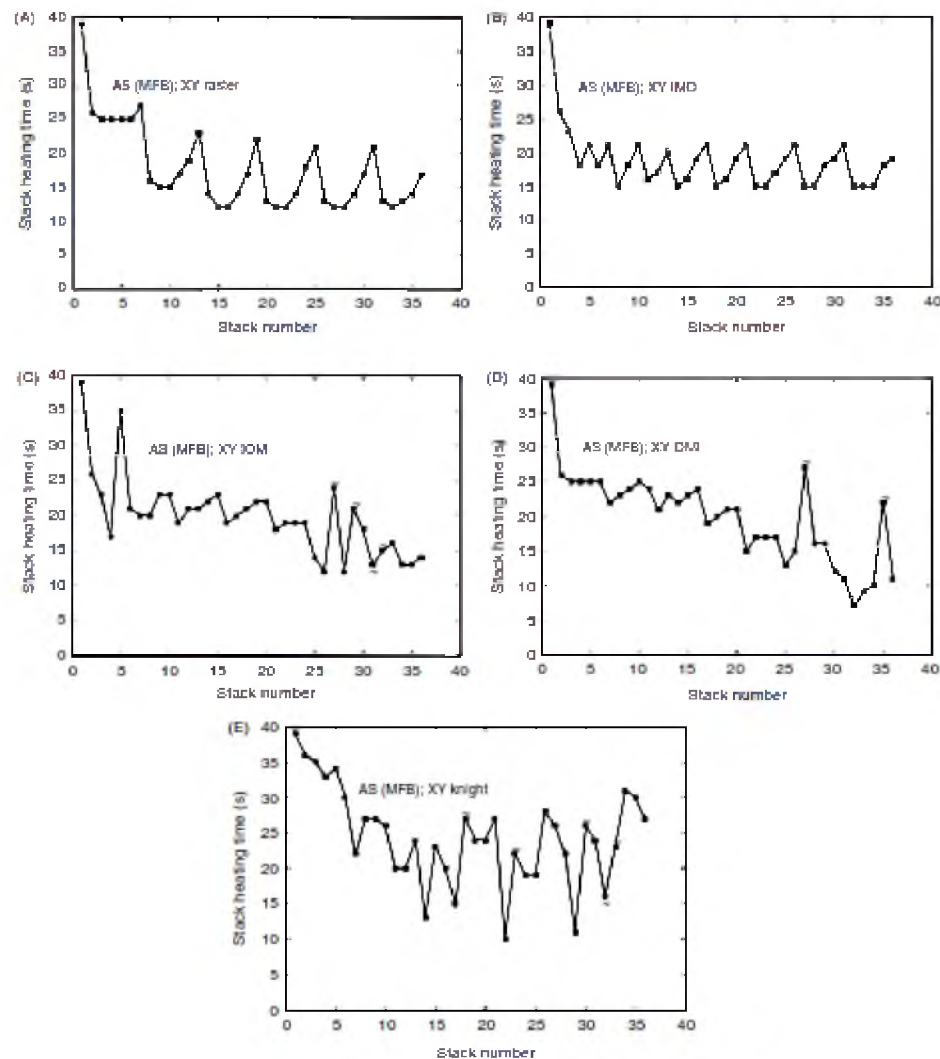


Figure 11. The stack heating time vs. stack number for the pads in Figure 10. The graphs, in order from shortest to longest treatment time, are for the AS (MFB): (A) raster, (B) IMO concentric annuli, (C) IOM concentric annuli, (D) OMI concentric annuli, and (E) knights. Cooling times of greater than 30 s in a preceding stack are marked with a tilde.

front in a tumour (e.g. using a planar BMF, XY raster scan), with the idea being that if the front of the tumour is treated first that any resulting increased attenuation would block the ultrasound from reaching the deeper positions. The current study indicates that if indeed such a PL (BMF), XY raster scan strategy is adopted, that treatment times will be

very long. Thus, it is important to study this question in much more depth in the future to quantify the treatment time trade-offs involved. While several studies have begun investigating tissue attenuation changes during thermal therapy treatments, much remains to be determined experimentally *in vivo* before definitive conclusions can be drawn about the

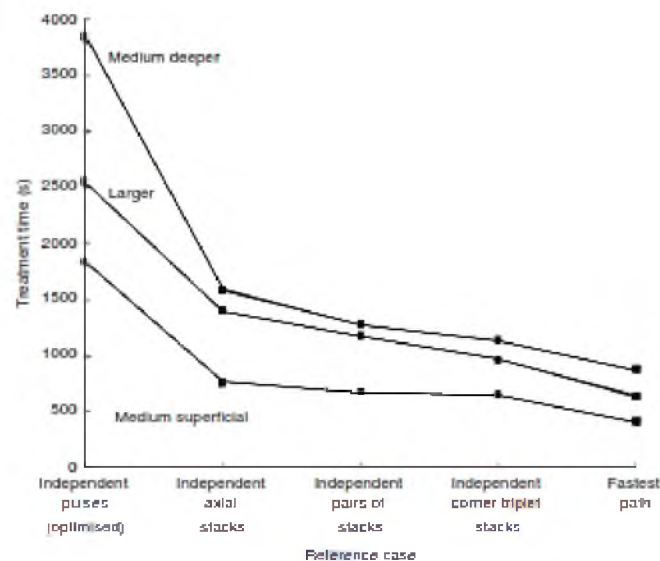


Figure 12. Treatment time vs. reference case for the medium superficial, medium deeper, and larger tumour treated with 'independent' pulses and stacks under the standard treatment conditions. Also shown are the times for the fastest scans obtained in this study for the same treatment conditions. The fastest case for each of the tumours was: A5 (MFB) NY raster for both the medium superficial tumour and for the larger tumour, and A5, MFB IMO concentric annuli for the medium deeper tumour.

role of attenuation change in path optimisation. In particular, the speed with which attenuation changes occur during an *in vivo* HIFU treatment is not precisely known (i.e. whether such changes occur within seconds of ablation or on a scale of minutes, etc.). Previous *ex vivo* studies have shown that the level and rate of tissue attenuation changes due to thermal ablation depend on the temperature to which the tissue is heated [42–46], the frequency of the ultrasound beam [40, 43, 44, 46], and both the rate of dose delivery and the maximum dose delivered [42], with tissue attenuation changing more after it has been heated and then cooled, vs. when it is kept in a heated state [45]. Further study is needed to determine what affect tissue attenuation changes have on the optimal path choice, and whether an axial treatment which starts in the middle of the tumour could be sufficiently 'fast' to treat an axial stack before the tumour's attenuation changes significantly. However, the evidence presented in Figure 4 shows that, if further research shows that tissue attenuation changes are both fast enough and large enough in magnitude to make a back-to-front focal zone path necessary for some treatments, starting with a back treatment plane and axially stacking the focal zones is still faster than a transverse raster scan path that does not use axial stacking.

Similar timing and magnitude considerations are present for possible changes in tumour and normal tissue perfusion changes during treatments.

Overdosing (tumour positions above 240CEM) was also examined but was found, both through post-treatment analysis and exploratory simulations on selected paths, to not be a significant enough effect to change the rank ordering of the paths presented for the treatment conditions studied herein – although reductions in treatment times would be possible on all paths through the reduction of overdosing. Avoiding large amounts of overdosing in practice could only be done by anticipating all future doses to be delivered to a given position, a difficult task that would rely on accurate modelling. The problems of overdosing and attenuation changes are interrelated; that is, attenuation changes will likely be very significant in treatments that go to very high temperatures and thus deliver very high tumour doses (with concomitant overdosing for treatment efficacy 'insurance').

One of the main results from the simulations conducted in this paper was an examination of the physics present in treatment paths that have significant levels of axial stacking. Even though the temperature increase due to this stacking may vary for a particular treatment, the results of these

simulations lend credence to the belief that the underlying physics of axial stacking and stack adjacency will be a useful tool for treatment acceleration in many, and more complicated, clinical situations. In summary, these results provide useful guidelines for reducing treatment times through path selection in many tumours, and a reference base for future studies of more complex situations, e.g. for treating larger, deeper tumours with heterogeneous perfusions, irregular geometries and temporally changing properties. Given the very large treatment time gains realised in the current study, it is reasonable to expect that by applying the basic bio-thermal approaches identified in this study, those gains will translate, in some proportion, to other cases. Given the immense scope of an exhaustive search over all tumour anatomies and physiologies, transducer configurations, focal zone sizes and shapes and spacing, and NI paths for any tumour, it is unlikely that a truly universally optimal scan path will ever be found, nor be needed since it is likely that some 'close to optimal' patterns will give practical treatment times.

Conclusion

Optimisation of the focal zone scan path in HIFU treatments yields significant treatment time savings. The optimised treatment paths use axially stacked (along the transducer axis) focal zones, with each such stack starting with the focal zone in the tumour centre. These time savings occur primarily because the optimised axial focal zone stacks take advantage of SAR overlap and temperature superposition in the tumour in successive axial focal zone heating pulses. The tumour is generally best treated by multiple such stacks scanned through the tumour in an optimised transverse pattern that maximises the amount of 'stacking adjacency', with the best path being dependent on the normal tissue constraints. These time gains are present over a range of transducer powers and tissue perfusion levels, and for several different tumour configurations. Such treatment time reductions will be very important clinically, thus motivating further path studies and searches for even better thermophysics-based heuristic guidelines for a wider range of expected clinical conditions.

Acknowledgements

We greatly appreciate the help of Dennis Parker, Urvi Vyas, and Doug Christensen, and use of the UCAIR facilities for this work. An allocation of computer time from the Center for High Performance Computing at the University of Utah is gratefully acknowledged.

Declaration of interest: This work was partially supported by grants from NIH (R01-CA134599), Siemens Medical Solutions, the Focused Ultrasound Foundation, a University of Utah Synergy Grant and the Ben B. and Iris M. Margolis Foundation. The authors alone are responsible for the content and writing of the paper.

References

1. Chao JC, Lee RC. The future of biothermal engineering. In: Diller RK, editor. Heat and Mass Transfer in Living Systems. New York: New York Academy of Sciences; 1998. pp 1-20.
2. Christensen DA. Ultrasonic Bioinstrumentation. Chichester: Wiley; 1988.
3. Fennessy FM, Tempney CM. MRI-guided focused ultrasound surgery of uterine leiomyomas 1. Acad Radiol 2005;12:1158-1166.
4. Hindley J, Gedroyc WM, Regan L, Stewart E, Tempney C, Hynnen K, et al. MRI Guidance of Focused Ultrasound Therapy of Uterine Fibroids: Early Results. Am J Roentgenol 2004;183:1713-1719.
5. Illing RO, Kennedy JE, Wu F, ter Haar GR, Protheroe AS, Friend PJ, et al. The safety and feasibility of extracorporeal high-intensity focused ultrasound (HIFU) for the treatment of liver and kidney tumours in a western population. Br J Cancer 2005;93:890-895.
6. Hynnen K, Pomeroy O, Smith DN, Huber PE, McDannold NJ, Kretschbach J, et al. MR imaging-guided focused ultrasound surgery of fibroadenomas in the breast: A feasibility study. Radiology 2001;219:176-185.
7. Hesley GK, Feltner JP, Gebhart JB, Dunagan KT, Gony KR, Kessler JB, et al. Noninvasive treatment of uterine fibroids: Early Mayo Clinic experience with magnetic resonance imaging-guided focused ultrasound. Mayo Clinic Proc 2006;81:936-942.
8. Doria DR, Smith NB, King R, Hynnen K. In vivo demonstration of noninvasive thermal surgery of the liver and kidney using an ultrasonic phased array - Comparison of strategies using phased array systems. Ultrasound Med Biol 1999;25:1087-1098.
9. Damianou C, Hynnen K. Focal spacing and near-field beaming during pulsed high temperature ultrasound therapy. Ultrasound Med Biol 1993;19:777-787.
10. McDannold NJ, Jolesz FA, Hynnen KM. Determination of the optimal delay between sonications during focused ultrasound surgery in rabbits by using MR imaging to monitor thermal buildup in vivo 1. Radiology 1999;211:419-426.
11. Roemer R, Payne AJ. Minimization of HIFU dose delivery time. Paper presented to the International Society of Therapeutic Ultrasound conference, Seoul, Korea, 12-15 June 2007.
12. McDannold N, Tempney CM, Fennessy FM, So MJ, Rybicki FJ, Swann EA, et al. Uterine leiomyomas: MR imaging-based thermometry and thermal dosimetry during focused ultrasound thermal ablation. Radiology 2006;240:263-272.
13. Wu F, Chen WZ, Bai J, Zou JZ, Wong ZL, Zhu H, et al. Pathological changes in human malignant carcinoma treated with high-intensity focused ultrasound. Ultrasound Med Biol 2001;27:1099-1106.
14. McDannold, Hynnen K, Wolf D, Wolf G, Jolesz F. MRI evaluation of thermal ablation of tumors with focused ultrasound. J Magn Reson Imaging 1998;8:91-100.

15. Xiaobing F, Hynynen K. Ultrasound surgery using multiple sonifications – Treatment time considerations. 1996;22: 471–482.
16. McDannold N, Jolesz FA, Hynynen K. Determination of the optimal delay between sonifications during focused ultrasound surgery in rabbits by using MR imaging to monitor thermal build-up in vivo. *Radiology* 1999;211:419–426.
17. Payne A, Vyas U, Blankespoor A, Christensen D, Roemer R. Minimisation of HIFU pulse heating and interpulse cooling times. *Int J Hyperthermia* 2010;26:198–208.
18. Fan X, Hynynen K. Ultrasound surgery using multiple sonifications – Treatment time considerations. *Ultrasound Med Biol* 1996;22:471–482.
19. Liu H-L, Lin W-L, Chen Y-Y. A fast and conformal heating scheme for producing large thermal lesions using a 2D ultrasound phased array. *Int J Hyperthermia* 2007;23:69–82.
20. Kohler MO, Mougnot C, Quesson B, Enholm J, Le Bail B, Laurent C, et al. Volumetric HIFU ablation under 3D guidance of rapid MRI thermometry. *Med Phys* 2009;36:3521–3535.
21. Enholm JK, Kohler MO, Quesson B, Mougnot C, Moonen CTW, Sotkka SD. Improved volumetric MR-HIFU ablation by robust binary feedback control. *IEEE Trans Biomed Eng* 2010;57:103–113.
22. Mougnot C, Salomez R, Palussière J, Grenier N, Moonen CTW. Automatic spatial and temporal temperature control for MR-guided focused ultrasound using fast 3D MR thermometry and multi-spiral trajectory of the focal point. *J Magn Reson Med* 2004;52:1005–1015.
23. Mougnot C, Quesson B, Senneville B, Oliveira PLd, Sprinkhuizen S, Palussière J, et al. Three-dimensional spatial and temporal temperature control with MR thermometry-guided focused ultrasound (MRgHIFU). *Magn Reson Med* 2009;61:603–614.
24. Malinen M, Hänninen T, Kaipio JP, Hynynen K. Scanning path optimization for ultrasound surgery. *Phys. Med. Biol.* 2005;50:3473–3490.
25. Sapareto SA, Dewey WC. Thermal dose determination in cancer therapy. *Int J Radiat Oncol Biol Phys* 1984;10: 787–800.
26. Pennes HH. Analysis of tissue and arterial blood temperatures in the resting human forearm. *J Appl Physiol* 1948;1:93–122.
27. Moros EG, Dutton AW, Roemer RB, Burton M, Hynynen K. Experimental evaluation of two simple thermal models using hyperthermia in muscle in vivo. *Int J Hyperthermia* 1993;9:581–598.
28. Rawnsley RJ, Roemer RB, Dutton AW. The simulation of discrete vessel effects in experimental hyperthermia. *J Biomech Eng* 1994;116:256–262.
29. Roemer R. Thermal dosimetry and treatment planning. In: Gauthier M, editor. *Thermal Dosimetry*. Berlin: Springer; 1990. pp 119–214.
30. Vyas U, Christensen D. Ultrasound beam propagation using the hybrid angular spectrum method. In: *Proceedings of the EMBC 30th Annual International Conference of the IEEE*. Vancouver: EMBC, 2008. pp. 2526–2529.
31. Todd N, Payne A, Parker D. 3-D MR temperature imaging with model predictive filtering reconstruction. *Proceedings of the 17th Annual ISMRM Scientific Meeting and Exhibition*. Honolulu: Curran Associates, 2009. p. 445.
32. FDA. Information for manufacturers seeking marketing clearance of diagnostic ultrasound systems and transducers. 2009. Available at <http://www.fda.gov/MedicalDevices/DeviceRegulationandGuidance/GuidanceDocuments/ucm089001.htm> (accessed 2011).
33. Fisher B, Slack NH, Bross IDF cooperating investigators. Cancer of the breast: Size of neoplasm and prognosis. *Cancer* 1969;24:1071–1080.
34. Fan X, Hynynen K. A study of various parameters of spherically curved phased arrays for noninvasive ultrasound surgery. *Phys Med Biol* 1996;41:591–608.
35. Hynynen K, Shimizu D, Anhalt D, Stea B, Sykes H, Cassidy JR, et al. Temperature distributions during clinical scanned, focused ultrasound hyperthermia treatments. *Int J Hyperthermia* 1990;6:891–908.
36. Hynynen K, Roemer R, Anhalt D, Johnson C, Xu ZX, Swindell W, et al. A scanned, focused, multiple transducer ultrasonic system for localized hyperthermia treatments. *Int J Hyperthermia* 1987;3:21–35.
37. Shimizu D, Hynynen KH, Anhalt DP, Roemer RB, Cassidy JR. Scanned focused ultrasound hyperthermia: Initial clinical results. *Int J Radiat Oncol Biol Phys* 1988;15: 1203–1208.
38. Zderic V, Keshavarzi A, Andrew MA, Vazay S, Martin RW. Attenuation of porcine tissues in vivo after high-intensity ultrasound treatment. *Ultrasound Med Biol* 2004;30:61–66.
39. Keshavarzi A, Vazay S, Kaczowski PJ, Keilman G, Martin R, Chi EY, et al. Attenuation coefficient and sound speed in human myometrium and uterine fibroid tumors. *J Ultrasound Med* 2001;20:473–480.
40. Worthington AE, Trachtenberg J, Sherar MD. Ultrasound properties of human prostate tissue during heating. *Ultrasound Med Biol* 2002;28:1311–1318.
41. Kolios M, Sherar M, Hunt J. Temperature dependent tissue properties and ultrasonic lesion formation. *Adv Heat Mass Transf Biotech* 1999;44:113–118.
42. Damiannou CA, Sanghvi NT, Fry FJ, Maass-Moreno R. Dependence of ultrasonic attenuation and absorption in dog soft tissues on temperature and thermal dose. *J Acoust Soc Am* 1997;102:628–634.
43. Clarke RL, Bush NL, Ter Haar GR. The changes in acoustic attenuation due to in vitro heating. *Ultrasound Med Biol* 2003;29:127–135.
44. Gertner MR, Wilson BC, Sherar MD. Ultrasound properties of liver tissue during heating. *Ultrasound Med Biol* 1997;23:1395–1403.
45. Techavipoo U, Varghese T, Chen Q, Stiles TA, Zagzebski JA, Frank GR. Temperature dependence of ultrasonic propagation speed and attenuation in excised canine liver tissue measured using transmitted and reflected pulses. *J Acoust Soc Am* 2004;115:2859–2865.
46. Worthington AE, Sherar MD. Changes in ultrasound properties of porcine kidney tissue during heating. *Ultrasound Med Biol* 2001;27:673–682.

Appendix A

Four cases that represent the most elemental 'building blocks' used to construct all 31 of the scans studied are presented to investigate the thermo-physical mechanisms underlying the scans' differences in treatment times. These idealised cases include 'independently optimised': (1) pulses; (2) single axial stacks; (3) pairs of adjacent axial stacks; and (4) corner triplets of adjacent axial stacks. All reference stacks used MFB axially stacking since this stacking order always gives the shortest treatment times of all six stacking orders. All four of these cases are 'independent' in the sense that for the independent pulses, each pulse is applied under the idealised conditions that it is not affected by, i.e. is independent of, all other pulses. Such pulse

'independence' could arise if there was a high blood perfusion everywhere, and the sequential heating pulses were widely separated in space so they did not affect each other. Similarly for independent stacks, each stack is applied so that it is not affected by any other stacks, and similarly for the pairs and triplets of stacks. Each case is 'optimised' since the pulse heating and inter-pulse cooling periods are optimised separately for each case. That is, the independent single pulse case uses one heating pulse period that is optimised for the independent heating of one location, the independently optimised single axial stack has three heating periods and two cooling periods that are optimised for the treatment of the three axial positions within one independent stack, etc.

Independently optimised single pulses

If each heating pulse was independent of all other pulses then it would begin its heating pulse with the tumour at basal conditions and treat its focal zone location to the needed dose, but would have no effect on any other location. This means that there would be no treatment time gains at that location from 3D SAR overlap among successive pulses, nor from long term thermal build-up in the tumour, nor from the delivery of prior or future dose. Similarly, there would be no treatment time delays from inter-pulse cooling since there would be no thermal build-up in the normal tissues (i.e. $\Delta t_{\text{Cool},n} = 0$ for all n) other than from the single pulse, which will not require inter-pulse cooling by definition. The resulting treatment time is thus N times the independent pulse's optimised heating time, which is the same for all pulses due to their independence.

Independently optimised single axial stacks

Next, a series of 'independent' MFB stacks, whose three pulse heating and two inter-pulse cooling times were optimised within that stack, was studied. This approach takes advantage of SAR overlap and temperature superposition within the tumour to reduce the second and third pulse heating times (when compared to the first pulse). In the tumours studied it also resulted in some normal tissue thermal build-up due to the three heating pulses, but never enough to reach the constraint temperature, so normal tissue thermal build-up was not a consideration ($\Delta t_{\text{Cool},n} = 0$ for all n). There is no interaction with other stacks, and thus there is no long-term thermal build-up in the tumour or in the normal tissues. The difference between this case's treatment times and the independent single pulse case's treatment times is thus a measure of the heating time gained by using axial stacking. The resulting total treatment time is $N/3$ times the optimised

independent axial stack heating time, which is the same for all stacks due to their independence.

Independently optimised pairs of adjacent axial stacks

Next, since in most transverse scan patterns studied, successive stacks are placed adjacent to each other (in x or y , but not diagonally), those pairs gain from their adjacency (the second stack will have lower heating times since it will have been preheated by SAR overlap heating and transverse conduction from the first stack). If such pairs are independent, they will have interactions between themselves, but not with any other stacks. Comparing the treatment time for the optimised independent pairs of adjacent stacks to that for independent single axial stacks gives a measure of the time gains obtained solely from the 'two stack adjacency'. The resulting treatment time is $N/6$ times the heating time needed to heat one such pair of stacks, which is the same for all such pairs due to their independence. Again, for this case, the normal tissue constraint temperature was never reached during the six pulses used by a pair of stacks, and thus $\Delta t_{\text{Cool},n} = 0$ for all n .

Independently optimised corner triplets of axial stacks

Finally, the sequence of three adjacent stacks that form corners (e.g. stacks 1, 2 and 3 at the beginning of the AS (MFB), IMO pattern of Figure 3) not only gain from the immediate adjacency of each pair of successive stacks, but also from the diagonal heating between stacks 1 and 3. When compared to the paired stack times they give a measure of the time gains realised solely from adding a third stack to form a 'corner triplet'. Their treatment time is $N/9$ times the time required for one such triplet. Again, in these cases there is little thermal build-up due to the nine heating pulses and thus normal tissue constraints were never activated ($\Delta t_{\text{Cool},n} = 0$ for all n).

The 'reference case' results for the standard treatment conditions are presented (Figure 12) to both show the gains attainable from the different 'building blocks' scanning approaches, and as a baseline for comparison with the results for the 31 paths studied. Also shown are the results from those paths (out of all of the 31 paths studied) with the shortest treatment times. Note that those 'fastest' paths have the additional benefits (not present in any of the 'independent' reference cases) of both (1) thermal build-up in the tumour, a benefit that results in further shortening of the treatment times, and (2) accounting for 'prior dose' to reduce treatment times. These results clearly illustrate the gains achievable through optimising the use of the thermal physics (primarily axial stacking and secondarily stack adjacency) during treatment path selection.

CHAPTER 3

HIFU TREATMENT TIME REDUCTION THROUGH HEATING APPROACH OPTIMIZATION

Reprinted with Permission from Informa UK Ltd.

International Journal of Hyperthermia, Vol. 28, No. 8, Pages 799-820

Joshua Coon, Nick Todd, Robert Roemer

RESEARCH ARTICLE

HIFU treatment time reduction through heating approach optimisation

JOSHUA COON¹, NICK TODD^{1,2}, & ROBERT ROEMER^{2,3,4}¹Department of Physics and Astronomy, University of Utah, Salt Lake City, ²Utah Center for Advanced Imaging Research (UCAIR), University of Utah, Salt Lake City, ³Department of Mechanical Engineering, University of Utah, Salt Lake City, and ⁴Department of Radiology, University of Utah, Salt Lake City, Utah, USA

(Received 30 March 2012; Revised 6 October 2012; Accepted 8 October 2012)

Abstract

Purpose: This study evaluated the HIFU treatment time reductions available for several scan paths when optimising the heating approach used (single, discrete pulses versus volumetric scanning) and the paths' focal zone heating locations; number (N_{cycles}), spacings, sequencing order, number of heating cycles (N_{cycles}), and heating times. Also evaluated were the effects of focal zone size, increased tissue absorptivity due to heating, and optimisation technique.

Materials and methods: Treatments of homogeneous constant property tumours were simulated for several simple generic tumour shapes and sizes. The concentrated heating approach (which delivered the desired thermal dose to each location in one discrete heating pulse ($N_{\text{cycles}}=1$)) was compared to the fractionated heating approach (which dosed the tumour using multiple, shorter pulses repeatedly scanned around the heating path (i.e. 'volumetric scanning' with $N_{\text{cycles}}>1$)). Treatment times were minimised using both simultaneous, collective pulse optimisation (which used full a priori knowledge of the interacting effects of all pulses) and sequential, single pulse optimisation (which used only the information from previous pulses and cooling of the current pulse).

Results: Optimised concentrated heating always had shorter treatment times than optimised fractionated heating, and concentrated heating resulted in less normal tissue heating. When large, rapid tissue absorptivity changes were present (doubled or quadrupled immediately after heating) the optimal ordering of the scan path's sequence of focal zone locations changed.

Conclusion: Concentrated heating yields significant treatment time reductions and less normal tissue heating when compared to all fractionated scanning approaches, e.g. volumetric scanning.

Keywords: HIFU, treatment planning, treatment optimization, focal zone size

Introduction

HIFU has been shown to be a promising treatment modality for several types of cancer and uterine fibroids [1–8]. While many factors will affect its ultimate clinical acceptance, long treatment times [9, 10], sometimes several hours [5], can present a serious obstacle to wider clinical implementation. This limitation will become increasingly important when larger malignant tumours (whose irregularly shaped volumes must be completely dosed) in critical locations are treated. Reductions in treatment time are possible through user selection of the HIFU treatment operating parameters, including: the transducer power; the pulse heating times; the focal zone

(FZ) location(s) in the tumour; the order in which these locations are treated; the number of times they are each heated; and the focal zone size and shape. Finding an optimised set of treatment parameters that will make a given treatment short enough to be clinically viable presents a complicated problem. Although many studies have looked at treatment time as a factor when studying HIFU treatments, including studies on dose homogeneity inside of the tumour and new transducer systems [11–22], only a few studies have focused solely on the development of a set of optimal treatment scanning parameters to specifically reduce treatment time [23–26]. The problem is made

Correspondence: Dr Joshua Coon, Department of Physics and Astronomy, University of Utah, 115 South 400 East, Salt Lake City, UT 84112-0830, USA. Tel: 801-581-0901. E-mail: coon@eng.utah.edu

ISSN 0265-6736 print/ISSN 1464-3857 online © 2012 Informa UK Ltd.
DOI: 10.3109/02656736.2012.738846

especially difficult because the large dimensionality of the problem combined with long computational times makes a 'brute force' search through all treatment parameter space unfeasible [25]. Because of this difficulty with exhaustive searches for optimal treatment parameters, previous research has optimised each user-selectable parameter independently [23, 25]. So far, optimisation research specifically focused on minimising treatment time has been done on the transducer power levels [23], heating and cooling times at each position [23], and the path of the focal zone through the tumour [25].

This study expands that research to compare treatment times of a concentrated and a fractionated pulse heating approach (defined below). It does so while also studying the effects of an increasing number of focal zone heating locations used to heat a tumour of a fixed size (focal zone packing density), and for a range of focal zone spacings, both axial and transverse, for a fixed number of focal zones heating a tumour of a fixed size. Additionally, this study investigates the effects of heating-induced absorptivity changes on the optimal path for treatments using focal zones in an axial stack.

Concentrated versus fractionated focal zone heating

The question of whether to use a single heating pulse to completely deliver a desired total therapeutic thermal dose to each successive focal zone location individually before moving to another location (herein called concentrated heating), versus an approach that successively passes the focal zone over a fixed set of positions in a cyclical fashion that only delivers a fraction of the desired thermal dose to each location during each such pass (herein called fractionated heating) has been the subject of much speculation. These two approaches have different advantages and disadvantages. This paper concentrates on comparing the speed with which they can treat tumours under comparable conditions in order to determine which approach has the potential to be clinically faster. Although several speculative claims have been made regarding treatment speed, no systematic studies have been performed to evaluate their relative heating times under comparable conditions. Many HIFU applications have used concentrated heating in simulations, animal experiments and clinical treatments [4, 16, 17, 27–37]. The concentrated HIFU method was developed, in part, to overcome the long treatment times present in standard hyperthermia [30, 38] by using small, concentrated, high power density focal zones that produced high temperatures in short times. By heating tissues rapidly, that approach both reduced the time available for cooling to occur and took advantage of the non-linear temperature versus

thermal dose relationship [30, 39]. Concentrated heating was also introduced to reduce the cooling effects of the (unknown) tumour blood flow [30, 31] by inducing more dependence on thermal conduction. Unknown blood flow effects are now less of a concern since the temperatures present during treatments can be measured with magnetic resonance imaging (MRI) [4, 40–42]. One way to obtain more concentrated treatments is to use a more highly focused beam with a tight focus (with dimensions of approximately 1 mm by 5 mm, e.g. [4]). However, such smaller focal zones require treatment of a larger number of focal zone locations to cover a given tumour, potentially resulting in more heating in the normal tissue due to build up from the larger number of points heated [43, 44].

Other research [21, 45–50] has subsequently modified the concentrated heating approach in one of two ways. First, investigators have studied the use of a larger focal zone (produced either electronically or mechanically) that is then scanned discretely through a reduced number of locations [46, 47, 50]. Focal zones as large as $1 \times 1 \times 2 \text{ cm}^3$ [47] have been used, and one simulation study investigated the use of a large, single focal zone that was optimally shaped to yield a uniform thermal dose in the tumour, thus potentially minimising the total energy needed to treat the tumour [51]. Second, other investigators have proposed using a single focal zone (or multiple foci) to rapidly scan a large volume by using repetitive heating pulses that cyclically heat a sequence of focal zone locations (called volumetric scanning), including extensive research on animal models [21, 45, 49]. These volumetric heating approaches use rapid electronic switching to repeatedly progress through successive treatment locations, and have the potential advantage of giving a more uniform temperature distribution in the tumour. However, problems exist with this approach as well. Due to the smaller power density ratio between the tumour and that in the normal tissue, more near-field heating may occur in these treatments, a trend noted by Damianou and Hynynen [31]. Also, when trying to minimise treatment times, research has indicated [23, 25] that it is always desirable to have the maximum possible power density at each treatment location to take advantage of both the reduced time available for cooling and the non-linear rate of thermal dose deposition, factors whose effects are reduced by the dilution of power present in the larger, or repeatedly scanned, focal zone approaches. Finally, some researchers have investigated a mix of concentrated and diluted focal zones in simulation studies [52].

Though strong opinions exist regarding which treatment strategy (concentrated or fractionated) will achieve optimal results when considering a treatment time metric, little work has been done to directly

compare the two methods. This paper directly compares these methods with the end goals of both gathering quantitative evidence on, and explaining the underlying physics of both heating approaches, in order to help resolve this timing question.

Focal zone packing, spacing and scanning path

Most studies using a discrete scanning approach use conservative spacings between focal zone locations to avoid thermal dose 'holes' of untreated tissue inside the tumour, with a spacing of about 3 mm laterally [4, 25] and 5 mm or less axially between treatment planes [4, 25, 28] being typical. However, little work has been done on treatments that employ a more aggressive axial and transverse spacing, and little work has been done on the trade-offs involved between the optimal spacing of a smaller number of focal zones versus increasing the focal zone packing density. This need reflects a similar need for systematic studies of different focal zone sizes, which have only been studied for a few isolated cases, often as part of a larger study whose main focus is another phenomenon [11, 17, 20, 22, 53, 54]. Thus, the effect of focal zone size on treatment time remains unclear.

Several previous studies [11, 13, 23, 25, 45, 49, 50] have examined the effect of scanning path in magnetic resonance guided high intensity focused ultrasound (MRgHIFU) treatments. However, much work remains to be done in this area, including an examination of the path when other parameters, including the spacing between focal zone locations in the tumour, have been optimised. The results of previous research strongly suggest that, even in non-optimal scanning conditions, repeated use of 'axial stacking' of the focal zones (e.g. where an initial focal zone is placed in the centre of the tumour and subsequent focal zones are placed proximal/distal to this focal zone in a 'stack' along the axis of the transducer) can dramatically reduce treatment times.

Tissue absorptivity changes during treatment

Increases in the ultrasound absorptivity coefficient as a result of heating have been observed both experimentally [55–57] and when matching simulation data to experimental results [58]. Previous *ex vivo* studies have shown that both the magnitude and the rate of increase in the tissue ultrasound absorptivity coefficient due to heating depend on the temperature to which the tissue is heated [59–63], the frequency of the ultrasound beam [57, 60, 61, 63], and both the rate of dose delivery and the maximum thermal dose delivered [59]. However, little research has been performed on the quantitative effects of these changes on HIFU treatments, including whether the presence of absorptivity changes will increase or

decrease treatment times, or alter the optimal path for a given treatment. The only guideline present for such choices is the general observation that if very large absorptivity changes are present during a treatment, that treating the proximal tumour locations first should be avoided since the subsequent ultrasound pulses will possibly not be able to then penetrate to the more distal tumour locations [58]. However, though this conclusion is logical given its assumptions, the definition of 'very large' still remains to be quantified, as does the temporal speed with which absorptivity changes occur relative to a treatment's scan times. It has, however, been shown that tissue absorptivity changes more after it has been heated and then cooled versus when it is kept in a heated state [62]. That study showed the absorptivity increasing up to, and plateauing at, values of up to twice the unheated values.

Optimisation technique

Several previous studies have examined the problem of optimising HIFU treatments using a variety of techniques and objectives [13, 25, 26, 64–68]. The objectives used for HIFU optimisation generally have the primary goal of either shaping the thermal dose delivered to the tumour and the surrounding tissue [13, 26, 64–68] or of reducing treatment time through parameter optimisation while treating a fixed volume to a desired dose [25, 26]. The optimisation techniques previously used include an adjoint approach (in one dimension) [64], a series of simulated treatments that step through the parameter space at fixed values [65], use of a cost function-based algorithm to minimise tumour overdosing [13, 67], an analytical solution for the thermal dose distribution in a single pulse treatment [66], and a sequential optimisation technique that optimises treatment times at each location without considering future dose [25] beyond the current pulse's effects. This research expands on previous research by comparing two techniques for optimising HIFU treatments to minimise treatment times: the sequential optimisation technique used in previous research [25] and a method of 'simultaneous, collective pulse optimisation' that uses all available knowledge for a given treatment, including the *a priori* knowledge of the heating due to and thermal dose deposited by all pulses during a treatment, to optimise treatments. That latter technique is similar to that used in previous research [13].

Methods

Treatment time and tissue constraints

The total time needed to administer a treatment (which served as the objective function for the

optimisation routine) was calculated as the sum of its focal zone location pulse heating times plus (if necessary to prevent normal tissue damage) the related inter-pulse cooling times:

$$t_{\text{treatment}} = \sum_{n=1}^N [t_{\text{heating}_n} + t_{\text{cool}_n}] \quad (1)$$

where $t_{\text{treatment}}$ is the total treatment time, t_{heating_n} is the heating time at position n and t_{cool_n} is the subsequent inter-pulse cooling time during which power is off before initiating the next heating pulse. In the current studies the normal tissue temperature constraint (see below) was never violated (except for a small subset of non-optimal runs), so inter-pulse cooling was never invoked, and thus the sum of the heating times always equalled the total treatment time. Additionally, a computational constraint that no individual heating pulse could be longer than 300 s was imposed on the solver for almost all treatments.

To ensure efficacy, a thermal dose constraint (which was a constraint function for the optimisation routine) ensured that all voxels in the tumour were treated to a minimum of CEM240 by the end of the treatment (a value commonly used in previous research [69, 70]), where CEM is the 'cumulative equivalent minutes' of dose at 43°C [39]. This included the dose accumulated during the cool down period following the last heating pulse of each treatment. To ensure safety, a strict temperature limit (which was an additional constraint function for the optimisation routine) was imposed in two normal tissue constraint planes located 1 cm proximal and distal to the tumour. That requirement was

$$\text{Max}(T_{NT}) \leq 6^\circ\text{C} \quad (2)$$

where $\text{Max}(T_{NT})$ is the maximum normal tissue temperature in the constraint planes. This temperature limit replicates the conservative temperature limit used in previous research [23, 25, 64] that triggers normal tissue cooling before significant dose is deposited in the normal tissue due to thermal build up. The location of the CEM30 dose surface in the tissue was also monitored and is reported for the cases where it is of interest (previous research has shown this to be an approximate limit above which irreversible tissue damage occurs [69, 70]).

Additionally, several computational tolerance constraints were imposed on the optimisation routine for the purpose of ensuring convergence. A tolerance for the evaluation of the objective function and each of the individual heating times (generally $<10^{-5}$ for both) was imposed on the solver for all simulations, and the simulations were terminated if this tolerance was met (i.e. the change of any value from one iteration to the next was less than the tolerance). Also, a maximum allowable number of 3000

iterations per optimisation was imposed on the solver, and the optimisation routine was halted if the maximum number of iterations was reached. In cases where the optimisation routine halted after the maximum number of steps without reaching a solution, a new starting guess for each treatment time (in the range (0, 300)) was input, and the solver was restarted until a feasible solution was found.

Pulse heating approaches

Two pulse heating approaches were used, concentrated and fractionated. There were N_{FZL} focal zone locations along the scan path in any given treatment, where N_{FZL} ranged from 1 to 25, depending on the tumour being treated. Each such location was heated N_{CYCLES} times.

Concentrated heating used a single pulse to heat each focal zone position to the desired thermal dose, and the focal zone did not return to heat any position a second time, i.e. $N_{\text{CYCLES}} = 1$ for this approach. The important independent variable for this approach is thus the pulse heating time at each location.

In fractionated heating, each focal zone position was heated with multiple shorter pulses as the focal zone cyclically scanned the N_{FZL} focal zone locations multiple ($N_{\text{CYCLES}} > 1$) times. Each fractionated pulse heating period was a fraction of the single pulse heating period, and delivered only a fraction of the desired thermal dose to that location. Important user-defined variables are the number of cycles used (N_{CYCLES}) and the time taken to execute the individual pulses within each cycle. For the fractionated heating approach two methods of implementation were investigated. First, since there are a total of $N_{\text{FZL}} \times N_{\text{CYCLES}}$ individual heating periods for each treatment, each of those times could be optimised, herein called the fully optimised, fractionated heating approach. Second, a simpler, more clinically practical version of fractionated heating involves the same fixed heating/dwell time at each location (equivalent to a constant scanning speed), with the cyclic scanning continuing until the complete tumour volume reaches the desired thermal dose, a fractionated heating approach previously characterised as 'volumetric' scanning [45, 49]. For high velocity volumetric scanning there is not enough time for the tissue to cool between cycles, and thus the high velocity fractionated heating approach becomes the equivalent of a single, large effective focal zone with the transducer's focal zone power diluted over the complete scanning volume. Conversely, as the scanning speed decreases the heating/dwell time at each position increases, the number of cycles needed to treat each position decreases, and the fractionated approach becomes closer and closer to the

concentrated approach, with $N_{\text{cycles}} = 1$ converging to the concentrated heating approach.

Optimisation techniques $t_{\text{heat}}: t_{\text{cool}}$

For a given treatment with all other treatment parameters fixed (e.g. scan path, number of focal zone locations heated) the optimal values for the individual heating times at each focal zone location were found using a gradient search routine. Two different optimisation techniques were used to determine those times: simultaneous, collective pulse optimisation, and sequential, single pulse optimisation.

Simultaneous, collective pulse optimisation was the primary technique used. It represents a 'best case' limit since it assumed, and utilised, complete, a priori knowledge of all of the thermal interactions among all heating pulses at all locations at all times during a treatment to find the set of pulse heating times that minimised the total treatment time. This technique minimised all heating times by reducing overdosing in the tumour by accounting for the SAR overlap and thermal conduction interactions among all pulses in a treatment. It worked by selecting initial guesses for the heating and cooling times at every focal zone heating location during the treatment, and then finding the optimal values of those times that minimised the total treatment time. This involved simultaneously optimising N_{pzt} heating times for the concentrated heating approach and $N_{\text{pzt}} \times N_{\text{cycles}}$ heating times for the fully optimised, fractionated heating approach. The *simulx* algorithm was run from several random guesses (i.e. in a Monte Carlo fashion) for starting times at each focal zone location to ensure convergence to a global minimum. Either the interior-point method or sequential quadratic programming method was used to generate iteratively updated times [71].

Since the simultaneous optimisation technique requires full a priori knowledge of the thermal effects of all treatment pulses, and such knowledge would be very difficult to realise clinically, it was important to determine whether its resulting treatment time gains would be worth the effort of trying to obtain that knowledge when compared to a more clinically practical technique. Thus, when concentrated heating was used, the collective pulse optimisation technique's treatment time predictions were compared to those of sequential, single pulse optimisation, which required very little a priori knowledge. That technique optimised each successive pulse's heating time individually, on a pulse-by-pulse basis. It used knowledge of the thermal history at each location arising from prior heatings, i.e. knowledge of the prior temperatures and thermal doses in the volume to be heated. The only future effect it

anticipated was the dose that would be delivered during that pulse's subsequent (post-heating) cooling period. Thus, in contrast to the simultaneous optimisation technique, the sequential optimisation technique did not anticipate/compensate for any dose delivered by future heating pulses.

Thermal simulations

All thermal simulations were done using a finite difference approximation to the spatial derivatives in the bio-heat equation [72]:

$$\rho C \frac{\partial T}{\partial t} = k \nabla^2 T - WC_b(T - T_b) + Q_{\text{ext}} \quad (3)$$

that converts the Pennes equation into a set of simultaneous ordinary differential equations that were solved using the Matlab[™] function ODE45, which uses a Runge Kutta approach. Here, T is the temperature ($^{\circ}\text{C}$) at the point being analysed, ρ is the tissue density (kg/m^3), C is the specific heat of tissue ($\text{J}/\text{kg}^{\circ}\text{C}$), k is the thermal conductivity of the tissue ($\text{W}/\text{m}^{\circ}\text{C}$), Q_{ext} is the applied power density deposited by the external applicator (W/m^2), W is the Pennes perfusion parameter ($\text{kg}/\text{m}^3/\text{s}$), C_b is the specific heat of blood and T_b is the arterial blood temperature. All simulations used a 1-mm isotropic spatial grid and a time step of 0.1 s or less. Thermal dose values were calculated using the approach of Sapareto and Dewey [39] using a 1-s time step.

Power deposition

The power deposition distribution was determined as in previous research [23, 25] using the hybrid angular spectrum (HAS) method [73] to simulate a 256-element phased array (Imasonic, Paris, France) with a diameter of 14.5 cm, a geometric focus of 13 cm, and a central frequency of 1 MHz. Resolution of the ultrasound field was 1 mm isotropic. The transducer (which was used in the associated phantom experiments (see below) was simulated to produce the smallest possible focal zone consistent with the diffraction limit, yielding a full width at half maximum (FWHM) focal zone specific absorption rate (SAR) volume of $1 \times 1 \times 12 \text{ mm}^3$. The total power from the transducer was set at a fixed value for all treatments (with a few exceptions as noted). The maximum power density used occurred when the focal zone was centred at the back face of the larger ($1 \times 1 \times 30 \text{ mm}^3$) axial tumour, and was $0.6 \times 10^3 \text{ W}/\text{m}^3$. The associated fixed transducer power magnitude was used in all studies since it has been shown in previous studies [23, 25] that a 'knee' occurs near this power density, below which the treatment times become significantly longer, and above which only minimal time gains are possible. This peak power density was similar to that used in

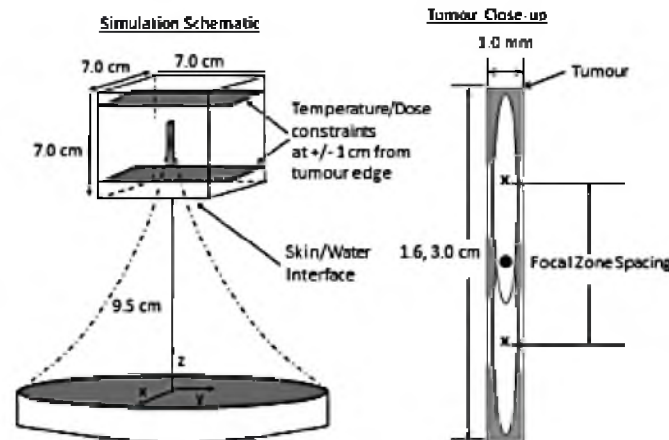


Figure 1. Model used for axial focal zone spacing and packing optimisation studies. The simulation region (left) and a close-up (right) of an 'axial tumour' are shown. The black dot at the centre of the tumour (right) marks the location of both the centre of the tumour and the geometric focus of the transducer. Both axial tumours (1.6 and 3.0 cm long) had at least 2.0 cm (slightly more for the smaller tumour) of normal tissue between the skin/water interface and the proximal tumour face to allow for a significant space in which normal tissue heating could occur.

previous work [23, 25] and well below limits set by the US Food and Drug Administration (FDA) [74]. The beam was steered electronically along the z-axis (which has been reported to increase near-field heating [75]) for all simulations, and mechanically (simulating the use of piezoelectric motors) for the transverse scans except for the 25-position simulations matched to phantom data, which used electronic steering.

Simulation region

Treatments were simulated in a $7 \times 7 \times 7 \text{ cm}^3$ treatment region, with the exception of the phantom experiment simulations which used a $10 \times 10 \times 10 \text{ cm}^3$ region. The geometric focus of the transducer and the centre of the simulated tumours coincided at 13 cm from the transducer face for all simulations. The simulation geometry is shown in Figure 1 along with a magnification of the 'axial tumours' used for the axial focal zone spacing and packing density optimisation studies. The acoustic and thermal properties of the $7 \times 7 \times 7 \text{ mm}^3$ region are listed in Table 1. The $10 \times 10 \times 10 \text{ mm}^3$ phantom matching studies had an iteratively calculated conduction coefficient of $0.4 \text{ (W/m}^2 \text{ } ^\circ\text{C)}$, zero perfusion, and a transducer power that was a factor of three larger than in the other simulations (to match the experiments). All other property values were identical to those in Table 1.

Tumours and scan paths studied

Three types of generic tumours that increased in complexity/extent were studied, each with associated scan paths chosen to study particular optimisation problems: tumours treated by an axial stack of focal zone locations; pairs of adjacent axial stacks to investigate transverse thermal effects, and 25-position transverse scans for which phantom experiments had been performed. All three tumour types were used to compare the two pulse heating approaches and the two optimisation techniques. The need to proceed sequentially in complexity/extent was motivated by the large scale of the problem being solved as noted in the introduction. That is, with over 300 000 finite difference points (1 000 000 in the case of the 10-cm^3 region) being modelled over long time periods with small time steps, and with each possible treatment scenario being simulated many times over in the iterative optimisation process, the computational times involved were very large, with over 250 000 h of parallelised computer time being used for the simulations in this study.

Axial tumours

Previous research [25] has shown that a series of axially stacked focal zones that are sequentially applied to a 3D tumour yields the fastest treatments, and that while there were some additional gains attained by optimising stack adjacency, each axial

Table I. Tissue and acoustic properties held constant in all simulations except for the changing absorptivity study.

Thermal conductivity, k ($\text{W}/\text{m}^\circ\text{C}$)	0.5
Specific heat, C ($\text{J}/\text{kg}^\circ\text{C}$)	4190 (blood & tissue)
Speed of sound, c (m/s)	1500 (tissue & water)
Absorptivity coefficient, α ($\text{Np}/\text{m}/\text{MHz}$)	5.0 (values of 1.0, 1.5, 2.0 also used for the absorptivity study)
Density, ρ (kg/m^3)	1000
Femmes' perfusion, W ($\text{kg}/\text{m}^3/\text{s}$)	0.5 (a value of 5.0 was also used in the axial spacing study)

stack was relatively independent of other stacks for most cases. Thus, studying single stacks was a good place to start since it provided useful insights into the main characteristics of the basic physics of the scanning process. Those insights were then useful when studying more complicated problems. Two simple, axial tumours were studied, a $1 \times 1 \times 16 \text{ mm}^3$ (smaller axial tumour) and a $1 \times 1 \times 30 \text{ mm}^3$ (larger axial tumour). These tumours were used to investigate the effects of optimal spacing, axial focal zone packing (in which the number of focal zone locations used to treat a tumour ranged from 1–17) and scan path order (see Figure 2). The axial tumours were also used to study the effects of increased tissue absorptivity following heating.

Adjacent focal zone stacks

To expand to cases with more focal zones and spatial dimensions, larger tumour regions heated by two adjacent stacks were used to optimise the transverse spacing for both pulse heating approaches. Two adjacent axial stacks, each with two axial focal zone positions, were modelled (see Figure 3). The axial spacing between focal zones in each stack was fixed at the optimal value found in the axial tumour study. The transverse distance between the axial stacks' centre lines was varied from 1 to 6 mm in 1-mm steps.

Planar scanning of a larger tumour

Finally, simulation studies were performed that replicated the experimental conditions used to heat a phantom with 25 focal zone positions in a plane perpendicular to the transducer's axis [76]. Replication allowed the power levels used in the simulations to be made equivalent to those used experimentally, the thermal conductivity of the phantom to be estimated, and the simulation process to be validated [76]. Experimentally, the focal zone was electronically scanned with the 25 focal zone positions arranged in either concentric circles or a square raster pattern at a constant depth in the tissue. The simulated treatment was then iteratively matched to the experimental data by comparing the 240 and CEM30 dose lines of the two treatments

through a least-squares fit in three orthogonal planes containing the focal zone's peak power density. The circular scans had a central point plus two concentric circles with radii of 2.25 and 4.5 mm, and 8 and 16 focal zone locations, respectively. The focal points were evenly spaced on the circles, which were scanned in an 'in-to-out' pattern with the central point heated first. The square tumour's dimensions were $10 \times 10 \text{ mm}$ with a 2-mm transverse separation of focal zones, and it was scanned in a 5×5 position raster scan pattern starting in one corner. The experimental and simulated concentrated heating approach used fixed heating pulse times of 15 s at each of the 25 locations yielding a heating time of 375 s. In the fractionated heating approach, each point was repeatedly heated 150 times for 0.1 s during each heating, yielding the same total heating time as the concentrated approach. Having equivalent total heating times and applied power levels for both the fractionated and concentrated scans allowed a comparison of their ablation rates by determining which technique first reached the desired dose everywhere in the matched treatment planes. In these (non-optimised) experiments the concentrated heating approach had higher ablation rates than fractionated heating for both the circular and square patterns. This was also true in the associated, matched treatment simulations, which gave results that were very close to those of the experiments [76]. Having performed this initial verification test for the simulations, further simulation studies were performed with the validated model to investigate additional treatment scenarios.

Model of absorptivity changes

To examine the effects of absorptivity changes, a 'worst-case' scenario approach was studied for the three-position axial tumour. The smaller axial tumour was divided into three equal sub-volumes, each to be treated by a focal zone position centred on that sub-volume. Absorptivity was either doubled or quadrupled from its initial value at every position in each sub-volume immediately after it had been treated, and before the next position in the treatment path was heated. The same absorptivity increase was

made at all points in the sub-volume, regardless of the dose they had received (all of which reached at least CEM240 by the end of the treatment). This model of absorptivity change is much faster (i.e. instantaneous) and much larger than measured in *ex vivo* dog tissue heated in a water bath [59], which reached a maximum absorptivity of only twice the baseline value. These studies were performed using the concentrated heating approach and the collective optimisation technique.

Results

Results are presented in order of evolving complexity/extent starting with the axial tumour model and ending with the 25-position phantom treatment simulations. For all cases the desired minimum thermal dose, or a higher dose, was delivered to all tumour locations. Results are presented in terms of the total heating times since for all cases of interest the total cooling time was zero. All results are for a constant perfusion of $W = 0.5$ (kg/m³/s) and a middle/front/back scan path, which is the axial focal zone sequence previously shown to give the shortest heating times [25], unless otherwise indicated.

Axial spacing and packing optimisation

Optimal spacing and packing studies were performed for heating tumours with one, two, three, four or 17 axial focal zone locations. These studies were also used to investigate the effects of heating approach (concentrated and fractionated), optimisation technique (collective and sequential) and focal zone size.

One focal zone position

The simplest case used one focal zone position to heat the small axial tumour, with a search done in 1-mm steps to find the optimal offset of the focal zone position from the centre of the tumour. The offset that produced the shortest treatment times was with the focal zone centred at the tumour centre (zero offset) or slightly distal to it, with the difference in heating times between the two locations being less than 5 s. The resulting treatment time for the central location is shown in Figure 4a (where this single pulse case is equivalent to zero separation of two focal zones). As expected, using only one position of this small focal zone to heat this tumour resulted in long treatments (the focal zone's FWHM axial length is 12 mm, which only covered three quarters of the tumour's length).

Two focal zone positions

Figure 4a shows the optimised treatment times for treating the smaller axial tumour versus the axial

separation of the two focal zones for the collectively optimised, concentrated scanning approach (circles) and the fractionated heating approach (diamonds), for which high velocity scanning was simulated. The percentage of the optimised time spent in the front/back positions is shown for the concentrated case, and the corresponding duty cycle percentages are shown for the high velocity, fractionated scanning approach. For the high velocity scanning approach, optimising the duty cycle is equivalent to optimising a large, effective focal zone's shape. These results show firstly that when both heating approaches were optimised for both focal zone spacing and for front/back heating times, the concentrated heating approach gave shorter treatment times than the high velocity, fractionated heating approach.

Secondly, also shown in Figure 4a (by the \times) is the total treatment time for the fully optimised, fractionated heating approach case with two cycles treating the two positions ($N_{\text{FZL}} \times N_{\text{CYCLES}} = 4$) at the 8-mm spacing. This result shows that when complete freedom was given to the four individual heating times of the fractionated approach, that approach reduced to the concentrated heating approach – that is, its four times reduced to twice identical to the two (front/back) optimal concentrated heating approach times, plus two zero heating times.

Thirdly, for the concentrated heating approach the optimal spacing corresponds to both an overlap of the two focal zones' FWHM lengths of 2 mm for each focal zone (17% of the axial FWHM), which prevents a thermal dose 'hole' in the centre of the tumour, and an extension of the FWHM SAR to 2 mm beyond the tumour's front and back boundaries. This distribution heats the ends of the tumour, which generally require more energy deposition [25], without spacing the focal zones too far apart. Also as expected, the optimal spacing smoothed out the thermal dose within the tumour. Figure 4b shows the dose distribution in the tumour for the 2 mm, 8 mm and 16 mm spacings.

Fourthly, the results show that the time gains obtained by the more practical, sequential optimisation technique applied to the concentrated heating approach (square symbol) were quite similar to those from the difficult to implement, complete knowledge, collective optimisation strategy that assumed full a priori knowledge of all treatment information.

Finally, studies with the perfusion value increased to 5 kg/m³/s were also performed using both the concentrated and high velocity fractionated approaches at all the focal zone spacings shown in Figure 4a. The results of those studies show that while, as expected, the treatment times were increased versus a lower perfusion, the value of the optimal focal zone spacing and the general 'U' shape

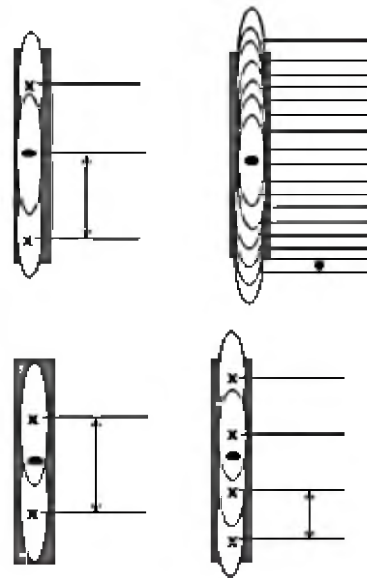


Figure 2. Schematic of treatments on the axial tumour using two, three, four and 17 positions. The black dot at the centre shows the tumour centre and the location of the geometric focus of the transducer. The arrows show the distances used to define the focal zone spacing for every treatment. All focal zones were equally spaced within any given treatment.

of the graph were unchanged at the higher perfusion values.

Three focal zone positions

Figure 5 shows the treatment time versus the distance of the proximal and distal focal zone centres from the tumour centre (where the middle focal zone is centred) for the smaller axial tumour. Results are shown for the concentrated heating approach using the collective optimisation technique (open circles) at all spacings, and for the sequential optimisation technique (closed squares) at selected spacings. Also shown at the optimal spacing (6 mm) are 1) the optimised treatment time for the fully optimised, fractionated heating approach for two cycles, for which the six optimised pulse heating times were found to be the same three times as for the collectively optimised concentrated heating approach plus three zero pulse heating times (\times), so that the fully optimised fractionated approach became equivalent to the concentrated heating approach, and 2)

the optimal heating time for the collectively optimised, high velocity fractionated scan (diamond).

To further investigate the details of the three-position high velocity fractionated heating approach with collective optimisation, the treatment times for all possible duty cycles (in steps of 10%) using three positions were studied with the optimal 6-mm spacing. The results (Figure 6) show that optimising the duty cycles (which, at high scan velocities is equivalent to optimally shaping a fixed, effective focal zone) gives a minimum heating time of 114 s for the optimal distribution (20/30/50% for the middle/front/back focal zones respectively). This time can be compared to the more clinically practical fractionated approach of a fixed heating time at each focal zone location (i.e. a uniform duty cycle of 33/33/33%) which has a total treatment heating time of 168 s, which shows that spatially optimising (shaping) a focal zone of fixed size can yield significant treatment time gains. However, the total heating times for both of those fractionated approaches are still much longer than the concentrated heating approaches' times for both collective optimisation (63 s, Figure 5) and sequential optimisation (64 s, Figure 5).

Focal zone packing

Since the above results showed that increasing the number of focal zones used to heat a given tumour yielded faster treatments, additional optimisation studies were performed with more positions and for treatments of the larger axial tumour, resulting in studies of one, two, three and 17, and three, four and 17 positions for the smaller and larger axial tumours, respectively. The resulting treatment times are shown in Figure 7 for collective optimisation of both the concentrated heating approach and the high velocity fractionated heating approach. The focal zones' spacings and duty cycles for these treatments were optimised as described below. Due to the fact that the concentrated treatments had shorter treatment times than the high velocity treatments for every treatment configuration examined so far, concentrated treatments were examined in more depth, while still continuing to study a smaller set of fractionated treatments.

Concentrated heating approach: The treatment times shown in Figure 7 for the two- and three-position treatments of the smaller axial tumour using full optimisation and concentrated scanning are taken from Figures 4 and 5 respectively. These points represent the fastest treatment times found in each of those figures. The treatment time in Figure 7 for the four-position treatment of the smaller axial tumour was obtained as part of a larger study. In that study a complete range of uniform spacings between focal

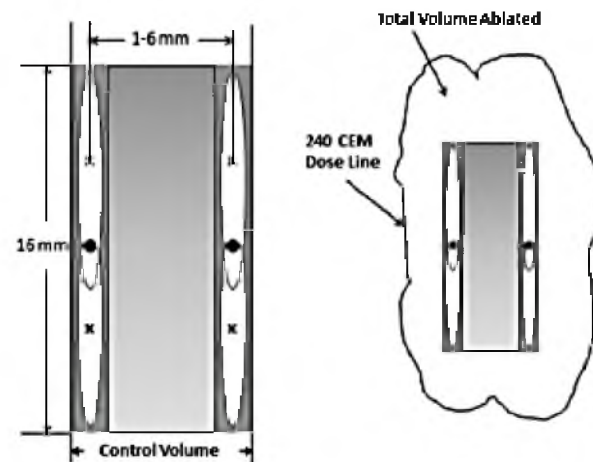


Figure 3. Schematic of the four-position transverse spacing study using two axial stacks of two positions each. The black dot at the centre of each axial stack of focal zones coincides with the geometric centre of the transducer. The axial spacing between focal zones in each stack was fixed at the optimal value found for the two-position treatment of a single axial stack. The shaded area between the stacks shows the inter-axial tumour volume (left) where the dose is guaranteed to reach the target dose (CEM240) by the end of the treatment. This 'control volume' is smaller than the 'total volume ablated' by the treatment (right) because thermal dose is also deposited exterior to the inter-axial tumour space.

zones was simulated. Those spacings (Figure 2) began at 1 mm and increased to a limit where the most proximal/distal focal zones' centres were touching the edges of the tumour. The four heating times were optimised at each such spacing. The fastest treatment time for the optimal spacing is shown in Figure 7. That optimal spacing was 7 mm, resulting in focal zones with centres at 4 mm, 11 mm, 18 mm, and 25 mm from the front face of the tumour.

To study an even denser focal zone packing, treatments with 17 locations were studied with those locations uniformly spaced 1 mm and 2 mm apart for the smaller and larger tumours, respectively. The heating times were optimised at all 17 positions for both tumours using the collective optimisation technique. The results in Figure 7 are shown for the middle/front/back path, which was the fastest path. (Also studied with the collective optimisation approach were a front/middle/back path and a back/middle/front path for the small axial tumour, both of which had treatment times that were a few seconds longer than the middle/front/back path.) The small tumour was also treated with the concentrated heating approach using sequential optimisation and the resulting minimised treatment time was essentially the same as for the collective optimisation technique.

High velocity fractionated heating approach: The data points in Figure 7 for the two- and three-position treatments of the smaller axial tumour are the fastest treatment times for high velocity scans from Figures 4 and 6 respectively. Studies were also performed for the larger axial tumour using high velocity scanning for two, three and four positions. The duty cycles that minimised the treatment times were iteratively optimised for each of those three treatments. In that optimisation a search was conducted that minimised the treatment time for a given duty cycle, and then a new duty cycle was generated via a heuristic algorithm that moved heating time away from overdosed focal zone locations to focal zone locations with minimal dosing. Also, treatments of the larger tumour were performed for three, four and 17 focal zones with a more clinically practical uniform duty cycle at all positions (with a two-position treatment not attempted because of insufficient coverage of the tumour, which would lead to long heating times). In the three-, four-, and 17-position uniform duty cycle cases the treatment times were also quite long, being 525, 602, and 625 s respectively. The treatment times for the uniform duty cycle treatments increase monotonically with the number of positions because the increased number of positions further dilutes the power from the treatments with fewer positions. However, a

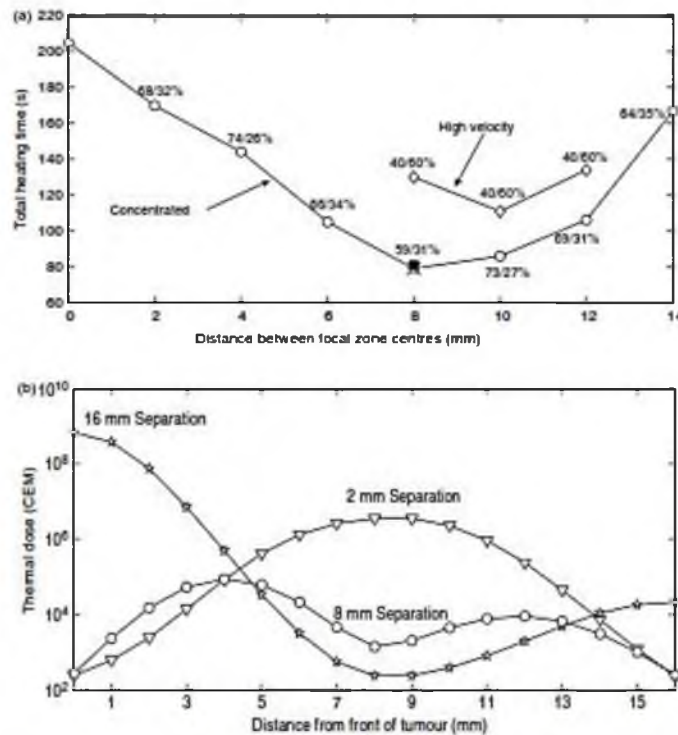


Figure 4. (a) Total heating time versus axial separation of the centres of two focal zones ($N_{FZL} = 2$) heating the smaller axial tumour using a front-back scan path with the focal zones located symmetrically around the tumour centre. Zero separation indicates complete overlap of the two focal zones (i.e. it is equivalent to using only one focal zone). Results are shown using collective optimisation for both the concentrated heating approach (circles) and the high velocity fractionated heating approach (diamonds). The percentage of the optimised times spent in the front/back locations are shown for all separations. Also shown (at 8 mm) are the total heating times (x) for a fully optimised, fractionated scan for $N_{CYCLES} = 2$ in which four times were optimised, and for a concentrated scan using sequential optimisation (solid square) whose optimised front/back heating times were similar to the fully optimised times. (b) Thermal dose versus distance from the front of the tumour for the treatments of the small axial tumour using 2 mm (diamonds), 8 mm (squares), and 16 mm (stars) separations with the concentrated heating approach and collective optimisation.

point is eventually reached where the power cannot be diluted further because it is distributed as uniformly as possible (given the dimensions and shape of the focal zone) throughout the treatment region, which is why the treatment times are seen to plateau between four and 17 positions.

To illustrate how the collectively optimised pulse heating times vary with position for concentrated heating, Figure 8a shows the heating times as a function of distance from the proximal tumour face using 17 positions to heat the smaller axial tumour. Figure 8b shows a similar graph for the sequentially optimised concentrated heating approach case.

The general shapes of these curves were the same for the larger tumour.

Optimal transverse spacing

To investigate a scan path with both axial and transverse components, a study of two adjacent axial stacks was performed, with each stack having two axial heating locations (Figure 3). Both stacks used the optimal axial spacing for the high velocity fractionated treatments from the two-position study (10 mm, Figure 4a) – a spacing that slightly favoured the fractionated heating approach. Results are shown in Figure 9a for the ablation rate of the internal

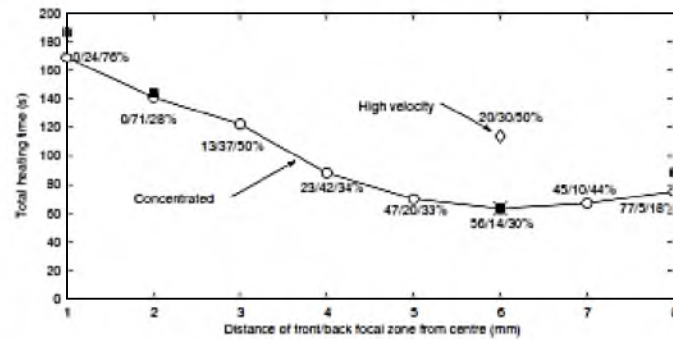


Figure 5. Treatment time versus distance of the proximal and distal focal zones from the tumour centre in a three-position, middle/front-back treatment of the smaller axial tumour for the concentrated heating approach using the collective (open circles) and sequential (solid squares) optimisation techniques. The percentage of time spent in the middle/front/back focal zone locations is shown for the collective optimisation technique. Also shown at the optimal spacing are the result for the fully optimised fractionated heating approach (\times) with two cycles ($N_{\text{cycles}} = 2$, for which six times were optimised) and for the high velocity, collectively optimised fractionated scan (diamond), i.e. the single, larger effective focal zone case.

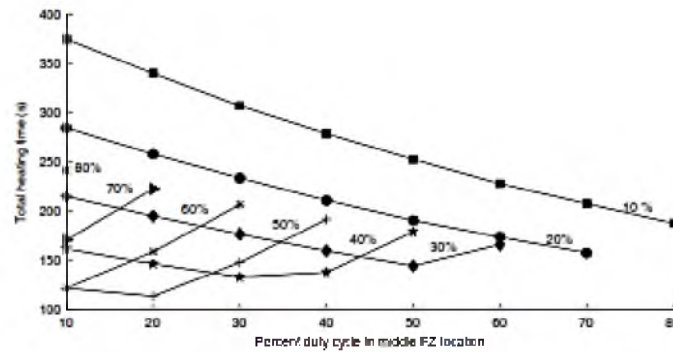


Figure 6. Treatment time versus middle position duty cycle for a high velocity, three-position treatment of the small axial tumour using the optimal spacing of Figure 5. The duty cycle percentage spent at the back focal zone position is shown above each line, while the front position percentages can be obtained by subtraction.

tumour volume (the two axial stacks' voxels plus all voxels between the two stacks) versus transverse spacing for both the collectively optimised concentrated heating approach and the high velocity, fractionated approach at a uniform, 25% duty cycle. The four positions of the optimal heating times of the concentrated approach are shown as the percentage of the total treatment time at each spacing. The 23 other possible paths for the four-position treatments were also investigated for the concentrated heating approach with collective optimisation, and the total treatment times were found to

be relatively insensitive to permutations in scan path order.

At the optimal transverse spacing (3 mm) of the concentrated approach, this graph also shows the treatment time needed for the fully optimised, fractionated heating approach for two cycles, which requires optimising eight pulse heating times. Again, as in the two- and three-position axial studies, the fully optimised fractionated case resulted in optimal pulse heating times that were the same as the times of the collectively optimised concentrated approach (i.e. $N_{\text{cycles}} = 1$ with the four concentrated approach heating times plus four zero heating times). Finally,

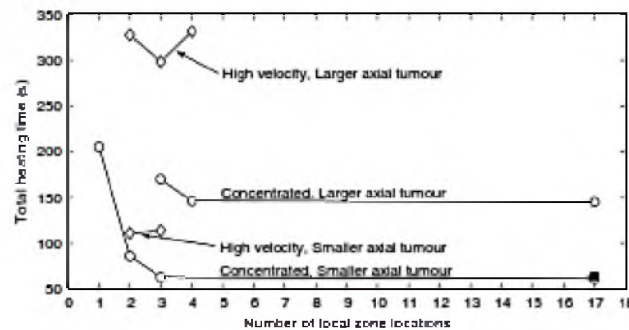


Figure 7. Treatment time versus the number of focal zone locations for concentrated heating using the collective optimisation technique (circles) and for the high velocity, fractionated approach that creates a single, large effective focal zone (diamonds). Results are shown for both the smaller and larger axial tumours. Results are also shown for the 17-position case for the concentrated treatment of the smaller axial tumour using sequential optimisation (filled square).

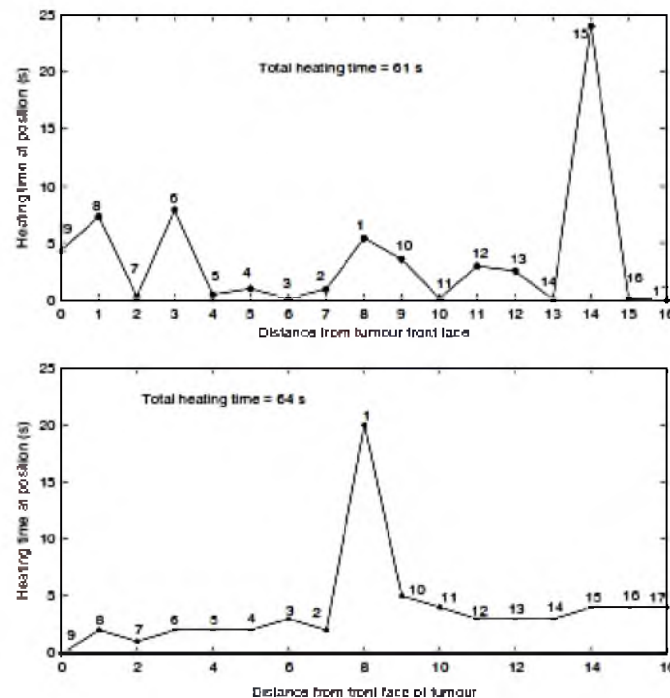


Figure 8. Heating time at each position versus distance from the front tumour face for the 17-position treatment of the smaller axial tumour using a middle-front-to-back treatment path and the concentrated heating approach. Results are shown for both the collectively optimised (top) and sequentially optimised (bottom) techniques. The number by each data point indicates the relative order in which that focal zone location was heated.

at that optimal 3-mm spacing the total treatment time is also shown for the sequentially optimised concentrated approach, with the times spent at each focal zone location noted (as a percentage of the total treatment time).

Figures 9b and 9c show the final dose contours in the plane containing the two stacks' axes for the collectively optimised, concentrated (Figure 9b) and high velocity, fractionated (Figure 9c) cases of Figure 9a. For the fastest collectively optimised, concentrated scan spacing (at 3 mm) the CEM30 contour line remains within the required 10 mm proximal and distal normal tissue constraint boundaries, so that heating approach does not violate the normal tissue constraint either for the lenient normal tissue constraint of a CEM30 dose or for the much stricter 6°C temperature constraint. However, for larger spacings, not only do those scans have lower ablation rates, but they also violate both the dose and temperature constraints. By comparison, the collectively optimised high velocity fractionated case violates the CEM30 dose and 6°C temperature constraints even for the 3-mm spacing. Activating constraints would, clinically, require additional cooling times, thus further lengthening treatments and lowering the ablation rate.

Finally, Figure 9d shows the results for the same scans as Figure 9a, but the ablation rate now includes the tissue volume exterior to the axial stacks which was treated above CEM240. Since no fixed volume was being heated to CEM240, in order to fairly compare different cases it was necessary for comparison to have a different standard than treatment time. To do so, the results in Figure 9d are given in terms of the ablation rate present at the time at which the control volume was treated to CEM240 by the concentrated heating approach in Figure 9a. This allows fair comparisons of the two approaches by using the same heating time for both approaches, and then comparing ablation rates at that time. Also shown are the spacings at which each of the approaches first violates the normal tissue constraint for temperature and dose. This violation continued for all treatments to the right of these lines.

Twenty-five-position transverse scans

To further investigate the effects of heating approach and optimisation technique, several cases were run using the 25-position model which was calibrated against the phantom experiments [76]. Three concentrated and three fractionated approach treatments were evaluated for the square tumour.

In the first simulation study of the concentrated approach the heating time was the same for all focal zone locations (as in the experiments), but now that uniform heating time was systematically lowered

(until a minimal focal zone heating time was found that treated the complete tumour (9.4 s per location, 236 s total time)). A second concentrated approach simulation used the collective, simultaneous optimisation technique, yielding a set of 25 optimised focal zone heating times, giving an average heating time per location of 8.5 s (213 s total time). A third concentrated approach treatment used the sequential optimisation technique. It had a total treatment time of 219 s.

Three fractionated heating approach cases were simulated that varied the scanning speed (and the related number of traverses through the tumour, N_{cycles}) using the uniform heating time approach. The heating time per position was set to either a very rapid switching time between scanning path trajectory points (i.e. fast fractionated heating which created a large, effective focal zone), or 0.1 s, or 1.0 s per position. The treatment time for the large, effective focal zone case was optimised by finding the smallest heating time that treated every voxel of the tumour to at least CEM240. For the treatments using a 0.1 or 1.0 s heating time per position, the number of passes through the trajectory (N_{cycles}) was set an initially high value and was sequentially reduced until a minimum number was found that would still treat the entire tumour to CEM240 (114 and 11 cycles, respectively) with no partial passes through the scanning path trajectory.

Absorptivity property changes

To investigate the effects of increases in tissue absorptivity due to heating of tissue, a study was performed using the small axial tumour and a three-position treatment with the collectively optimised, concentrated heating approach. The optimisation technique took into account the future changes in attenuation due to heating. The absorptivity was either doubled or quadrupled (from an initial value of 5 Np/m at 1 MHz) immediately after each position (and its sub-volume) was heated. Figure 11 shows the resulting treatment times for the four axial treatment paths investigated. All treatments were run from at least 12 randomly selected starting points to check for the presence of local minima. In each case, local minima were found and the lowest treatment time found is shown. A 6°C temperature rise constraint was used in the normal tissue, but was not activated by any of the treatments.

Discussion

Four important conclusions can be drawn from these results. First, all focal zone heating approaches can be considered as lying along a spectrum with the number of cyclic heating passes (N_{cycles}) through

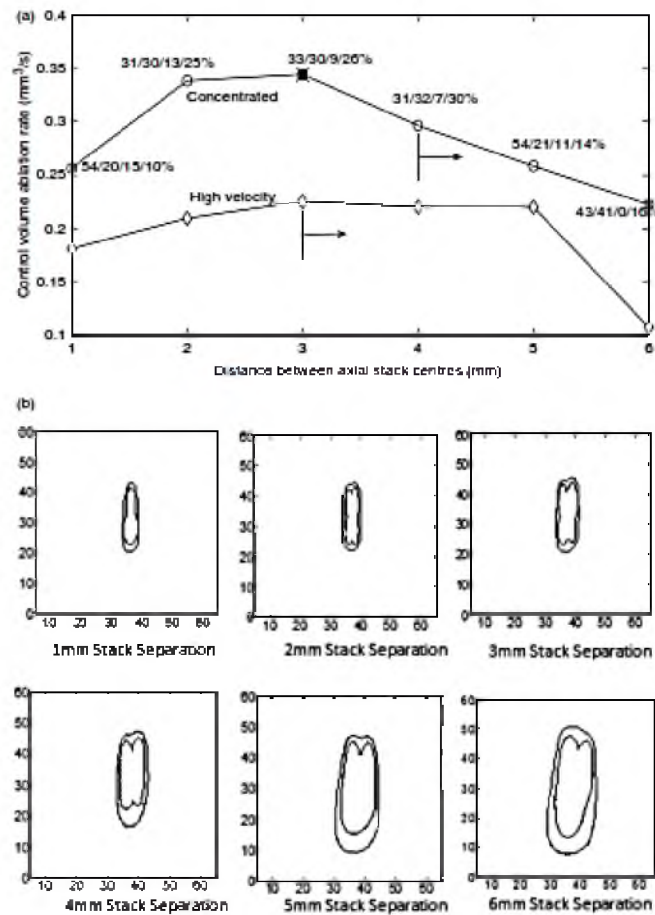


Figure 9. (a) Ablation rate in the control volume (the voxels in the control volume as defined in Figure 3) versus centreline separation for two side-by-side, two-position axial stacks for the collectively optimised, concentrated heating approach (open circles) and the optimised high velocity fractionated heating approach with a uniform duty cycle of 25% at each position (diamonds). The percentage of time spent at each of the four positions (front/back for stack 1 then front/back for stack 2) is shown for the concentrated heating approach. The axial spacing between focal zones in each axial stack was 10 mm. The cross (x) at 3 mm shows the result for the fully optimised, fractionated case with two cycles (and hence eight pulse heating times) which reduced to the concentrated heating times plus four zero heating times. Also shown is the result for the sequential optimisation of the concentrated heating approach as the optimal spacing (filled square). The vertical lines indicate the spacing at which each treatment approach first violated the normal tissue constraints, with the arrow indicating that all larger spacings also violated the safety constraint. (b and c) Dose maps of treatments using two adjacent axial stacks (of two positions each) for spacings between the centres of the two stacks of 1–6 mm for the collectively optimised, concentrated focal zones (b) and the high velocity fractionated heating (c). The interior and exterior dose lines for each map are the 240 and 30 CEM lines respectively. The slice contains the two stacks' axes. Dimensions are in mm. (d) The ablation rate for the total volume (control volume + exterior voxels) treated using two axial stacks with four positions each with all parameters identical to those listed in Figure 9A for treatments using concentrated heating (open circles) and high velocity fractionated (closed circles) heating. The spacings where the normal tissue and dose constraint are first violated are indicated by arrows.

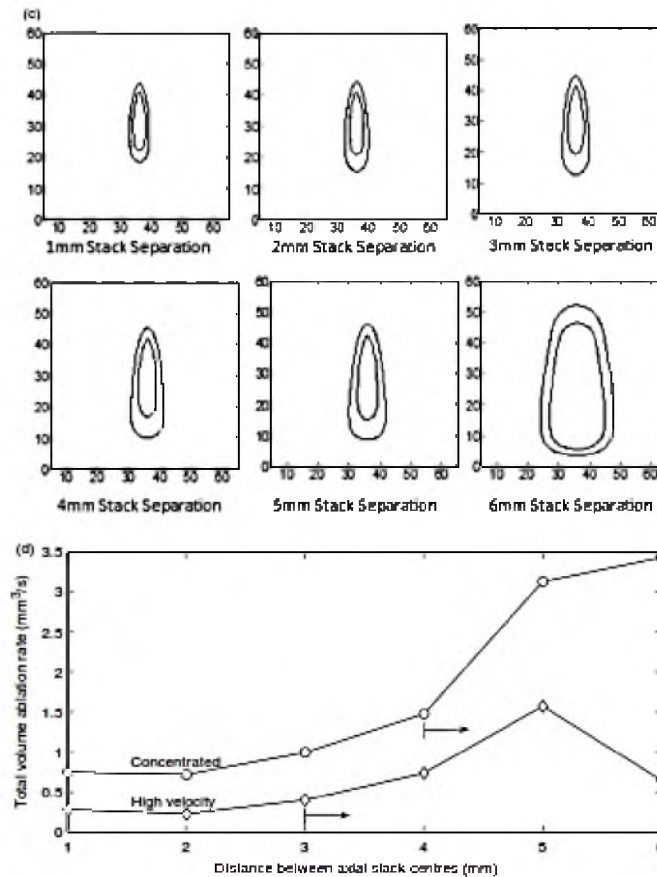


Figure 9. Continued.

the tumours' N_{pzt} heating positions as an independent variable. At one end of the spectrum is the optimised concentrated heating approach ($N_{\text{cycles}} = 1$) which always gives the shortest treatment times, while at the other end is the optimised high velocity fractionated scanning (with $N_{\text{cycles}} \gg 1$) which gives the longest treatment times. As the scanning speed of the fractionated heating approach increases (i.e. the dwell time per position decreases and the number of cycles increases), the high velocity fractionated heating approach becomes the equivalent of a single large effective focal zone and it has the longest treatment times. Second, for a given number of focal zone locations used to treat a tumour, both

heating approaches have optimal axial and transverse spacings that, when used, can significantly reduce treatment times. For the concentrated heating approach the treatment time decreases monotonically with the number of heating positions, but a point of diminishing returns is reached at a relatively low focal zone packing density. Third, the sequential, pulse by pulse optimisation technique gives almost the same treatment time gains as the much more difficult to implement complete knowledge, simultaneous pulse optimisation technique. Finally, large, rapid changes in tissue absorptivity (i.e. immediately increasing by a factor of four) can affect the optimal choice of scan path, but whether such large, rapid

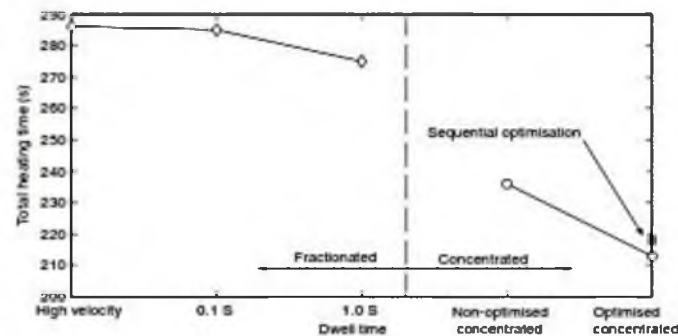


Figure 10. Heating time versus scanning approach for six different treatments on a square treatment region with transducer and tissue parameters matched to data from an agar phantom. The diamonds show the results of the fractionated heating approach with different fixed heating times per pulse. The circles show the concentrated approach results for a fixed (non-optimised) heating time per pulse and a collectively optimised scan, while the solid square shows the sequential optimisation result.

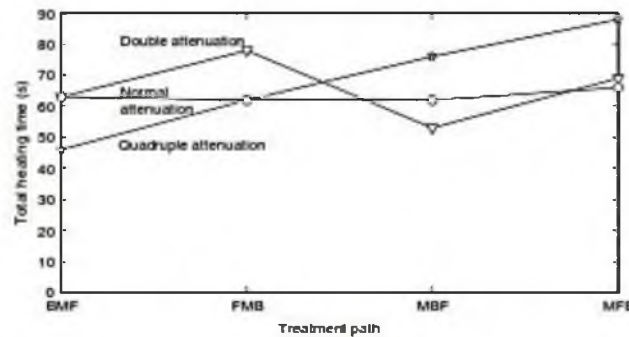


Figure 11. Collectively optimised concentrated heating approach heating times versus treatment path sequence for the smaller axial tumour using three positions with normal absorptivity (circles) immediately doubled absorptivity (triangles) and immediately quadrupled absorptivity (stars). Spacing between focal zones is the optimal value found in the three-position axial spacing study. The abbreviations F, M, and B are used for the front, middle, and back treatment focal zone locations, respectively, and the order in which the letters appear is the order in which the focal zones were heated.

changes will actually occur during treatments remains to be seen.

First, all cases studied showed that using concentrated heating pulses reduced treatment times when compared to the fractionated ('volumetric scanning') heating approach. This is illustrated by two consistent trends. First, the collectively optimised concentrated heating approach always had the shorter heating times, and second, the fractionated approach always reduced to the concentrated approach when it was 'fully optimised', i.e. when each of its $N_{\text{cycle}} \times N_{\text{FZL}}$ heating pulses could be independently optimised. The fractionated approach

has longer heating times since after it heats one position it then moves away, allowing that position to cool, thus requiring later reheating (and more time). Trying to rapidly switch the focal zone between several points to create a large, effective focal zone to avoid such cooling makes treatments even slower because the single focal zone's concentrated power is then diluted over a wider volume, causing the temperatures to rise more slowly everywhere. This approach thus both takes longer to reach high temperatures where the non-linear thermal dose effects occur, and allows more time for thermal losses by conduction and blood flow. Because long

treatment times are likely to be a major barrier to practical clinical implementation of HIFU treatments, the results of this study suggest, from the treatment time viewpoint, that implementing concentrated, rather than fractionated, heating would be advantageous. That is, while other considerations might make volumetric scanning clinically attractive, reducing treatment time is clearly not one of them. This conclusion is reinforced by the current results which show that the fractionated heating approach is also associated with more normal tissue heating than is present in a comparable concentrated heating approach. Thus, in larger, more complicated tumour treatments the fractionated approach would likely also require even more tissue cooling than the concentrated approach, resulting in even larger differences in total treatment time between the two heating approaches.

Also, although they are always slower than the comparable concentrated scans, the treatment times for high velocity fractionated scans are decreased greatly when the duty cycle and focal zone spacing are optimised – when compared to the more typical, and practical, approach of using a uniform duty cycle and a conservative spacing. The optimised shapes of the effective focal zones created in this study by high velocity fractionated scans roughly mimic the ‘volcano’ shape found to be optimal in previous research [51] with a simple effective focal zone power deposition model.

Second, when using the concentrated heating approach it is clear that increasing the number of focal zone locations used to treat a given tumour monotonically decreases the heating time needed. The mechanism for this treatment time reduction is that heating more locations along a given focal zone trajectory makes it easier to both avoid low dose, ‘untreated holes’ in the tumour, and also to reduce the amount of overdosing at all locations. However, the treatment time gains so obtained seem to reach a point of diminishing returns at quite low focal zone packing densities. In the limit ($N_{fz} \rightarrow \infty$), this method can be considered as a continuously scanning method with an optimised velocity distribution. However, the results from the 17-position study indicate that extrapolating out to large numbers of positions by such scanning will likely yield only minimal additional time gains compared to simpler treatments with a smaller number of focal zone locations, e.g. $N_{fz} = 4$ in the current simple generic tumour model heated by this transducer. Finally, the concentrated approach may be optimised even further by reducing the current requirement that each FZ heating location be associated with dosing the focal zone’s complete FWHM volume. That is, requiring it to dose a smaller volume (with one MR voxel centred in the FZ being the limit) would give

more ability to optimally shape the dose contours by utilising controlled heating at even more FZ positions. Clearly such an approach would decrease heating times, but by how much remains unclear, especially given the small gains when going from four to 17 FZ positions in the current study.

Third, the results show that treatments at optimal spacings reduce treatment time, with larger reductions coming from the use of optimal spacings in the axial direction than in the transverse direction. This greater reduction comes as a result of the axial overlap of the sequential focal zone’s SAR patterns, and thus the greater level of preheating of the current focal zone due to the previous focal zones’ heating versus heating focal zones in a transverse raster fashion within a single axial plane. This greater level of interaction between the heating of pulses in an axial stack means not only that the dose is deposited at an accelerated rate when points are heated along an axial stack, but that there is more of an opportunity to shape the final profile of the dose deposited in the tumour along this axial stack than there is in transverse scanning paths, where less interaction occurs.

Given the results presented here and in previous studies [23, 25], it seems quite clear that the shortest treatment times will occur when using axially stacked, collectively optimised, concentrated heating of tumours with a large number of small focal zones at optimal spacings and with high powers. An important treatment time question then is whether such an approach can be implemented in a clinically practical manner. There are several results in the current paper that indicate that such practically can be achieved. First, there appear to be only marginal time gains from using the (very difficult, if not impossible to achieve) full knowledge, collective optimisation technique when compared to sequential, single pulse optimisation. This seems to be a result of the fact that such knowledge would only be of major value when there is a significant amount of thermal interaction among a large number of pulses. However, for the optimal scan paths [25] such interactions only occur between a small number of pulses (primarily those in any given axial stack, and to a lesser extent the adjacent stacks). This makes sequential optimisation practical, and gives almost the same treatment times as collective optimisation. Second, the sequential optimisation approach will likely be easy to implement practically in MRgHIFU, with MR temperature measurements allowing one to account for prior heating and dose delivery to each site, and to develop adaptive models to continually improve predictions of the doses delivered during tumour cooling. Since MRgHIFU can measure temperatures rapidly enough (a few seconds between measurements for a high spatial resolution [77]),

real-time control of individual pulses is possible so that close to (sequentially) optimal heating times can be realised clinically, a process that will be achieved more accurately as MRI temperature imaging improves. Third, given the significantly diminishing returns obtained with high focal zone packing densities, the current study indicates that a relatively small number of focal zones (per stack) will be adequate to rapidly treat tumours, making the treatment planning and control more practical. As larger and more complicated tumours are treated with more extensive and complicated paths (compared to the initial simple generic tumours and paths studied herein) there may be more interactions among heating pulses. Such interactions could yield further opportunities to reduce treatment time through the anticipation of future heating effects by either simultaneous collective optimisation of the complete treatment, or sequential optimisation that anticipates the effects of a small number of future heating pulses, e.g. all of the pulses in a stack, but not the complete treatment.

Another factor that can have a significant impact on treatment times and ablation rates is tissue perfusion. For the current study, the low perfusion value of $0.5 \text{ kg/m}^3/\text{s}$ was used for almost all studies (with the exception of the two-position axial spacing optimisation study where it was found that a $5.0 \text{ kg/m}^3/\text{s}$ tissue perfusion value left the optimal spacing and shape of the graph unchanged). Previous studies [78–80] have shown that HIFU treatments can be sensitive to changes in the tissue perfusion network, with differences in simulated ablation volumes up to 70% being reported due to the choice of perfusion model [78]. The results in the current paper indicate that while treatment times will increase as perfusion increases, the optimal heating approach will likely remain the concentrated approach. Similarly, as perfusion increases the individual pulses, effects will have less interaction, thus bringing the results from the collective optimisation techniques closer to the sequential optimisation results. Future studies should investigate tissue-specific scenarios using organ-specific blood perfusions and tumour models in order to expand upon the more generic results presented herein which provide guidelines for future research.

Finally, the tissue absorptivity coefficient changes had complex effects on the optimal heating times of the focal zone sequence in an axial stack. While a back/middle/front treatment path could always be used to avoid the problem of passing ultrasound through regions in which the absorptivity coefficient has increased, it is unclear whether this would always be time optimal. In particular, such a path leads to longer treatment times under some variable absorptivity models, such as doubling the absorptivity

immediately after treating each position. Further *in vivo* experimental determinations of how absorptivity changes with heating parameters are needed to further quantify these effects, particularly on a more clinically realistic model than the simplified model used in this study that begins to quantify the effects of absorptivity changes.

Conclusion

This study examined the treatment of tumours using concentrated and fractionated heating approaches. The results show that a concentrated heating approach produced faster treatments for all tumours studied, both for simplified treatments on axial stacks and for treatments on larger areas with simulation data matched to phantom experiments. Additionally, this study showed that optimal focal zone spacings exist in both the transverse and axial directions, and that although treatment time decreases monotonically as the number of focal zone locations is increased, the resulting treatment time gains reach a point of diminishing returns at low focal zone packing densities. Also, this study showed that, at least for the simple generic tumours studied herein, sequential optimisation of individual heating pulses gives almost the same treatment times as the much more difficult to implement simultaneous, collective pulse optimisation technique that requires complete a priori knowledge of the entire treatment. Finally, this study shows that absorptivity changes have complex effects on treatment times and on the selection of treatment path, and that further experimental data is needed to determine the magnitudes of such changes, as well as for blood perfusion, that occur clinically in tumours.

Acknowledgements

We greatly appreciate the help of Dennis Parker, Urv Vyas, Martin Cuma, Doug Christensen, Chris Dillon, Allison Payne, and Josh de Bever, and use of the UCAIR facilities for this work. A generous allocation of extensive computer time from the Center for High Performance Computing at the University of Utah is also gratefully acknowledged.

Declaration of interest: This work was partially supported by grants from the US National Institutes of Health (R01-CA134599), Siemens Medical Solutions, the Focused Ultrasound Foundation, a University of Utah Synergy Grant and the Ben B. and Iris M. Margolis Foundation. The authors alone are responsible for the content and writing of the paper.

References

- Fennessy FM, Tempamy CM. MRI-guided focused ultrasound surgery of uterine leiomyomas. *Acad Radiol* 2005;12:1158-1166.
- Hindley J, Gedroyc WM, Regan L, Stewart E, Tempamy C, Hynnen K, et al. MRI guidance of focused ultrasound therapy of uterine fibroids: Early results. *Am J Roentgenol* 2004;183:1713-1719.
- Illing RO, Kennedy JE, Wu F, ter Haar GR, Protheroe AS, Friend PJ, et al. The safety and feasibility of extracorporeal high-intensity focused ultrasound (HIFU) for the treatment of liver and kidney tumours in a Western population. *Br J Cancer* 2005;93:890-895.
- Hynnen K, Pomeroy O, Smith DN, Huber PE, McDonnold NJ, Kewenbach J, et al. MR imaging-guided focused ultrasound surgery of fibroadenomas in the breast: A feasibility study. *Radiology* 2001;219:176-185.
- Hesley GK, Felmler JP, Gebhart JS, Dunagan KT, Gony JR, Kesler JB, et al. Noninvasive treatment of uterine fibroids: Early Mayo Clinic experience with magnetic resonance imaging-guided focused ultrasound. *Mayo Clin Proc* 2006;81:936-942.
- Daum DR, Smith NB, King R, Hynnen K. In vivo demonstration of noninvasive thermal surgery of the liver and kidney using an ultrasonic phased array - Comparison of strategies using phased array systems. *Ultrasound Med Biol* 1998;25:1087-1098.
- Poissonnier L, Chapelon J-Y, Rouvière O, Curiel L, Bouvier R, Marín X, et al. Control of prostate cancer by transrectal HIFU in 227 patients. *Eur Urol* 2007;51:381-387.
- Biana A, Murat FJ, Walter B, Thurnoff S, Wieland WF, Chaussy C, et al. First analysis of the long-term results with transrectal HIFU in patients with localised prostate cancer. *Eur Urol* 2008;53:1194-1203.
- Kennedy JE. High-intensity focused ultrasound in the treatment of solid tumours. *Nat Rev Cancer* 2005;5:321-327.
- Wu F. Extracorporeal high intensity focused ultrasound in the treatment of patients with solid malignancy. *Minim Invasiv Ther* 2006;15:26-35.
- Fan X, Hynnen K. Ultrasound surgery using multiple sonications - Treatment time considerations. *Ultrasound Med Biol* 1996;22:471-482.
- Wu F, Wang ZB, Chen WZ, Zou JZ, Bai J, Zhu H, et al. Advanced hepatocellular carcinoma: Treatment with high-intensity focused ultrasound ablation combined with transcatheter arterial embolization. *Radiology* 2005;235:699-667.
- Malinen M, Huruinen T, Kaipio JP, Hynnen K. Scanning path optimization for ultrasound surgery. *Phys Med Biol* 2005;50:3473-3490.
- Zhang L, Zhu H, Jin C, Zhou K, Li K, Su H, et al. High-intensity focused ultrasound (HIFU): Effective and safe therapy for hepatocellular carcinoma adjacent to major hepatic veins. *Eur Radiol* 2009;19:437-445.
- Meléndez D, N'Djin WA, Farnetier H, Chesnois S, Riviere M, Chapelon J-Y. Ultrasound surgery with a toric transducer allows the treatment of large volumes over short periods of time. *Appl Phys Lett* 2007;91:193901-193903.
- Zhou Y, Kargl SG, Hwang JI. The effect of the scanning pathway in high-intensity focused ultrasound therapy on lesion production. *Ultrasound Med Biol* 2011;37:1497-1468.
- Harikumar P, Myers MR, Banerjee RK. HIFU procedures at moderate intensities - Effect of large blood vessels. *Phys Med Biol* 2007;52:3493.
- Malinen M, Huruinen T, Kaipio JP, Hynnen K. Scanning path optimization for ultrasound surgery. *Phys Med Biol* 2005;50:3473-3490.
- Liu H-L, Chen Y-Y, Yen J-Y, Lin W-L. Treatment time reduction for large thermal lesions by using a multiple 1D ultrasound phased array system. *Phys Med Biol* 2003;48:1173-1190.
- Sasaki K, Arima T, Kanabara K-I, Shimoda M, Kohue E-I, Umemura S-I. Effect of split-focus approach on producing larger coagulation in swine liver. *Ultrasound Med Biol* 2003;29:591-599.
- Charles Mougenot RS, Jean Palussière, Nicolas Grenier, Chris T.W. Moonen. Automatic spatial and temporal temperature control for MR-guided focused ultrasound using fast 3D MR thermometry and multiapical trajectory of the focal point. *Magn Reson Med* 2004;52:1005-1015.
- Seip R, Sanghvi NT, Uchida T, Umemura SI. Comparison of split-beam transducer geometries and excitation configurations for transrectal prostate HIFU treatments. *Proc IEEE Ultrason Symp* 2001;2:1343-1346.
- Payne A, Vyas U, Blankespoor A, Christensen D, Roemer R. Minimization of HIFU pulse heating and interpulse cooling times. *Int J Hyperthermia* 2010;26:198-208.
- Roemer R, Payne AH. Minimization of HIFU dose delivery time. Paper presented at the International Society of Therapeutic Ultrasound, 2007, Seoul, Korea, 12-15 June.
- Coen J, Payne A, Roemer R. HIFU treatment time reduction in superficial tumours through focal zone path selection. *Int J Hyperthermia* 2011;27:465-481.
- Huruinen T, Kaipio JP, Malinen M. Optimal control in high intensity focused ultrasound surgery. In: Alves CJF, Pardalos PM, and Vicente LN, editors. *Optimization in Medicine*. New York: Springer; 2008. pp 169-195.
- Hynnen K, Roemer R, Anhalt D, Johnson C, Xu ZX, Swindell W, et al. A scanned, focused, multiple transducer ultrasonic system for localized hyperthermia treatments. *Int J Hyperthermia* 1987;3:21-35.
- Kennedy JE, Wu F, ter Haar GR, Gleeson FV, Phillips RR, Middleton MR, et al. High-intensity focused ultrasound for the treatment of liver tumours. *Ultrasonics* 2004;42:931-935.
- Wu F, Chen WZ, Bai J, Zou JZ, Wang ZL, Zhu H, et al. Pathological changes in human malignant carcinoma treated with high-intensity focused ultrasound. *Ultrasound Med Biol* 2001;27:1099-1106.
- Billard BE, Hynnen K, Roemer RB. Effects of physical parameters on high temperature ultrasound hyperthermia. *Ultrasound Med Biol* 1990;16:409-420.
- Damiano C, Hynnen K. The effect of various physical parameters on the size and shape of necrotic tissue volume during ultrasound surgery. *J Acoust Soc Am* 1991;95:1641-1649.
- Gianfelice D, Khan A, Boulanger Y, Amara M, Bolbidia A. Feasibility of magnetic resonance imaging-guided focused ultrasound surgery as an adjunct to tamoxifen therapy in high-risk surgical patients with breast carcinoma. *J Vasc Interv Radiol* 2003;14:1275-1282.
- McDonnold N, Moss M, Killiany R, Rosene DL, King RL, Jolesz FA, et al. MRI-guided focused ultrasound surgery in the brain: Tests in a primate model. *Magn Reson Med* 2003;49:1188-1191.
- McDonnold NJ, Jolesz FA, Hynnen KH. Determination of the optimal delay between sonications during focused ultrasound surgery in rabbits by using MR imaging to monitor thermal buildup in vivo. *Radiology* 1999;211:419-426.
- Palussiere J, Salomir R, Le Bail B, Fawaz R, Quesson B, Grenier N, et al. Feasibility of MR-guided focused ultrasound with real-time temperature mapping and continuous sonication for ablation of VX2 carcinoma in rabbit thigh. *Magn Reson Med* 2003;49:89-98.

36. McDannold N, Hynynen K, Wolf D, Wolf G, Jolesz F. MRI evaluation of thermal ablation of tumours with focused ultrasound. *J Magn Reson Imaging* 1998;8:94–100.
37. McDannold N, Hynynen K, Jolesz F. MRI monitoring of the thermal ablation of tissue: Effects of long exposure times. *J Magn Reson Imaging* 2001;13:421–427.
38. Olson JR, Samulski TV, Leopold KA, Clegg ST, Dewhirst MW, Dodge RK, et al. Sensitivity of hyperthermia trial outcomes to temperature and time: Implications for thermal goals of treatment. *Int J Radiat Oncol Biol Phys* 1993;25:289–297.
39. Sapareto SA, Dewey WC. Thermal dose determination in cancer therapy. *Int J Radiat Oncol Biol Phys* 1984;10:787–800.
40. Todd N, Payne A, Parker D. 3-D MR temperature imaging with model predictive filtering reconstruction. Paper presented at the International Society for Magnetic Resonance in Medicine Annual Meeting; 17–24 April 2009, Honolulu, Hawaii.
41. Poerner JD, Wagner CD, Deane YD, Thomsen C, Ståhlberg F, Acham E. Noninvasive MRI thermometry with the proton resonance frequency (PRF) method: In vivo results in human muscle. *Magn Reson Med* 1995;33:74–81.
42. Ishihara Y, Calderon A, Watanabe H, Okamoto K, Suzuki Y, Kurada K, et al. A precise and fast temperature mapping using water proton chemical shift. *Magn Reson Med* 1995;34:814–823.
43. Damianou C, Hynynen K. Focal spacing and near-field heating during pulsed high temperature ultrasound therapy. *Ultrasound Med Biol* 1993;19:777–787.
44. Damianou C, Hynynen K. The effect of various physical parameters on the size and shape of necrosed tissue volume during ultrasound surgery. *J Acoust Soc Am* 1994;95:1641–1649.
45. Kohler MO, Mougnot C, Quesson B, Enholm J, Le Bail B, Laurent C, et al. Volumetric HIFU ablation under 3D guidance of rapid MRI thermometry. *Med Phys* 2009;36:5521–5535.
46. Wu X, Sherar M. Theoretical evaluation of moderately focused spherical transducers and multi-focus acoustic lens transducer systems for ultrasound thermal therapy. *Phys Med Biol* 2002;47:1603–1621.
47. Cheng T-Y, Ju K-C, Ho C-S, Chen Y-Y, Chang H, Lin W-L. Sph-focussed ultrasound transducer with multidirectional heating for breast tumor thermal surgery. *Med Phys* 2008;35:1387–1397.
48. Gorny KR, Hagiandrou NJ, Hesley OK, Gossout BS, McGee KP, Feltz JP. MR guided focused ultrasound: Technical acceptance measures for a clinical system. *Phys Med Biol* 2006;51:3155–3173.
49. Enholm JK, Kohler MO, Quesson B, Mougnot C, Moonen CTW, Sekka SD. Improved volumetric MR-HIFU ablation by robust binary feedback control. *IEEE Trans Biomed Eng* 2010;57:103–113.
50. Liu H-L, Lin W-L, Chen Y-Y. A fast and conformal heating scheme for producing large thermal lesions using a 2D ultrasound phased array. *Int J Hyperthermia* 2007;23:69–82.
51. Cheng KS, Romer RB. Closed-form solution for the thermal dose delivered during single pulse thermal therapies. *Int J Hyperthermia* 2005;21:215–230.
52. Fan X, Hynynen K. A study of various parameters of spherically curved phased arrays for noninvasive ultrasound surgery. *Phys Med Biol* 1996;41:591–608.
53. Cheng K, Romer R. Blood perfusion and thermal conduction effects in Gaussian beams, minimum time single-pulse thermal therapies. *Med Phys* 2005;32:311–317.
54. Patel PR, Luk A, Durrani A, Dromi S, Cuenca J, Angstadt M, et al. In vitro and in vivo evaluations of increased effective beam width for heat deposition using a split focus high intensity ultrasound (HIFU) transducer. *Int J Hyperthermia* 2008;24:537–549.
55. Zderic V, Keshavard A, Andrew MA, Vazay S, Martin RW. Attenuation of porcine tissues in vivo after high-intensity ultrasound treatment. *Ultrasound Med Biol* 2004;30:61–66.
56. Keshavard A, Vazay S, Kaczowski PJ, Keilman G, Martin R, Chi EY, et al. Attenuation coefficient and sound speed in human myometrium and uterine fibroid tumors. *J Ultrasound Med* 2001;20:473–480.
57. Worthington AE, Trachtenberg J, Sherar MD. Ultrasound properties of human prostate tissue during heating. *Ultrasound Med Biol* 2002;28:1311–1318.
58. Kolos M, Sherar M, Muir J. Temperature dependent tissue properties and ultrasonic lesion formation. *Adv Heat Mass Transfer Biotech* 1999;14:113–118.
59. Damianou CA, Sanghvi NT, Fry FJ, Maas-Moreno R. Dependence of ultrasonic attenuation and absorption in dog soft tissues on temperature and thermal dose. *J Acoust Soc Am* 1997;102:628–634.
60. Clarke RL, Bush NL, Ter Haar GR. The changes in acoustic attenuation due to in vitro heating. *Ultrasound Med Biol* 2003;29:127–135.
61. Gerner MR, Wilson BC, Sherar MD. Ultrasound properties of liver tissue during heating. *Ultrasound Med Biol* 1997;23:1395–1403.
62. Techapoo U, Varghese T, Chen Q, Stiles TA, Zagzebski JA, Frank GR. Temperature dependence of ultrasonic propagation speed and attenuation in excised canine liver tissue measured using transmitted and reflected pulses. *J Acoust Soc Am* 2004;115(6):2859–2865.
63. Worthington AE, Sherar MD. Changes in ultrasound properties of porcine kidney tissue during heating. *Ultrasound Med Biol* 2001;27:673–682.
64. Loulou T, Scott EP. Thermal dose optimization in hyperthermia treatments by using the conjugate gradient method. *Numer Heat Transfer A* 2002;42:661–683.
65. Lin WL, Liang TC, Yen JY, Liu HL, Chen YY. Optimization of power deposition and a heating strategy for external ultrasound thermal therapy. *Med Phys* 2001;28:2172–2181.
66. Cheng KS, Romer RB. Optimal power deposition patterns for ideal high temperature therapy/hyperthermia treatments. *Int J Hyperthermia* 2004;20:57–72.
67. Hong W, Aarvold J, O'Donnell M, Cain C. Thermal dose optimization for ultrasound tissue ablation. *IEEE Trans Ultrason Ferr* 1999;46:913–928.
68. Datta DR, Hynynen K. Optimization of thermal dose using switching mode patterns of a spherically shaped square element phased array. *Proc IEEE Ultrason Symp* 96;2:1309–1312.
69. Yarmolenko PS, Moon EJ, Landon C, Manzoor A, Hochman DW, Vighani BL, et al. Thresholds for thermal damage to normal tissues: An update. *Int J Hyperthermia* 2011;27:320–343.
70. Dewey WC. Arrhenius relationships from the molecule and cell to the clinic. *Int J Hyperthermia* 1994;10:457–483.
71. Mathworks. Constrained nonlinear optimization algorithms, 2011. Available at: <http://www.mathworks.com/products/optimization/description3.html>; Mathworks Inc.
72. Pennes HH. Analysis of tissue and arterial blood temperatures in the resting human forearm. *J Appl Physiol* 1948;1:93–122.
73. Vyas U, Christensen D. Ultrasound beam propagation using the hybrid angular spectrum method. Paper presented at the Engineering in Medicine and Biology Society 30th Annual

820 J. Coon *et al.*

- International Conference of the IEEE; 20–25 August, 2008, Vancouver, Canada.
74. US FDA. Information for Manufacturers Seeking Marketing Clearance of Diagnostic Ultrasound Systems and Transducers, 2009. Available at: <http://www.fda.gov/MedicalDevices/DeviceRegulationandGuidance/GuidanceDocuments/ucm089001.htm>.
 75. Payne A, Vyas U, Todd N, de Bever J, Christensen DA, Parker DL. The effect of electronically steering a phased array ultrasound transducer on near-field tissue heating. *Med Phys* 2011;38(9):4971–81.
 76. Coon J. Treatment time reduction through parameter optimization in magnetic resonance guided high intensity focused ultrasound treatments. Doctoral dissertation, University of Utah, 2012.
 77. Todd N, Payne A, Parker DL. Model predictive filtering for improved temporal resolution in MRI temperature imaging. *Magn Reson Med* 2010;63:1269–1279.
 78. Schutt DJ, Hammerich D. Effects of variation in perfusion rates and of perfusion models in computational models of radio frequency tumor ablation. *Med Phys* 2008;35:3462–3470.
 79. Prakash P, Diederich CJ. Considerations for theoretical modelling of thermal ablation with catheter-based ultrasonic sources: Implications for treatment planning, monitoring and control. *Int J Hyperthermia* 2012;28:69–86.
 80. He X, McGee S, Coad JE, Schmidlin F, Lizzo PA, Swanlund DJ, et al. Investigation of the thermal and tissue injury behaviour in microwave thermal therapy using a porcine kidney model. *Int J Hyperthermia* 2004;20:567–593.

CHAPTER 4

PHANTOM AND SIMULATION TEMPERATURE

MATCHING THROUGH LEAST SQUARES

FIT OF DOSE LINES

The experimental data were generated via experiments performed by Nick Todd. The simulations treatments in the work were performed by Joshua Coon.

Data from simulated treatments were matched to data acquired from experiments performed on an agar phantom. The agar phantom was prepared in house by the method described in Madsen et al. (1).

The phantom was heated using the 256 element phased transducer described previously (Imasonics Inc.). The phantom comparison study consisted of two arrangements of focal zone path locations. The first path had twenty-five points arranged in a Cartesian grid in a single transverse plane measuring and had a volume of 100 mm^3 with dimensions of 10 mm, 10 mm, and 1 mm in the transverse and axial directions respectively (with 2 mm transverse separation of focal zones). The second used two concentric circles (and a central point) in a single transverse plane with a volume of 78.5 mm^3 with transverse radii of 2.5 mm and 5 mm and an axial thickness of 1mm.

These two heating patterns were each heated using both a concentrated and fractionated heating approach. In the concentrated approach, each point in the pattern was heated once and only once during the treatment. In the fractionated approach, each point was repeatedly heated with a duty cycle of 0.1 seconds, and the treatment trajectory was repeated sufficiently many times until the cumulative heating time was the same as the cumulative heating time of the concentrated approach.

The settings for the phantom heating experiment are given in the Table 4.1. Temperatures during heating were monitored via a 3.0 Tesla MRI (Siemens Inc.) to acquire temperature data, both during heating and during a phantom cooling period that immediately followed. Temperatures were acquired using a 3D Segmented EPI GRE Sequence with an EPI factor of 9, TR=35ms, TE=10 ms, Flip angle = 40 degrees, and a bandwidth of 766 Hz/pixel. Voxel resolution for the acquired images was 1.5 x 1.5 x 3.0 mm, which was interpolated to isotropic 1 mm voxels via zero-filled interpolation for data analysis. The images were reconstructed via using a Temporally Constrained Reconstruction (TCR) algorithm (2).

Maps of thermal dose were then extracted from the raw data by integrating the reconstructed temperature maps over time (with a 2 second temporal resolution) to extract the final thermal dose delivered to the phantom by the end of heating and cooling. Three “control planes” were then extracted from the full data set. These control planes consisted of dose maps of three orthogonal planes (XY, YZ, XZ) through the central voxel of the phantom heating grid. The control planes all had 1 mm thickness and length/breadth that spanned the phantom.

Table 4.1: Summary of parameters used in the phantom treatments.

	<u>Setup</u>	<u>Concentrated</u> <u>Heating</u>	<u>Fractionated</u> <u>Heating</u>
<u>Cartesian Grid</u>	<ul style="list-style-type: none"> • 25 total points • 5 x 5 Grid • 2 mm between points 	<ul style="list-style-type: none"> • Raster • 15 sec/pt 	<ul style="list-style-type: none"> • Raster • 0.1 sec/pt • 150 Cycles
<u>Concentric Circles</u>	<ul style="list-style-type: none"> • 1 Central Point • $R_1 = 2.25\text{mm}$ 8 points • $R_2 = 4.5\text{ mm}$ 16 points 	<ul style="list-style-type: none"> • “In-to-Out” Pattern • 15 sec/pt 	<ul style="list-style-type: none"> • “In-to-Out” Pattern • 0.1 sec/pt • 1st: central pt + small circle (150 repeats) • 2nd: larger circle (150 repeats)
<u>Properties Shared by All Phantom</u>	90 Watts electrical power at transducer; focus 5 cm deep into phantom; 25 points; single transverse plane; 375 sec total heating; Electronic steering of transducer; No interpulse cooling		

	<u>Setup</u>	<u>Concentrated</u> <u>Heating</u>	<u>Fractionated</u> <u>Heating</u>
<u>Heatings</u>			
<u>Literature</u> <u>Phantom</u> <u>Properties (82)</u>	Conduction=0.4 W/m/K; Specific Heat = 4000 J/kg/°C; Attenuation = .050 Np/cm/MHz; c = 1500 m/s; Rho = 1000 kg/m ³ ; W=0 kg/m ³ /s (81)		

To match the phantom data with experimental data, SARs were calculated using HAS method on a 10 x 10 x 10 cm homogeneous simulated tissue region with phantom properties listed in Table 3.3, except for the thermal conductivity and transducer power, which were found through an iterative optimization method described below.

In this optimization method, a series of treatments were performed on a tissue region with a range of thermal conductivity values using a large number of transducer powers. Doses maps in the three control planes (described above) were then matched for the simulated and phantom treatments. The matching was performed by counting the number of voxels in each simulated treatment control plane with at least 240 CEM and at least 30 CEM of thermal dose. Then, the number of such voxels from each simulated treatment was compared to the number of voxels from the phantom treatment (similar to a method used in previous research (2)) using the following metric:

$$LS_{target} = \left[(XY_{sim} - XY_{phant})^2 + (XZ_{sim} - XZ_{phant})^2 + (YZ_{sim} - YZ_{phant})^2 \right]^{\frac{1}{2}} \quad (3.4)$$

where LS_{target} is the least squares fit to the number of voxels dosed to the target dose, XY_{sim} , XZ_{sim} , and YZ_{sim} are the number of voxels dosed to the target treatment dose in the XY , XZ , and YZ planes of the simulated treatment, respectively, and XY_{phant} , XZ_{phant} , and YZ_{phant} are the number of voxels dosed to the target treatment dose in the XY , XZ , and YZ of the phantom treatment, respectively.

Figure 4.1 shows a graph of the least squares difference for the number of voxels treated to 240 CEM and 30 CEM between data from a phantom experiment using the concentrated Cartesian grid scanning approach and a series of matching simulated treatments (along the control planes) using the “optimal” transducer power for each conduction value. This optimal value was found by examining several treatments at a fixed region conduction value and several transducer power levels and comparing the least squares fit between the number of voxels treated to 240 CEM for the phantom and simulated treatments for each transducer power. The optimal transducer power level was the one which minimized that difference.

Several additional treatments were performed with an identical setup to the method used to compare the 240 CEM simulated and phantom dose lines for treatments described above, but with the comparison made between the 30 CEM dose lines instead. In general, the transducer powers that minimized the least squares difference between the 30 CEM dose lines of the phantom and simulated treatments at the optimal transducer power were very close to the power values that minimized the least squares difference between the 240 CEM dose lines for the phantom and simulated treatments (shown in Figure 4.1).

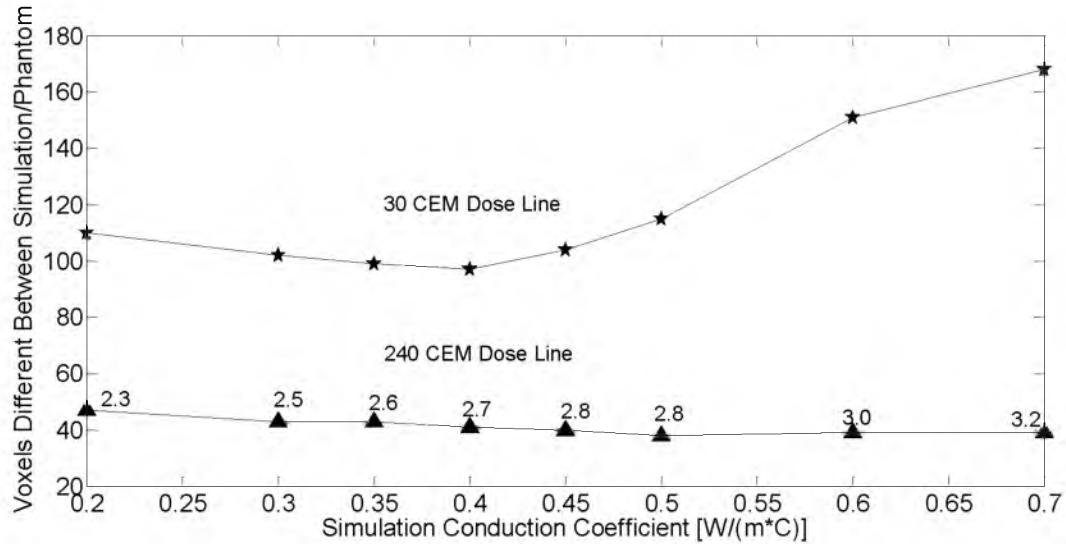


Figure 4.1: The number of voxels different between phantom data and a matching simulated treatment versus the conduction coefficient of the simulated treatment for voxels dosed to 240 CEM (triangles) and 30 CEM (stars). Shown above each point in the 240 CEM data line are the corresponding transducer power (normalized to the 0.6×10^7 W/m³ transducer power used in the axial spacing optimization studies) that minimized the difference in the number of voxels in the phantom/simulated treatment that were treated to 240 CEM. The same transducer power (as shown above the 240 CEM line) was used to generate the data points on the 30 CEM line for each conduction value.

The process of finding the optimal transducer power was then repeated for several conduction values between 0.2 and 0.7 W/(m°C) and the results are shown in Figure 4.1. It can be seen from the graph that a minimum in the plot of the 30 CEM dose line match line occurs at a conduction value of 0.4 W/(m°C). This minimum corresponds with the 0.4 W/(m°C) conduction value that is the “lookup” value predicted for the conduction of the phantom material (82).

Figure 4.2 shows the number of voxels treated to at least 240 CEM along each of the three control planes for both the phantom and simulated treatments for the concentrated and fractionated Cartesian grid and concentrated and fractionated concentric

circles treatments. The power used for the simulated treatments was fixed at the optimal power found in Figure 4.1.

For each of the scan paths that treated the 25 points (Cartesian, raster, and concentric circles), the concentrated focal zone treatments ablated a larger number of voxels to 240 than the fractionated treatments in equal amounts of treatment time, meaning that the concentrated approach had a larger ablation rate than the fractionated approach. However, no good comparison of scanning paths is possible because the areas covered by the approaches in the XY plane are different, with values of 100 mm^2 and 78.5 mm^2 , respectively. To illustrate visually how visually “close” the dose lines are for the optimal transducer and phantom conduction values suggested by analysis of Figure 4.2, dose maps of the phantom data and simulated treatment were generated for a simulated treatment with a $0.4 \text{ W}/(\text{m}^*\text{C})$ region conduction value and the optimal power found for that conduction value ($1.8 \times 10^7 \text{ W}/\text{m}^3$) and are shown in Figure 4.3-4.5. It can be seen from the graphs that, visually, the fits generated by the above optimization method are very close.

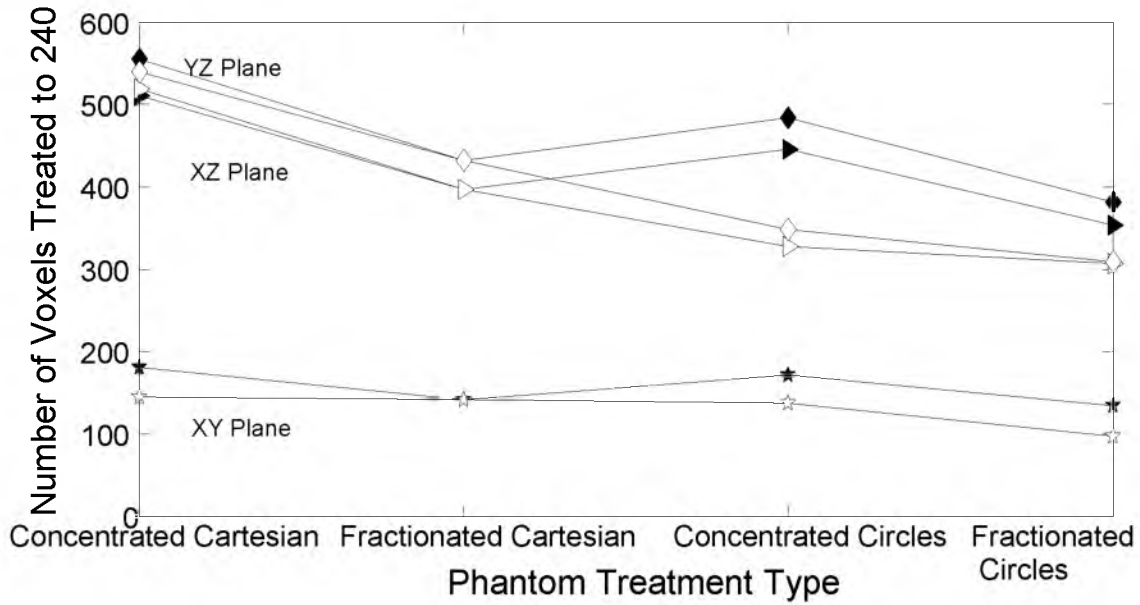


Figure 4.2: The number of voxels treated to 240 vs. the treatment type along three orthogonal planes taken through the central voxel of the treatment grid. The planes are the XY (stars), XZ (triangles), and YZ (diamonds) planes. Also shown are the numbers of voxels treated to 240 CEM for the matching simulated treatments (marked with dashed lines). The simulated treatment data points are marked with open versions of the same closed symbols used for the phantom treatment data points. The power used for all simulated treatments was the optimal power found for the concentrated Cartesian treatment using the method in Figure 4.1.

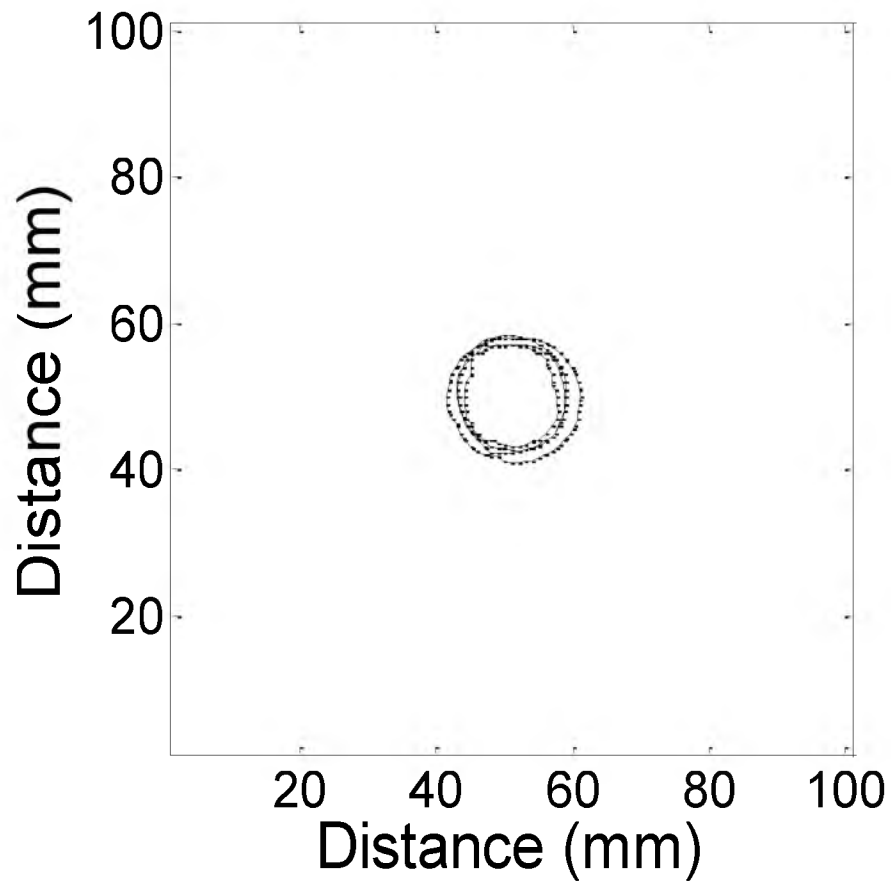


Figure 4.3: 240 and 30 CEM thermal dose contour lines for phantom heating data (solid line) and a matching simulated treatment (dashed line) for XY plane of the final dose maps, taken through the central voxel of the Cartesian grid of focal zone locations for each treatment. The dose lines for the simulated data were generated by using the optimal transducer power and conduction coefficient found in Figure 4.1.

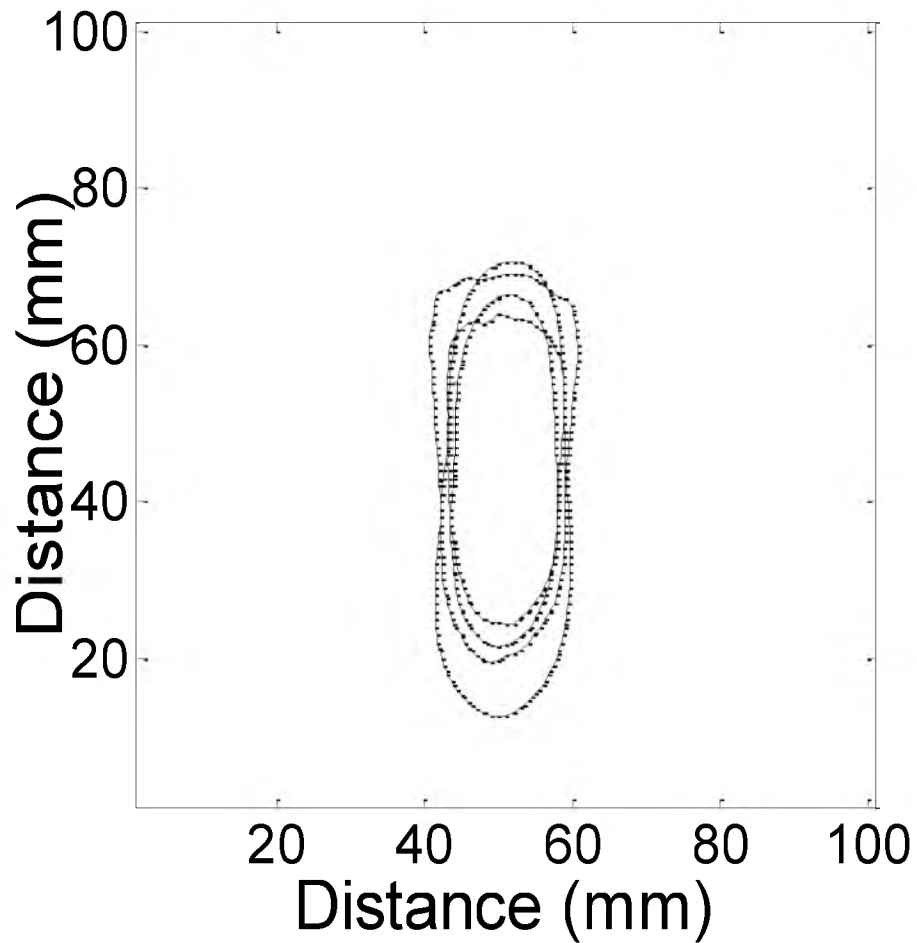


Figure 4.4: 240 and 30 CEM thermal dose contour lines for phantom heating data (solid line) and a matching simulated treatment (dashed line) for the XZ plane of the final dose maps, taken through the central voxel of the Cartesian grid of focal zone locations for each treatment. The dose lines for the simulated data were generated by using the optimal transducer power and conduction coefficient found in Figure 4.1.

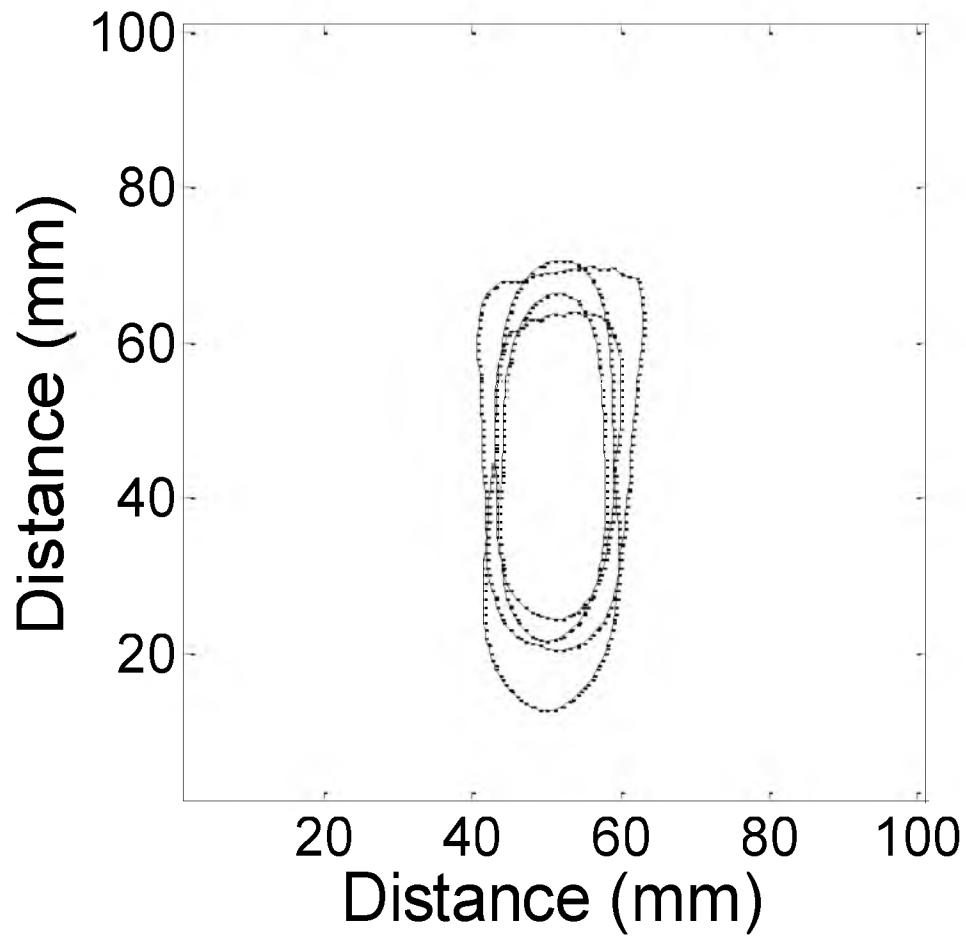


Figure 4.5: 240 and 30 CEM thermal dose contour lines for phantom heating data (solid line) and a matching simulated treatment (dashed line) for XY (top), XZ (middle) and YZ (bottom) planes of the final dose maps, taken through the central voxel of Cartesian grid of focal zone locations for each treatment. The dose lines for the simulated data were generated by using the optimal transducer power and conduction coefficient found in Figure 4.1.

References

1. Madsen EL, Frank GR, Dong F. Liquid or Solid Ultrasonically Tissue-Mimicking Materials with Very Low Scatter. *Ultrasound in Medicine & Biology*. 1998;24(4):535-42.
2. Todd N, Vyas U, de Bever J, Payne A, Parker DL. Reconstruction of fully three-dimensional high spatial and temporal resolution MR temperature maps for retrospective applications. *Magnetic Resonance in Medicine*. 2011:n/a-n/a.
3. Todd N, Vyas U, de Bever J, Payne A, Parker DL. The effects of spatial sampling choices on MR temperature measurements. *Magnetic Resonance in Medicine*. 2011;65(2):515-521.

CHAPTER 5

CONCLUSION

This work has demonstrated that large reductions in HIFU treatment times can be achieved through user-controllable parameter optimization. For the focal zone path, these simulations strongly indicate that treatments incorporating a series of adjacent axial middle-front-back axial stacks are much faster than other treatment paths tested for several perfusions, transducer powers, tumor sizes, tumor depths, and normal tissue temperature constraints. This research also gives insight into the physical mechanisms behind treatment time reduction as a function of path, which are primarily utilization of concentrated heating and thermal superposition to advantageously use nonlinear thermal dose accumulation rates. Also, this work indicates the role of adjacency between treatment stacks in situations involving a variety of normal tissue constraints. In situations where the normal tissue has a high temperature constraint, axial stacks should have greater adjacency to reduce treatment times. However, in situations where the normal tissue has a low temperature constraint, adjacency may need to be reduced to decrease thermal buildup in the normal tissue (and the need for long interpulse cooling times).

Further, this work shows that treatments with high velocity (or fractionated) focal zones have longer treatment times than treatments with concentrated focal zones for all

treatments where the two approaches were compared. These comparison treatments include: a single axial stack with a variety of focal zone spacings and packings, perfusions, power levels, concentrated focal zone treatment paths, and fractionated focal zone duty cycles; adjacent axial stacks with a variety of spacings between the stacks and power levels; and a twenty-five position treatment in a single transverse plane, both in an agar phantom and in a simulated treatment with simulation data iteratively optimized to match the phantom data. The physical mechanism behind these shorter treatment times is again the advantageous use of thermal buildup to utilize the nonlinear rate of thermal dose deposition. Also, this work shows that an optimal spacing, both axial and transverse, exists for HIFU treatments and that there are “diminishing returns” for treatment time reduction with an increase in the number of axial positions. For two axially stacked focal zones, optimal spacing occurs when the distance between focal zones is sufficient to allow a small amount of overlap in the -3 dB SAR lines, while the optimal transverse spacing between two axial stacks occurs with a small distance between the -3 dB SAR lines.

Future Work

In the short term, the most immediate expansion to the above work would be a series of *in vivo* or *in vitro* experiments to confirm the numerous simulation results. To date, the strongest experimental confirmation has come from the agar phantom experiment for a twenty-five position treatment comparing concentrated and fractionated focal zones. A good extension would be to further confirm the results of the fractionated versus concentrated focal zone results in meat and animal models. Also, the simulation

results on optimal axial path, optimal spacing, and optimal packing could be confirmed through a series of dedicated experiments, probably within the time frame of about a year. A major impediment to experimental confirmation so far has been the difficult and time consuming work necessary to develop a functioning treatment controller for the real-world implementation of these experiments, a problem which (at the time of writing) is being researched by colleagues in the research group, with a beta treatment controller being actively tested and developed. Once the treatment controller has undergone adequate initial testing, the optimization studies described above would constitute both a good extension to the work of this dissertation and a good means of further testing and perfecting the treatment controller.

In the long term, two important extensions to the work are necessary. First, this research needs to be extended into investigating the effects on treatment time in treatments where the ultrasound attenuation and tissue perfusion levels change as a function of time. With the exception of a limited set of examples, most of the treatment simulations have been run with the assumption that these properties remain constant throughout the duration of the treatment. However, a practical impediment exists to this extension because current experimental research into how these properties actually change over time is very limited and would need to be significantly extended before a parametric simulation investigation of the effects of property changes on treatment times could be undertaken. It should be noted that a complete study of these property changes, sufficient to generate a model accurate enough for extensive computational analysis, would, in my opinion, require a dedicated team working under a multiyear grant.

Second, this research should be extended to include treatment time optimization for inhomogeneous and patient specific treatment situations. A good intermediate step would be to extend these simulations to simple situations involving homogeneous phantoms with a regular pattern of inhomogeneity introduced by the insertion and suspension of a second material, with significant validation testing of simulation results. In the longer term, optimization of models acquired from anatomical scans of patient and animal data and verified in animal models would seemingly be a necessary step to the ultimate clinical implementation of these results into HIFU treatments.

APPENDIX A

GUIDE TO SIMULATION COMPUTER CODE

Introduction

This appendix will serve as a tutorial to guide users through using the HIFU treatment simulation code developed for treatment parameter optimization. The goal for this guide is to enable a user with a general knowledge of the Matlab software platform, finite difference simulation techniques, and HIFU treatments to run the code in Appendix B to simulate and optimize treatments. This code was developed in connection with research performed at the University of Utah.

To model equations (1.1 -1.3) using a computer, the equations must be implemented using a scheme to approximate their solutions in a calculable space. One such scheme is to take a finite difference approximation to these equations. In brief, the finite difference method for solving differential equations discretizes each equation over a series of temporal and spatial steps, with the small spatial regions (usually cubes) formed by discretization called voxels. In this formulation, the derivatives of the differential equation are approximated by

$$f'(x) \approx \frac{f(x+\Delta x) - f(x)}{\Delta x} \quad (4.1)$$

where $f'(x)$ is the derivative of the continuous function, $f(x + \Delta x)$ is the function evaluated at point $x + \Delta x$, $f(x)$ is the function evaluated at point x , and Δx is a small spatial increment.

Physical properties are assumed homogenous for a given voxel, and solutions to the differential equations are assumed constant over a given voxel for a given time step. Yu et al. (1) have previously shown that, as the temporal and spatial steps of the finite difference voxels approach 0, the solution to the discrete problem becomes that of the continuous problem.

In order to optimize treatment times, it is necessary to have software that quickly and robustly simulates HIFU treatments for a variety of user-controllable input parameters and region ultrasound and physical properties. For the purposes of treatment simulation, the essential components of treatment simulations are carried out by four essential routines: HASGui5, calc_A.m, constfun1.m, and dosecalc3D.m. Also, for optimization of treatment times, a fifth function is used named Treatment_Optimization.m. This function calls the Matlab optimization routine fmincon.m with parameters specified in the code. For specific details on the input parameters possible into this function, the reader is referred to the extensive documentation available on the Matlab website.

Treatment Simulations Table

The function purpose, input parameters, and output parameters for these five functions are summarized in Table A.1.

Table A.1: Summary of purpose, input variables, and output variables for Matlab scripts and functions used for treatment simulations.

	<u>Purpose</u>	<u>Input</u>	<u>Output</u>	<u>Comments</u>
<u>HASGUI5</u>	Simulate	Transducer	Q:	For details,
	propagatio	Characteristics:	Simulated	contact Dr.
ERFA_101	n of	Transducer	ultrasound power	Douglas
x101.mat;	ultrasound	Central	density in tissue	Christensen,
param_Ax	beam from	Frequency	region	Department
ial_Optimi	transducer	Physical		of
zation.m;	through the	dimensions of	The region	Bioengineeri
Modl_Lar	tissue	transducer	pressure pattern	ng,
geUniform	region	(diameter or	data is also	University of
71x71x71.		length and	available as an	Utah.
mat are		width)	output. However,	
supporting		Transducer	this data is	Note: For
files		power	encapsulated in	simulations
		Phase and	the Q data	on
		Amplitude of	through Equation	inhomogeneo
		each element	(1).	us regions,
		(phased array		tissue
		only)		properties
		Size of each		must be
		element (phased		specified for
		array only)		region type

Table A.1 Continued

	<u>Purpose</u>	<u>Input</u>	<u>Output</u>	<u>Comments</u>
		Percent transducer area active (phased array only) Tissue Properties: Speed of Sound Density Ultrasound Attenuation Distance from transducer Modeling Properties: Voxel dimensions Region size		(i.e., water, tissue, etc.)
<u>Calc A. m</u>	Create a finite	Tissue Properties:	A: Matrix containing finite	An annotated copy of the

Table A.1 Continued

	<u>Purpose</u>	<u>Input</u>	<u>Output</u>	<u>Comments</u>
	difference time domain approximat ion of the right hand side of Equation 2 with $Q \equiv 0$	Thermal conductivity Blood perfusion Tissue density Specific heat of tissue Specific heat of blood Modeling Properties: Voxel dimensions Region size	difference approximation of the right hand side of the bioheat equation with $Q \equiv 0$. XYZ: 3-D matrix containing the 1- D addresses of each voxel in the matrix A above.	code is included in this appendix.
<u>Constfun1.</u> <u>m</u>	Calculate a HIFU treatment on a tissue region, including the time evolution	Treatment Parameters: Heating and cooling times at each focal zone location Order in which focal zone	NT_max_temp: The maximum temperature of the normal tissue reached at any time during treatment	An annotated copy of the code is included in this appendix. Note: The

Table A.1 Continued

	<u>Purpose</u>	<u>Input</u>	<u>Output</u>	<u>Comments</u>
	of the bioheat equation	locations are treated A (calculated with Calc_A.m above) B (Q calculated with HASGUI5 above divided by the density and specific heat of the tissue and the transducer power) Location of normal tissue constraint planes (if needed) Transducer power level multiplication factor (i.e. a constant by	dose_tumor_min : The minimum dose applied in any voxel of the tumor during treatment	output parameters are currently hard coded and can be changed to meet the needs of the treatment simulation.

Table A.1 Continued

	<u>Purpose</u>	<u>Input</u>	<u>Output</u>	<u>Comments</u>
		<p>which the B matrix is multiplied)</p> <p>Starting position number</p> <p>Tumor location</p> <p>Length of time dose accumulation is monitored after treatment</p> <p>Initial Region</p> <p>Temperature</p> <p>Modeling Properties:</p> <p>Time step size</p>		
<u>Dosecalc3</u> <u>d.m</u>		<p>Temperatures for tissue voxels</p> <p>Time steps between</p>	<p>doseFinal: The thermal dose applied to the region</p>	<p>An annotated copy of the code is included in</p>

Table A.1 Continued

	<u>Purpose</u>	<u>Input</u>	<u>Output</u>	<u>Comments</u>
		temperature measurements		this appendix.
<u>Treatment Optimization.m</u>		Matlab Solver: Includes calculation method for Hessian matrix, function stopping tolerance, step calculation method, etc. Data Specific: Constraints Upper and lower bounds Starting Point	Xmin: Vector containing optimized heating and cooling times for given HIFU treatment The program also outputs a variety of variables that are useful for diagnostics.	An annotated copy of the code is included in this appendix.

Calculation of Q

In order to calculate Q for the model above, the use of HASGui5 is required. For this, three external files are required by the solver. These files are: a Matlab binary file containing the phases and amplitudes of the 256 transducer elements propagated from the transducer face to a plane just outside the simulation region, a file containing the acoustic parameters of each type of tissue in the simulation region, and a file containing a 3-D model of the region with each of tissue types specified by an integer value. These files are named ERFA_101x101.mat, param_Axial_Optimization.m, and Modl_LargeUniform71x71x71.mat. An annotated copy of the *.m file is included at the end of the appendix while the *.mat files are included as attachments. For specific details on and theory behind the operation of proprietary HASGui5, the readers are encouraged to contact Dr. Douglas Christensen of the Department of Bioengineering at the University of Utah.

Once the Q values have been calculated and saved, these Q values can be converted to the B values used as inputs for the constfun1.m file by dividing by the tissue density, tissue specific heat, and the transducer power. These B values should then be saved in a cell array in a format similar to the included file B_71x71x71_1mm3_Resolution.mat. In this file, each element of the cell array corresponds to a different B matrix, with $B\{1\}$ corresponding to the most proximal focal zone, $B\{2\}$ the second most proximal, and so on until $B\{17\}$ is reached, which corresponds to the most distal focal zone. The organization of these matrices is a matter of preference.

Calculating A

Next, the matrix with the finite difference approximation of the bioheat equation must be calculated. A sample code containing the typical matrix values for simulation region, an isotropic spatial resolution of 1mm, and the correct number of finite difference nodes to cover the 7cm^3 region is included in Appendix B. The output file generated by this code containing the variables A and xyz is named `A_71_71_71_1mm.mat` and is attached to the document.

Treatment Optimization

With preliminary steps of generating the A matrix and B cell array for the treatment completed, treatment optimization studies can be run. As a debugging step, it is often useful to run the `constfun1.m` code for an input vector of treatment times independently of the optimization routine and check the temperatures and thermal dose generated by each heating pulse and cooling period. Lines of debugging code have been included for this purpose in `constfun1.m`, and they can be used by uncommenting or removing the semicolon from the end of the relevant lines of code.

Treatment optimization can be performed by running the code named `Treatment_Optimization.m`. The iterative results will display to the Matlab command window (a feature that can be changed by setting the optimization options) and the final output can be saved by inserting a `save` command at the end of the script.

Because of the large size of the parameter space for possible HIFU treatments, it is often beneficial to run treatment optimizations in a high performance computing environment.

Final Comments

There are several places where the Matlab files included in this example and their implementation can be improved. First, most of the parameters that are currently hard coded into the various *.m files could be passed into the work space using a structure called as an argument by the applicable function. Also, the code could be optimized in several locations for execution speed and memory efficiency.

For large projects, a version of the code could also be written that is designed to run either on a GPU or on multiple CPUs via a parallel computing architecture, such as MPI or Open MP. These improvements might be particularly crucial if this software is ever developed as part of a clinical patient treatment planning software package.

APPENDIX B

SIMULATION COMPUTER CODE

param_Axial_Optimization.m

```
% Parameter file for HASgui4, which calculates the pressure and Q patterns using
%  ERFA approach and the Hybrid Angular Spectrum method.
%
%  This file shows the typical ultrasound parameters used in the
%  calculation of Q profiles.
%
%Note some of these values can be edited later in the HASGui5 window if
%needed.

c0=1.5e3; % speed of sound in water (in m/s).
rho0=1.0e3; % density of water (in kg/m^3).

% The following are in mm units, must be converted to m later for calculations:
Dx=1.0; Dy=1.0; Dz=1.0; % voxel sizes in mm.
```


dmm=95; % initial value of distance in mm from transducer to Modl, needed for propagation.

offsetxmm=0; offsetymm=0; % initial values of offset of Xducer axis to model axis in mm.

hmm=0; vmm=0; zmm=0; % initial values of focus shift in mm.

Pr=100; % total radiated power in W.

% ----- Media parameters below -----

% Note: c(i) = speed of sound in (m/s) in medium i, a(i) is pressure attenuation coefficient

% in (Np/cm*MHz) (NOTE UNITS!) in medium i, rho(i) is density in (kg/m³) in medium i.

c(1)=1500; a(1)=0.05; rho(1)=1.00e3; % water (except attenuation)

mediadescr='1=breast' ;

Calc_A.m

% This code solves Pennes BHTE in a 3D domain using Finite difference. In

% this version, the user inputs the tissue parameters, the region

% resolution (i.e., spacing between nodes), and the number of nodes. The

% program will output the state-space matrix "A" of the right hand side of the

% bioheat equation (with input power set to 0) and a matrix "xyz", which

% is a 3-D matrix that registers the 1-D addresses of the finite difference
% voxels.

%In this version of the code, the inputs are hard coded for transparency.
%This can be easily converted into code where the parameters are input
%through a function.

% The X, Y and Z directions are chosen so Z is along the transducer axis, and
% X&Y are parallel to the face of the transducer.

%Hard Coded Tissue Parameters

k_nt = 0.5; % Thermal conductivity of normal tissue [W/(m C)]

w_nt = 0.5; % Blood perfusion in normal tissue [kg/(m³ s)]

rho = 1000; % Tissue density [kg/m³]

ct = 4000; % Specific heat of tissue [J/(kg C)]

cb = 4000; % Specific heat of blood [J/(kg C)]

%The resolution of the domain

del_x = .001; %Distance between node centers in the X direction in meters [m]

del_y = .001; %Distance between node centers in the Y direction in meters [m]

del_z = .001; %Distance between node centers in the Z direction in meters [m]

%The number of total nodes in each direction in the finite difference matrix.

```

n_nodes_x=71;

n_nodes_y=71;

n_nodes_z=71;


% Build the conductivity and the perfusion matrices.

cond_matrix = k_nt*ones(size(xyz));    % Initialization

perf_matrix = w_nt*ones(size(xyz));    % Initialization


%A matrix containing inhomogeneous conduction and perfusion values
%can be easily constructed by replacing values in the matrices above with
%other values. For example, suppose that the user had an input matrix slice
%M that was segmented, where different tissue types corresponded to
%different numbers in the matrix. As an example, suppose:

%
%  M= [ 1 1 2
%      2 2 2
%      1 2 1]
%
% where 2 is some tissue type (i.e., fat) and 1 is a different tissue type
% (i.e., muscle). The user could then use the FIND command to select out each
% tissue type and IND2SUB command to convert the linear addresses returned
% by the FIND command to a 3-D format. In the example above:

```

```

%
% s=find(M==2);
% ss=ind2sub(s);
% cond_matrix(ss)=cond_matrix/k_nt*k_new
%
%where k_new is the table lookup value of the conduction in muscle.

%% Code engine

%In general, it is likely not necessary for the user to modify this part of
%the code.

n_total = n_nodes_x*n_nodes_y*n_nodes_z; % Total nodes in the domain.

% Form the XY planes. The total domain will be considered as a stack of XY planes
% along the Z direction.

n_rows = n_nodes_x; % Number of rows, columns and the planes in the 3D matrix.
n_cols = n_nodes_y;
n_planes = n_nodes_z;

%This code creates the 3-D addresses that are later used to register each
%of the tumor voxels.

xyz = zeros(n_rows,n_cols,n_planes);

```

```

temp = 1;          % Initialization

for z = 1:n_planes

for y = 1:n_cols

xyz(:,y,z) = temp:(temp + n_rows-1);

temp = temp + n_rows;

end

end

A = sparse(300,300);

% 'A' matrix values for nonboundary nodes.

for kk = 2:1:n_planes-1          % All the planes except the ones at the boundary (z =
0, z = z_max)

kk

forjj = 2:1:n_cols-1            % All the planes except the ones at the boundary (y = 0, y
= y_max)

jj;

for ii = 2:1:n_rows-1           % All the planes except the ones at the boundary (x = 0, x =
x_max)

ii;

id = xyz(ii,jj,kk);             % Index of the nonsurface, nonboundary node.

```

```

    id_x_neighbor1 = xyz(ii-1,jj,kk);    % Indices of the neighbors in X,Y and Z
direction.

```

```

    id_x_neighbor2 = xyz(ii+1,jj,kk);
    id_y_neighbor1 = xyz(ii,jj-1,kk);
    id_y_neighbor2 = xyz(ii,jj+1,kk);
    id_z_neighbor1 = xyz(ii,jj,kk-1);
    id_z_neighbor2 = xyz(ii,jj,kk+1);

    A(id,id) = (1/(rho*ct))*(-(2*cond_matrix(ii,jj,kk))/del_x^2 - ...
        (2*cond_matrix(ii,jj,kk))/del_y^2 ...
        -(2*cond_matrix(ii,jj,kk))/del_z^2 ...
        - perf_matrix(ii,jj,kk)*cb);    % Diagonal element.

    A(id,id_x_neighbor1) = (1/(rho*ct))*(cond_matrix(ii-1,jj,kk)/del_x^2); %
Offdiagonal contribution due to 6 neighbors.
    A(id,id_x_neighbor2) = (1/(rho*ct))*(cond_matrix(ii+1,jj,kk)/del_x^2);
    A(id,id_y_neighbor1) = (1/(rho*ct))*(cond_matrix(ii,jj-1,kk)/del_y^2);
    A(id,id_y_neighbor2) = (1/(rho*ct))*(cond_matrix(ii,jj+1,kk)/del_y^2);
    A(id,id_z_neighbor1) = (1/(rho*ct))*(cond_matrix(ii,jj,kk-1)/del_z^2);
    A(id,id_z_neighbor2) = (1/(rho*ct))*(cond_matrix(ii,jj,kk+1)/del_z^2);
end
end
end

```



```

%keyboard

% BOUNDARIES

% 'A' matrix values for the boundary BUT nonedges (those touching 2 planes) and non-
corner

% (touching 3 planes) nodes.

forkk = [1 n_planes]          % Planes z = 0 and z = z_max

kk;

forjj = 2:1:n_cols-1          % All nodes except those at edges or corners.

for ii = 2:1:n_rows-1          % All nodes except those at edges or corners.

id = xyz(ii,jj,kk);           % Index of each node in planes z = 0 and z = z_max (and
non-edge/non-corner)

    id_x_neighbor1 = xyz(ii-1,jj,kk);    % Indices of the neighbors in X,Y and Z
direction.

    id_x_neighbor2 = xyz(ii+1,jj,kk);

    id_y_neighbor1 = xyz(ii,jj-1,kk);

    id_y_neighbor2 = xyz(ii,jj+1,kk);

ifkk ~= 1                      % z = z_max

    id_z_neighbor1 = xyz(ii,jj,kk-1);

A(id,id_z_neighbor1) = (1/(rho*ct))*(cond_matrix(ii,jj,kk-1)/del_z^2);

end

ifkk ~= n_planes% z = 0

    id_z_neighbor2 = xyz(ii,jj,kk+1);

A(id,id_z_neighbor2) = (1/(rho*ct))*(cond_matrix(ii,jj,kk+1)/del_z^2);

```

end

```

A(id,id) = (1/(rho*ct))*(-(2*cond_matrix(ii,jj,kk))/del_x^2 -
(2*cond_matrix(ii,jj,kk))/del_y^2 ...
-(2*cond_matrix(ii,jj,kk))/del_z^2 - perf_matrix(ii,jj,kk)*cb);    % Diagonal
element.

```

```

A(id,id_x_neighbor1) = (1/(rho*ct))*(cond_matrix(ii-1,jj,kk)/del_x^2); %
Offdiagonal contribution due to 4 neighbors.

```

```

A(id,id_x_neighbor2) = (1/(rho*ct))*(cond_matrix(ii+1,jj,kk)/del_x^2);

```

```

A(id,id_y_neighbor1) = (1/(rho*ct))*(cond_matrix(ii,jj-1,kk)/del_y^2);

```

```

A(id,id_y_neighbor2) = (1/(rho*ct))*(cond_matrix(ii,jj+1,kk)/del_y^2);

```

end

end

end

```

forkk = 2:1:n_planes-1          % All nodes except those at edges or corners.

```

```

kk;

```

```

forjj = [1 n_cols]              % Planes y =0 and y = y_max

```

```

for ii = 2:1:n_rows-1           % All nodes except those at edges or corners.

```

```

id = xyz(ii,jj,kk);             % Index of each node in planes z = 0 and z = z_max (and
nonedge/noncorner)

```

```

id_x_neighbor1 = xyz(ii-1,jj,kk); % Indices of the neighbors in X,Y and Z
direction.

```

```

    id_x_neighbor2 = xyz(ii+1,jj,kk);

    id_z_neighbor1 = xyz(ii,jj,kk-1);

    id_z_neighbor2 = xyz(ii,jj,kk+1);

    ifjj ~= 1                % y = y_max

        id_y_neighbor1 = xyz(ii,jj-1,kk);

    A(id,id_y_neighbor1) = (1/(rho*ct))*(cond_matrix(ii,jj-1,kk)/del_y^2);

end

    ifjj ~= n_cols % y = 0

        id_y_neighbor2 = xyz(ii,jj,kk+1);

    A(id,id_y_neighbor2) = (1/(rho*ct))*(cond_matrix(ii,jj+1,kk)/del_y^2);

end

    A(id,id) = (1/(rho*ct))*(-(2*cond_matrix(ii,jj,kk))/del_x^2 -
(2*cond_matrix(ii,jj,kk))/del_y^2 ...
    -(2*cond_matrix(ii,jj,kk))/del_z^2 - perf_matrix(ii,jj,kk)*cb);    % Diagonal
element.

    A(id,id_x_neighbor1) = (1/(rho*ct))*(cond_matrix(ii-1,jj,kk)/del_x^2); %
Offdiagonal contribution due to 4 neighbors.

    A(id,id_x_neighbor2) = (1/(rho*ct))*(cond_matrix(ii+1,jj,kk)/del_x^2);

    A(id,id_z_neighbor1) = (1/(rho*ct))*(cond_matrix(ii,jj,kk-1)/del_z^2);

    A(id,id_z_neighbor2) = (1/(rho*ct))*(cond_matrix(ii,jj,kk+1)/del_z^2);

end

end

```

```

end

forkk = 2:1:n_planes-1           % All nodes except those at edges or corners.

kk;

forjj = 2:1:n_cols-1             % Planes Y =0 and Y = y_max

for ii = [1 n_rows]              % All nodes except those at edges or corners.

id = xyz(ii,jj,kk);              % Index of each node in planes z = 0 and z = z_max (and
nonedge/noncorner)

    id_y_neighbor1 = xyz(ii,jj-1,kk);    % Indices of the neighbors in X,Y and Z
direction.

    id_y_neighbor2 = xyz(ii,jj+1,kk);

    id_z_neighbor1 = xyz(ii,jj,kk-1);

    id_z_neighbor2 = xyz(ii,jj,kk+1);

if ii ~= 1                        % x = x_max

    id_x_neighbor1 = xyz(ii-1,jj,kk);

A(id,id_x_neighbor1) = (1/(rho*ct))*(cond_matrix(ii-1,jj,kk)/del_x^2);

end

if ii ~= n_rows % x = 0

    id_x_neighbor2 = xyz(ii+1,jj,kk);

A(id,id_x_neighbor2) = (1/(rho*ct))*(cond_matrix(ii+1,jj,kk)/del_x^2);

end

```

```

    A(id,id) = (1/(rho*ct))*(-(2*cond_matrix(ii,jj,kk))/del_x^2 -
(2*cond_matrix(ii,jj,kk))/del_y^2 ...
    -(2*cond_matrix(ii,jj,kk))/del_z^2 - perf_matrix(ii,jj,kk)*cb);    % Diagonal
element.

    A(id,id_y_neighbor1) = (1/(rho*ct))*(cond_matrix(ii,jj-1,kk)/del_y^2); %
Offdiagonal contribution due to 4 neighbors.
    A(id,id_y_neighbor2) = (1/(rho*ct))*(cond_matrix(ii,jj+1,kk)/del_y^2);
    A(id,id_z_neighbor1) = (1/(rho*ct))*(cond_matrix(ii,jj,kk-1)/del_z^2);
    A(id,id_z_neighbor2) = (1/(rho*ct))*(cond_matrix(ii,jj,kk+1)/del_z^2);
end
end
end

% EDGES

% 'A' matrix values for the edges(those touching 2 planes) BUT noncorner (touching 3
planes) nodes.

forkk = [1 n_planes]                % Planes z = 0 and z = z_max
kk;

forjj = [1 n_cols]                  % Planes y = 0 and y = y_max
for ii = 2:1:n_rows-1                % All nodes except those corners.
id = xyz(ii,jj,kk);                  % Index of each node on the edge z = 0 and y = 0/y_max
AND z = z_max and y = 0/y_max

```

```

        id_x_neighbor1 = xyz(ii-1,jj,kk);    % Indices of the neighbors in X,Y and Z
direction.

        id_x_neighbor2 = xyz(ii+1,jj,kk);

    ifjj ~= 1                % y = y_max

        id_y_neighbor1 = xyz(ii,jj-1,kk);

        A(id,id_y_neighbor1) = (1/(rho*ct))*(cond_matrix(ii,jj-1,kk)/del_y^2);

    end

    ifjj ~= n_cols% y = 0

        id_y_neighbor2 = xyz(ii,jj+1,kk);

        A(id,id_y_neighbor2) = (1/(rho*ct))*(cond_matrix(ii,jj+1,kk)/del_y^2);

    end


    ifkk ~= 1                % z = z_max

        id_z_neighbor1 = xyz(ii,jj,kk-1);

        A(id,id_z_neighbor1) = (1/(rho*ct))*(cond_matrix(ii,jj,kk-1)/del_z^2);

    end

    ifkk ~= n_planes% z = 0

        id_z_neighbor2 = xyz(ii,jj,kk+1);

        A(id,id_z_neighbor2) = (1/(rho*ct))*(cond_matrix(ii,jj,kk+1)/del_z^2);

    end


    A(id,id) = (1/(rho*ct))*(-(2*cond_matrix(ii,jj,kk))/del_x^2 -
(2*cond_matrix(ii,jj,kk))/del_y^2 ...

```

```

    -(2*cond_matrix(ii,jj,kk))/del_z^2 - perf_matrix(ii,jj,kk)*cb);    % Diagonal
    element.

```

```

    A(id,id_x_neighbor1) = (1/(rho*ct))*(cond_matrix(ii-1,jj,kk)/del_x^2); %

```

Offdiagonal contribution due to 4 neighbors.

```

    A(id,id_x_neighbor2) = (1/(rho*ct))*(cond_matrix(ii+1,jj,kk)/del_x^2);

```

```

end

```

```

end

```

```

end

```

```

forkk = [1 n_planes]    % Planes z = 0 and z = z_max

```

```

kk;

```

```

forjj = 2:1:n_cols-1    % All nodes except corners

```

```

for ii = [1 n_rows]    % Planes x = 0 and x = x_max

```

```

    id = xyz(ii,jj,kk);    % Index of each node on the edge z = 0 and x = 0/x_max

```

```

    AND z = z_max and x = 0/x_max

```

```

        id_y_neighbor1 = xyz(ii,jj-1,kk);    % Indices of the neighbors in X,Y and Z
        direction.

```

```

        id_y_neighbor2 = xyz(ii,jj+1,kk);

```

```

    if ii ~= 1    % x = x_max

```

```

        id_x_neighbor1 = xyz(ii-1,jj,kk);

```

```

    A(id,id_x_neighbor1) = (1/(rho*ct))*(cond_matrix(ii-1,jj,kk)/del_x^2);

```

```

end

```

```

if ii ~= n_rows % x = 0

```



```

        id_x_neighbor2 = xyz(ii+1,jj,kk);
A(id,id_x_neighbor2) = (1/(rho*ct))*(cond_matrix(ii+1,jj,kk)/del_x^2);
end

ifkk ~= 1                % z = z_max

        id_z_neighbor1 = xyz(ii,jj,kk-1);
A(id,id_z_neighbor1) = (1/(rho*ct))*(cond_matrix(ii,jj,kk-1)/del_z^2);
end

ifkk ~= n_planes% z = 0

        id_z_neighbor2 = xyz(ii,jj,kk+1);
A(id,id_z_neighbor2) = (1/(rho*ct))*(cond_matrix(ii,jj,kk+1)/del_z^2);
end

A(id,id) = (1/(rho*ct))*(-(2*cond_matrix(ii,jj,kk))/del_x^2 -
(2*cond_matrix(ii,jj,kk))/del_y^2 ...
        -(2*cond_matrix(ii,jj,kk))/del_z^2 - perf_matrix(ii,jj,kk)*cb);    % Diagonal
element.

A(id,id_y_neighbor1) = (1/(rho*ct))*(cond_matrix(ii,jj-1,kk)/del_y^2); % Off
diagonal contribution due to 4 neighbors.

A(id,id_y_neighbor2) = (1/(rho*ct))*(cond_matrix(ii,jj+1,kk)/del_y^2);
end

end

end
end

```

```

forkk = 2:1:n_planes-1          % All nodes except corners

kk;

forjj = [1 n_cols]              % Planes y = 0 and y = y_max

for ii = [1 n_rows]             % Planes x = 0 and x = x_max

id = xyz(ii,jj,kk);             % Index of each node on the edge y = 0 and x = 0/x_max
AND y = y_max and x = 0/x_max

    id_z_neighbor1 = xyz(ii,jj,kk-1);    % Indices of the neighbors in X,Y and Z
direction.

    id_z_neighbor2 = xyz(ii,jj,kk+1);

if ii ~= 1                      % x = x_max

    id_x_neighbor1 = xyz(ii-1,jj,kk);

A(id,id_x_neighbor1) = (1/(rho*ct))*(cond_matrix(ii-1,jj,kk)/del_x^2);

end

if ii ~= n_rows % x = 0

    id_x_neighbor2 = xyz(ii+1,jj,kk);

A(id,id_x_neighbor2) = (1/(rho*ct))*(cond_matrix(ii+1,jj,kk)/del_x^2);

end

ifjj ~= 1                      % y = y_max

    id_y_neighbor1 = xyz(ii,jj-1,kk);

A(id,id_y_neighbor1) = (1/(rho*ct))*(cond_matrix(ii,jj-1,kk)/del_y^2);

end

```

```
ifjj ~= n_cols% y = 0
```

```
    id_y_neighbor2 = xyz(ii,jj+1,kk);
```

```
    A(id,id_y_neighbor2) = (1/(rho*ct))*(cond_matrix(ii,jj+1,kk)/del_y^2);
```

```
end
```

```
    A(id,id) = (1/(rho*ct))*(-(2*cond_matrix(ii,jj,kk))/del_x^2 -
```

```
    (2*cond_matrix(ii,jj,kk))/del_y^2 ...
```

```
    -(2*cond_matrix(ii,jj,kk))/del_z^2 - perf_matrix(ii,jj,kk)*cb);    % Diagonal
```

```
    element.
```

```
    A(id,id_z_neighbor1) = (1/(rho*ct))*(cond_matrix(ii,jj,kk-1)/del_z^2); %
```

```
    Offdiagonal contribution due to four neighbors.
```

```
    A(id,id_z_neighbor2) = (1/(rho*ct))*(cond_matrix(ii,jj,kk+1)/del_z^2);
```

```
end
```

```
end
```

```
end
```

```
% CORNERS
```

```
% 'A' matrix values for the corner (touching three planes) nodes.
```

```
for kk = [1 n_planes]    % All corners
```

```
    kk;
```

```
    for jj = [1 n_cols]
```

```
        for ii = [1 n_rows]
```

```

id = xyz(ii,jj,kk);          % Index of each node on the corners

%id_z_neighbor1 = xyz(ii,jj,kk-1);    % Indices of the neighbors in X,Y and Z
direction.

%id_z_neighbor2 = xyz(ii,jj,kk+1);

if ii ~= 1                    % x = x_max

    id_x_neighbor1 = xyz(ii-1,jj,kk);

    A(id,id_x_neighbor1) = (1/(rho*ct))*(cond_matrix(ii-1,jj,kk)/del_x^2);

end

if ii ~= n_rows% x = 0

    id_x_neighbor2 = xyz(ii+1,jj,kk);

    A(id,id_x_neighbor2) = (1/(rho*ct))*(cond_matrix(ii+1,jj,kk)/del_x^2);

end


ifjj ~= 1                    % y = y_max

    id_y_neighbor1 = xyz(ii,jj-1,kk);

    A(id,id_y_neighbor1) = (1/(rho*ct))*(cond_matrix(ii,jj-1,kk)/del_y^2);

end

ifjj ~= n_cols% y = 0

    id_y_neighbor2 = xyz(ii,jj+1,kk);

    A(id,id_y_neighbor2) = (1/(rho*ct))*(cond_matrix(ii,jj+1,kk)/del_y^2);

end


ifkk ~= 1                    % z = z_max

```

```

        id_z_neighbor1 = xyz(ii,jj,kk-1);
A(id,id_z_neighbor1) = (1/(rho*ct))*(cond_matrix(ii,jj,kk-1)/del_z^2);
end

ifkk ~= n_planes% z = 0

        id_z_neighbor2 = xyz(ii,jj,kk+1);
A(id,id_z_neighbor2) = (1/(rho*ct))*(cond_matrix(ii,jj,kk+1)/del_z^2);
end


A(id,id) = (1/(rho*ct))*(-(2*cond_matrix(ii,jj,kk))/del_x^2 -
(2*cond_matrix(ii,jj,kk))/del_y^2 ...
-(2*cond_matrix(ii,jj,kk))/del_z^2 - perf_matrix(ii,jj,kk)*cb);    % Diagonal
element.

end

end

end

%% Save Output

%A command can be inserted here to automatically save the output

```

Constfun1.m

```
%This is the constraint function used by Matlab for iterative optimization
%of treatment times with the fmincon function. This function takes an input
%vector of x, which is a vector of heating and cooling times in the format
%[h_1, c_1, h_2, c_2, ... h_n, c_n] where h_1 is the first pulse heating
%time, c_1 is the first interpulse cooling time, etc.

%The output of the function are the
%variables c and ceq. Respectively, these are the return values of the
%inequality and equality constraint equations used the thefmincon solver,
%respectively.

%c returns a 2x1 vector with information about
%two values in it: the minimum thermal dose
%in the tissue region and the maximum temperature in the normal tissue. The
%voxels containing the tumor and the normal tissue are defined later in the
%code. In order for a treatment to be a "feasible" solution, the values of c and
%ceq must either be empty or negative. In the current code, this can only happen
%if a) the entire tumor space is treated to at least 240 CEM by the end of
%the treatment and b) the temperature constraint is never violated. For the
%purposes of interacting with the fmincon function (because the fmincon function
%always needs a negative ceq value to know a treatment is feasible), the values actually
%reported are -minimum_thermal_dose_tumor +240 (where 240 is the dose
%threshold inside the tumor) and maximum_normal_tissue_temperature - 6
```

%(where 6 is the maximum allowable normal tissue temperature).

%For runtime purposes in equations where there is no need to have cooling
 %periods between pulses (i.e., a treatment using a small number of points),
 %the code can be modified as noted below and the input vector changed to be
 %a set of only pulse heating times.

%

function [c ceq] = constfun1(x)

input_vec=x;

%% User defined variables

%Note: the code could be modified to pass these variables through a
 %structure in the command line.

%These files contain the A and B matrices used in the finite difference
 %approximation to the bioheat equation: $\partial T / \partial t = A * T + B$. For
 %a simulation region with the number of nodes X_n , Y_n , and Z_n in the X,Y,
 %and Z directions, respectively, the variables in the bioheat equation would
 %be: T= a vector of length $X_n * Y_n * Z_n$ containing the temperatures of each

%voxel of the finite difference space in linearized format, t = the finite
 %difference solver time step, A is the $(X_n*Y_n*Z_n)*(X_n*Y_n*Z_n)$
 %state-space matrix containing a finite difference approximation of the
 %r.h.s. of the bioheat equation with no input power, and B a cell containing
 %[$X_nY_nZ_n$] size vectors of heat deposited in each voxel due to the
 %ultrasound. Different matrices in the B cell array correspond to different
 %placements/steerings for the ultrasound beam inside the tissue region.

%Currently, the A matrix is being calculated via the code in `calc_A.m` and
 %the B matrix is being calculated via the Hybrid Angular Spectrum (HAS)
 %method, using the HASGuiMatlab software.

```
load ('A_71_71_71_1mm.mat');
load ('B_71x71x71_1mm3_Resolution.mat');
```

%NT_1 and NT_2 are currently the "constraint planes" used by the program to
 %monitor temperature in the normal tissue.

```
NT_1 = xyz(:, :, 15);
```

```
NT_2 = xyz(:, :, 51);
```

%The "order" variable is used to select matrices from the B cell array in
 %the order in which the positions are to be treated. In this example, the

%matrices from B would be B{15}, B{9}, and B{21}.

order = [15, 9, 21];

power_level = 8.0; % The relative power of the transducer. The B matrices

%are multiplied by this power during transducer power on times.

posNum=1; %Initialization of the starting position

%These variables specify the range of voxels where the dose must reach 240

%CEM by the end of the treatment (i.e., the tumor).

d=36;

e=36;

f=25:41;

%This is the time step size that is later used for dose calculation.

%The dimensions are in seconds [sec].

step_size=1;

%This is the time at the end of treatment where dose accumulation continues

%to be monitored, even after the transducer has been turned off.

final_cool_down_time=200;

T_o{1}=zeros(length(A),1)'; %Starting temp of the model, assumed to be 0 in

```
%this example.
```

```
%% Internal variables initialization
```

```
%Initializations of several matrices used to store intermediate
```

```
%temperatures, times, initial temperatures, and doses.
```

```
tempsFinal_ODE=cell(108,1);
```

```
time_final=cell(108,1);
```

```
T_o=cell(108,1);
```

```
doseFinal=cell(108+1,1);
```

```
%The dimensions of the B matrix, later used in the RESHAPE command
```

```
aa=size(B{1},1);
```

```
bb=size(B{1},2);
```

```
cc=size(B{1},3);
```

```
%These are vectors later used to test the temperature values in the normal
```

```
%tissue.
```

```
NT_test1=zeros(length(input_vec)+1,1);
```

```
NT_test2=zeros(length(input_vec)+1,1);
```

```
tumorloc_temp=[reshape(xyz(d, e, f),size(d,2)*size(e,2)*size(f,2),1)];
```

```
tumorloc = [tumorloc_temp];
```

```
%% ODE solver and "engine" part of the code
```

```
for ii=1:length(input_vec)
```

```
ii;
```

```
%It is necessary to reshape the B heat deposition matrix into a vector
```

```
%in order to work with the ODE45 solver.
```

```
B{order(posNum)}=reshape(B{order(posNum)},aa*bb*cc,1);
```

```
pennes_heat = @(t,x) A*x + power_level*(B{order(posNum)}); %Function used for  
beam power on
```

```
pennes_cool = @(t,x) A*x; %Function used for beam power off
```

```
%This section contains a whole series of error controls to make sure
```

```
%that a) the heating times are not negative and b) if the heating times
%are less than the step size specified, that ODE45 does not return a
%huge vector of tiny heating increments.
```

```
%For treatments where only heating times are needed, change the
%following line and the corresponding line in the cooling times code to
%the following:
```

```
%
```

```
% if mod(ii,1)==0
```

```
% if mod(ii,2)==3
```

```
%
```

```
%and make sure that your new input_vec (i.e. x) vector only contains
%heating times.
```

```
if mod(ii,2)==1 %heating times
```

```
if input_vec(ii) < 0
```

```
input_vec(ii)=0;
```

```
end
```

```
if input_vec(ii) == 0
```

```
time=[0 0];
```

```
    temps=tempsFinal_ODE(77)(end,:);
```

```
tempsFinal_ODE(77)=temps(1:end,:);
```

end

if input_vec(ii) > 0

tspan = [0:step_size:input_vec(ii)-step_size, input_vec(ii)];

if input_vec(ii) < step_size

tspan = [0, input_vec(ii)];

end

[time, temps] = ode45(pennes_heat, tspan, T_o(77)); %Matlab ODE solver

tempsFinal_ODE(77) = temps(2:end,:);

end

posNum = posNum + 1;

end

if mod(ii, 2) == 0 %cooling times

if input_vec(ii) < 0

input_vec(ii) = 0;

end

if input_vec(ii) == 0

```

time=[0 0];

    temps=tempsFinal_ODE(77)(end,:);
tempsFinal_ODE(77)=temps(1:end,:);
end

if input_vec(ii) > 0
    tspan = [0:step_size:input_vec(ii)-step_size, input_vec(ii)];

    if input_vec(ii) < step_size
        tspan = [0, input_vec(ii)];
    end

    [time,temps] =ode45(pennes_cool,tspan, T_o(77));
    tempsFinal_ODE(77)=temps(2:end,:);
end
end

time_final(77)=time;
T_o(77)=temps(end,:);

%This part of the code invokes the external function DOSECALC3D
%to calculate the thermal dose deposited in the simulation

```

```

%region due to each sonication pulse and interpulse cooling

%time.

doseFinal(77) = dosecalc3D(tempsFinal_ODE(77),time_final(77));

%Much of this code is useful for debugging – for example, to
%make sure that reasonable doses are being deposited in the
%tumor with each sonication, etc.

%[rrss]= max(doseFinal(77)) % for debugging

%max(max(tempsFinal_ODE(77))); %for debugging

%reshape(doseFinal(77),aa,bb,cc); %for debugging

% save 'temp_file_1.mat' -v7.3 %for debugging

%saves memory – comment out section for debugging
if ii>1
tempsFinal_ODE(77)=[];
end

%Records max normal tissue temp after each sonication

NT_test1(ii,1)= max(max(tempsFinal_ODE(77)(:,NT_1)));

NT_test2(ii,1)= max(max(tempsFinal_ODE(77)(:,NT_2)));

temps=[];%saves memory – comment out for debugging

```

```

%saves memory – comment out section for debugging

if ii>1

tempsFinal_ODE(77)=[];

end

T_o(77)=[];%saves memory – comment out for debugging


end


%% Accounts for time at the end of the treatment where dose accumulates
%% during cooldown


tempsFinal_ODE(77)=[];%saves memory – comment out for debugging

ii+1;

iffinal_cool_down_time> 0


step_size=1;

[time,temps]=ode45(pennes_cool,[0:step_size:final_cool_down_time], T_o(77));

tempsFinal_ODE(77)=temps(2:end,:);

time_final(77)=time;

doseFinal(77) = dosecalc3D(tempsFinal_ODE(77),time_final(77));

```



```
tempsFinal_ODE(77)=[];%saves memory – comment out for debugging
```

```
temps=[];%saves memory – comment out for debugging
```

```
T_o(77)=[];%saves memory – comment out for debugging
```

```
%for debugging
```

```
% reshape(doseFinal(77),11,11,31);
```

```
% max(doseFinal(77))
```

```
% tempsFinal_ODE(77)(:,2082);
```

```
end
```

```
%% The values passed to output
```

```
%for debugging purposes – plot should have the right "shape"
```

```
%
```

```
% temp_var=max(temps_final');
```

```
% plot(temp_var)
```

```
% for jj=1:size(temps_final')
```

```
% figure(jj)
```

```
% plot(temps_final(jj,:))
```

```
% end
```

```

% for jj=1:size(temps_final)

% [p m k]=B_Loc(temps_final(jj,:));

% [p m k]

% end


%The final dose deposited over the duration of the treatment is summed and

%recorded

dose_summation_Final=zeros(size(A,1),1);


for kk=1:length(input_vec)+1

dose_summation_Final= dose_summation_Final+doseFinal{kk};

end


%reshape(dose_summation_Final,aa,bb,cc);%for debugging


dose_tumor=dose_summation_Final(tumorloc);

%dose_FZ_min= min(dose_FZ);


%Constraint Equation 1

```

```

NT_max_temp= max(max(NT_test1, NT_test2));

%[NT_max_temp min(dose_tissue)]%for debugging


%Constraint Equation 2

dose_tumor_min = min(min(dose_tumor));


%This vector is the actual "output" part of the function. It is formatted
%this way so that the values will be negative for feasible treatments because
%fmincon requires the constraint function to return a negative value.


%If the user wants to change the constraints output by the function, the
%user simply needs to add/subtract elements from this vector. For example,
%to eliminate the NT_max_temp as a constraint, simply delete it. Further, a
%dose constraint could be imposed into the code (instead of a temperature
%constraint) by using the code:

%
% ds_1=max(dose_summation_Final(NT_1));
% ds_2=max(dose_summation_Final(NT_2));
% dose_tissue_max= max(ds_1, ds_2);
% c = [ -dose_tumor_min+240 dose_tissue_max -30];


c = [ -dose_tumor_min+240 NT_max_temp -6];

ceq = [];

```

Dosecalc3d.m

```
% Thermal dose calculation of a 3-D matrix of points in a HIFU treatment.
% The function takes as an input a matrix of temperatures TEMPS in the tissue
% region of size  $n*m$  where  $n$  is the size of the time step vector minus one
% and  $m$  is the vectorized size of the three dimensional treatment space (of
% size  $x*y*z$  where  $x$  is the number of region voxels in the  $X$  direction,
%  $y$  is the number of region voxels in the  $Y$  direction, and
%  $z$  is the number of region voxels in the  $Z$  direction) and a vector of time
% steps TIME between temperature measurements of size  $n+1$ .
%. As an output, the function returns the total thermal dose deposited in
% the region DOSEFINAL of size  $m$ .
```

```
function doseFinal = dosecalc3D(temps,time)
```

```
[J,I] = size(temps);
```

```
doseFinal=zeros(I,1);
```

```
[ll, mm] =size(time);
```

```
time_vector=zeros(ll-1, 1);
```

```
dose_cumulative=0;
```

```
time_vector=diff(time);
```

```
fori=1:I % xyz position
```

```
if max(time)==0
```

```
break;
```

```
end
```

```
dose_cumulative=0;
```

```
% %for debugging
```

```
% if mod(i,100000)==0
```

```
% fprintf('%d \n',i);
```

```
%
```

```
% end
```

```
T=temps(:,i);
```

```
if max(T) >= 2 %Don't even go through the loop if the temp in the voxel doesn't exceed
```

```
2 degrees
```

```
for j=1:J-1 % time
```

```
T100=T(j);
```

```
% Calculate the dose using T100
```

```

if T100 <= 2

dose_integ = 0;           % Dose integrand (equals  $R^{(43-T)}$ )

% with  $R=4$  for  $T<6$  and

%  $R=2$  else

elseif T100 > 2 & T100 < 6

dose_integ = (4^(T100-6));

else

dose_integ = (2^(T100-6));

end

%dt=time(j)-time(j-1);

dose_cur = time_vector(j)*(dose_integ)/60;

%dose_cur = time_vector(j)*(1/60)*trapz(dose_array);

%This

%older version of the code with the Matlab TRAPZ function was

%excluded because the function is computationally inefficient,

%which led to long dose calculation times. The current version

%of the code uses a first order Euler approximation of the dose

%integral and is much more computationally efficient.

dose_cumulative = dose_cumulative +dose_cur;

end

else

```

```
%For debugging

%dose_track=0;

end


doseFinal(i)=dose_cumulative;


%Useful code for debugging purposes.

%   if dose_cumulative>100
%       fprintf('%d \n',i)
%   end


% if i==199463

%   test=T

%   pause

% end


%dose_cumulative=0;


end
```

Treatment_Optimization.m

```

function Opt_Test_Large_Mod2

% This is an auto generated M-file from Optimization Tool.


format long;

TolFun_Data=1e-6;

TolX_Data=1e-8;

DiffMaxChange_Data=1e-2;

DiffMinChange_Data=1e-8;

%This is the lower bound in the values that are feasible for the treatment
%times, set by the user. To avoid problems with constfun1, these values
%must be positive. Also, it does not matter if there are extra constraints;
%the extras are simply ignored by the solver.

lb=[1e-6 1e-6 1e-6 1e-6 1e-6 1e-6 1e-6 1e-6 1e-6];


%Similarly, these are the upper bounds on treatment time, set by the user.

%Again, extra constraints are ignored by the solver.

ub=[300 300 300 300 300 300 300];

%This is the initial point, used for the fmincon solver but not by the
%Multistart or GlobalSearch solvers

x0=[120 0 120];

TolCon_Data=1e-4;

```



```

% Start with the default options

options = optimset;

% Modify options setting

options = optimset(options,'Display', 'iter-detailed');

options = optimset(options,'TolFun', TolFun_Data);

options = optimset(options,'FunValCheck', 'on');

options = optimset(options,'Algorithm', 'interior-point');

options = optimset(options,'Diagnostics', 'on');

options = optimset(options,'DiffMaxChange', DiffMaxChange_Data);

options = optimset(options,'DiffMinChange', DiffMinChange_Data);

options = optimset(options,'TolX', TolX_Data);

options = optimset(options,'FinDiffType', 'central');

options = optimset(options,'TolCon', TolCon_Data);

options = optimset(options,'UseParallel','always');


%This is the code to use if the user only wants to run the fmincon from one
%starting location or to run it manually from multiple starting locations
%(by changing the value of x0). To run the fmincon solver automatically
%from multiple starting locations, use the "problem = ..." code.

%[x,fval,exitflag,output,lambda,grad,hessian] = ...

%fmincon(@objfun,x0,[],[],[],[],lb,ub,@constfun2,options);

```

```

%This creates two objects in the Matlab variable space to initiate the
%Multistart and GlobalSearch optimization routines. Multistart is identical
%to running fmincon several times from random feasible starting locations.

ms = MultiStart;

gs = GlobalSearch;

problem =

createOptimProblem('fmincon','x0',100*rand(1,4),'objective',@objfun,'nonlcon',@constfun18,'lb',lb,'ub',ub,'options',options);

[xmin,fmin,flag,outpt,allmins] = run(ms,problem,2);

saveResults_2posSpacing_18_71_71_71_1mm.mat

```